



HAL
open science

Scuffing initiation prediction in a lubricated piston ring cylinder liner contact

Simona Dahdah

► **To cite this version:**

Simona Dahdah. Scuffing initiation prediction in a lubricated piston ring cylinder liner contact. Mechanics [physics.med-ph]. Université de Lyon, 2022. English. NNT : 2022LYSEI011 . tel-03709326

HAL Id: tel-03709326

<https://theses.hal.science/tel-03709326>

Submitted on 29 Jun 2022

HAL is a multi-disciplinary open access archive for the deposit and dissemination of scientific research documents, whether they are published or not. The documents may come from teaching and research institutions in France or abroad, or from public or private research centers.

L'archive ouverte pluridisciplinaire **HAL**, est destinée au dépôt et à la diffusion de documents scientifiques de niveau recherche, publiés ou non, émanant des établissements d'enseignement et de recherche français ou étrangers, des laboratoires publics ou privés.



N°d'ordre NNT :2022LYSEI011

THESE de DOCTORAT DE L'UNIVERSITE DE LYON
opérée au sein de
INSA-LYON

Ecole Doctorale ED162
MEGA
(Mécanique, Energétique, Génie civil, Acoustique)

Spécialité du doctorat : Génie mécanique

Soutenue publiquement 25/02/2022, par :
Simona Dahdah
Ingénieur mécanique

**Scuffing Initiation Prediction in a
Lubricated Piston Ring Cylinder Liner
Contact**

Devant le jury composé de :

Morina, Ardian	Professeur	University of Leeds	Rapporteur
Sherrington, Ian	Professeur	University of Central Lancashire	Rapporteur
Quillien, Muriel	Maître de conférences	ISAE-SUPMECA	Examinatrice
Charles, Pierre	Docteur	Groupe PSA	Examineur
Lubrecht, Antonius	Professeur	INSA-Lyon	Directeur de thèse
Biboulet, Nans	Maître de Conférences-HDR	INSA-Lyon	Co-directeur de thèse

Département FEDORA – INSA Lyon - Ecoles Doctorales

SIGLE	ECOLE DOCTORALE	NOM ET COORDONNEES DU RESPONSABLE
CHIMIE	<u>CHIMIE DE LYON</u> https://www.edchimie-lyon.fr Sec. : Renée EL MELHEM Bât. Blaise PASCAL, 3e étage secretariat@edchimie-lyon.fr	M. Stéphane DANIELE C2P2-CPE LYON-UMR 5265 Bâtiment F308, BP 2077 43 Boulevard du 11 novembre 1918 69616 Villeurbanne directeur@edchimie-lyon.fr
E.E.A.	<u>ÉLECTRONIQUE, ÉLECTROTECHNIQUE, AUTOMATIQUE</u> https://edeea.universite-lyon.fr Sec. : Stéphanie CAUVIN Bâtiment Direction INSA Lyon Tél : 04.72.43.71.70 secretariat.edeea@insa-lyon.fr	M. Philippe DELACHARTRE INSA LYON Laboratoire CREATIS Bâtiment Blaise Pascal, 7 avenue Jean Capelle 69621 Villeurbanne CEDEX Tél : 04.72.43.88.63 philippe.delachartre@insa-lyon.fr
E2M2	<u>ÉVOLUTION, ÉCOSYSTÈME, MICROBIOLOGIE, MODÉLISATION</u> http://e2m2.universite-lyon.fr Sec. : Sylvie ROBERJOT Bât. Atrium, UCB Lyon 1 Tél : 04.72.44.83.62 secretariat.e2m2@univ-lyon1.fr	M. Philippe NORMAND Université Claude Bernard Lyon 1 UMR 5557 Lab. d'Ecologie Microbienne Bâtiment Mendel 43, boulevard du 11 Novembre 1918 69 622 Villeurbanne CEDEX philippe.normand@univ-lyon1.fr
EDISS	<u>INTERDISCIPLINAIRE SCIENCES-SANTÉ</u> http://ediss.universite-lyon.fr Sec. : Sylvie ROBERJOT Bât. Atrium, UCB Lyon 1 Tél : 04.72.44.83.62 secretariat.ediss@univ-lyon1.fr	Mme Sylvie RICARD-BLUM Institut de Chimie et Biochimie Moléculaires et Supramoléculaires (ICBMS) - UMR 5246 CNRS - Université Lyon 1 Bâtiment Raulin - 2ème étage Nord 43 Boulevard du 11 novembre 1918 69622 Villeurbanne Cedex Tél : +33(0)4 72 44 82 32 sylvie.ricard-blum@univ-lyon1.fr
INFOMATHS	<u>INFORMATIQUE ET MATHÉMATIQUES</u> http://edinfomaths.universite-lyon.fr Sec. : Renée EL MELHEM Bât. Blaise PASCAL, 3e étage Tél : 04.72.43.80.46 infomaths@univ-lyon1.fr	M. Hamamache KHEDDOUCI Université Claude Bernard Lyon 1 Bât. Nautibus 43, Boulevard du 11 novembre 1918 69 622 Villeurbanne Cedex France Tél : 04.72.44.83.69 hamamache.kheddouci@univ-lyon1.fr
Matériaux	<u>MATÉRIAUX DE LYON</u> http://ed34.universite-lyon.fr Sec. : Yann DE ORDENANA Tél : 04.72.18.62.44 yann.de-ordenana@ec-lyon.fr	M. Stéphane BENAYOUN Ecole Centrale de Lyon Laboratoire LTDS 36 avenue Guy de Collongue 69134 Ecully CEDEX Tél : 04.72.18.64.37 stephane.benayoun@ec-lyon.fr
MEGA	<u>MÉCANIQUE, ÉNERGÉTIQUE, GÉNIE CIVIL, ACOUSTIQUE</u> http://edmega.universite-lyon.fr Sec. : Stéphanie CAUVIN Tél : 04.72.43.71.70 Bâtiment Direction INSA Lyon mega@insa-lyon.fr	M. Jocelyn BONJOUR INSA Lyon Laboratoire CETHIL Bâtiment Sadi-Carnot 9, rue de la Physique 69621 Villeurbanne CEDEX jocelyn.bonjour@insa-lyon.fr
ScSo	<u>ScSo*</u> https://edsciencesociales.universite-lyon.fr Sec. : Mélina FAVETON INSA : J.Y. TOUSSAINT Tél : 04.78.69.77.79 melina.faveton@univ-lyon2.fr	M. Christian MONTES Université Lumière Lyon 2 86 Rue Pasteur 69365 Lyon CEDEX 07 christian.montes@univ-lyon2.fr

*ScSo : Histoire, Géographie, Aménagement, Urbanisme, Archéologie, Science politique, Sociologie, Anthropologie

“Take pride in how far you’ve come. Have faith in how far you can go. But don’t forget to enjoy the journey !”

Michael Josephson

Foreword

To all those people who have supported me during my PhD journey.

Firstly, I profoundly thank my supervisor Pr. Ton Lubrecht for giving me the opportunity to work with him and for his continuous guidance, support and encouragement throughout this work.

I would also thank Dr. Nans Biboulet for all the discussions we had and for sharing his ideas with me.

This thesis is mainly the result of a cooperation between LaMCoS (Contact and Structural Mechanics Laboratory) of INSA-Lyon and Groupe PSA of Stellantis. I like to thank Prof. Daniel Nelias for the welcome at LaMCoS.

Thank to Dr. Pierre Charles for his technical and financial support.

I sincerely thank the jury members: Prof. Ian Sherrington from University of Central Lancashire (UCLan) and prof. Ardian Morina from University of Leeds for reviewing my work. I would also thank Dr. Muriel Quillien from ISAE-SUPMECA for agreeing to be a member of the committee.

I would like to thank my colleagues, who not only created a pleasant work environment but also gave me lots of support in my work: Marjolaine, Thomas, Arif, Emna, Samy.

A big thank you to my friends for their continuous support: Abdel, Georges, Joey, Elvire, Tonina, Hounayda, Christelle, Jack, Christina, Sonia and Roberte to name but a few.

A special thank you to Dr. Yana for sharing our daily ups and downs and being my biggest supporter.

I have to admit, I am surrounded by wonderful people, by a family that always gives me love, trust and support. A big thanks to everyone of them.

Thanks to my sister Mabelle, she was always there for me and I know she will always be.

My parents, Mr. Simon and Mrs. Salwa, thank you for always believing in me and encouraging me to achieve whatever I want. I hope I made you proud.

Finally, I thank God for giving me strength yesterday, today and always.

Thank you all of you again!

Abstract

The piston-ring/cylinder liner (PRCL) contact has an important influence on the friction losses of internal combustion engines (ICE). Hence, the necessity to study the phenomena acting in this contact as well as its lubrication process.

In addition, the PRCL may be exposed to scuffing. Scuffing is a failure mode that can appear in a lubricated contact with sliding bodies. It is accompanied by temperature and friction increase and vibration. Its occurrence in the ICE is rare but once it initiates, the damage is catastrophic and permanent, thus the importance to predict its initiation.

Scuffing is studied through a thermal approach to create a prediction model of its appearance in the PRCL contact. The studied thermal effects are: the thermomechanical effect and the Marangoni effect. The first effect causes a surface deformation because of the temperature increase taking place in the contact. This deformation generated an additional load to the contact. The second effect causes an oil convection which creates a temporarily local starvation. Moreover, a third effect that contributes to scuffing initiation is the ring displacement along the liner. The ring redistributes the oil and helps to avoid starvation. The influence of the problem parameters on these effects is studied to obtain charts presenting the scuffing initiation limit.

KEYWORDS PRCL contact, Scuffing, Lubrication, Numerical simulation

Résumé

Le contact segment-chemise a une importante influence sur les pertes par frottement du moteur à combustion interne (MCI). D'où la nécessité d'étudier les phénomènes présents dans ce contact ainsi que son processus de lubrification.

De plus, le contact segment-chemise peut être exposé au grippage. Le grippage est un mode de défaillance qui peut apparaître dans un contact lubrifié en présence d'une vitesse. Il s'accompagne d'une élévation de température, de frottement et de vibration. Son apparition dans le MCI est rare mais une fois il apparaît l'endommagement est catastrophique et permanent, d'où l'intérêt de prédire son initiation.

Le grippage est étudié d'une approche thermique pour créer un modèle de prédiction de son initiation dans le contact segment-chemise. Les effets thermiques introduits dans le modèle sont: l'effet thermomécanique et l'effet de Marangoni. Le premier effet cause une déformation de la surface due à l'augmentation de température prenant lieu dans le contact. Cette déformation engendre une charge additionnelle dans le contact. Le second effet cause la convection et l'écartement de l'huile, ce qui crée une sous-alimentation locale en lubrifiant dans le contact. Un troisième effet qui s'ajoute aux deux précédents est le déplacement du segment sur la chemise. Ce dernier redistribue l'huile et aide à éviter la sous-alimentation locale en lubrifiant. L'influence des paramètres du problème sur ces effets est étudiée pour obtenir des graphes présentant la limite d'initiation du grippage dans le contact segment-chemise.

MOTS CLÉS: Contact segment-chemise, Grippage, Lubrification, Simulation numérique

Contents

Contents	i
List of Figures	v
List of Tables	ix
Notation	ix
Introduction	ix
1 State of the art	9
1.1 Introduction	10
1.2 Engine lubrication	10
1.2.1 Lubrication purpose	10
1.2.2 Lubrication circuit	11
1.2.3 Lubrication types	11
1.2.4 Stribeck curve	13
1.3 Piston Ring Cylinder Liner (PRCL)	14
1.3.1 PRCL description	14
1.3.2 Piston ring functions	16
1.3.3 Scuffing	16
1.4 Heat transfer	17
1.4.1 Description	17
1.4.2 Thermal-Marangoni convection	18
1.4.3 Thermo-mechanical effect	18
1.5 Conclusion	19
2 Numerical model	21
2.1 Introduction	22
2.2 Hydrodynamic theory	24
2.2.1 Piston rings/cylinder liner	24
2.2.2 Geometry and calculational domain	24
2.2.3 Hydrodynamic operating assumptions	25
2.2.4 Lubricant supply to the contact	26

2.2.5	Equations	27
2.2.6	Hydrodynamic model implementation	30
2.3	Thermal effect	31
2.3.1	Geometry and calculational domain	31
2.3.2	Thermal operating assumptions	33
2.3.3	Thermal Marangoni effect	33
2.3.4	Equations	33
2.3.5	Thermal theory calculation	37
2.4	Scuffing prediction model	38
2.5	Conclusion	40
3	Scuffing initiation caused by local starvation in the piston ring cylinder liner	43
3.1	Introduction	44
3.2	Model presentation	44
3.2.1	Lubricant distribution model	44
3.2.2	Contact load	45
3.2.3	Model input parameters	49
3.3	Lubricant distribution	50
3.3.1	Marangoni effect	50
3.3.2	Ring passage effect	55
3.3.3	Interpretation	61
3.4	Scuffing initiation limit	61
3.4.1	Contact load depends on the ring tension only	62
3.4.2	Composed contact load	63
3.4.3	Interpretation	64
3.5	Conclusion	65
4	Scuffing initiation caused by surface heating in the piston ring cylinder liner	67
4.1	Introduction	68
4.2	Model presentation	68
4.2.1	Thermo-mechanical loop	68
4.2.2	Prediction of the additional load	69
4.2.3	Thermo-mechanical effect: temperature increase	72
4.3	Scuffing initiation limit	73
4.3.1	Lubricant additive desorption	73
4.3.2	Thermo-mechanical effect outcomes	75
4.3.3	Scuffing initiation limit	78
4.4	Coupled effects	80
4.4.1	Complete model	80
4.4.2	Coupled effects: scuffing initiation limit	80
4.5	Conclusion	83

5	Conclusion and future work	85
5.1	Conclusion	86
5.2	Future work	86
	Bibliography	87
A	Thermo-mechanical analysis using COMSOL Multiphysics	99
B	Thermo-mechanical ring model	101
B.1	3D model analysis	101
B.2	2D model analysis	101
C	Thermal liner model	109
D	Ring tension and pressure distribution	113
E	Numerical model input variables	115

List of Figures

1	Four-stroke operating cycle of an ICE engine [1]	6
2	Hybrid electric configurations: (A): parallel; (B) series; (C) split-power [2]	6
1.1	Lubrication circuit of an ICE [3]	12
1.2	Tower's test rig [4]	13
1.3	Stribeck curve illustrating the three lubrication regimes: boundary regime, mixed regime and fully flooded regime [5]	14
1.4	Piston ring	15
1.5	Tears of wine [6]	19
2.1	Surface liner [7]	22
2.2	Worn area [7]	22
2.3	Wear measurement in the y-direction [7]	23
2.4	Ring cross sections	24
2.5	Contact zone model	25
2.6	Fully flooded lubrication regime	26
2.7	Starved lubrication regime	27
2.8	Oil distribution geometry	28
2.9	Ring thermal model	32
2.10	2D liner thermal model	32
2.11	Thermal Marangoni model	34
2.12	Scuffing loop model	39
2.13	Stribeck curve: coefficient of friction as a function of the film thickness over the surface roughness	40
2.14	Detailed scuffing algorithm	41
3.1	Lubricant distribution model	45
3.2	Radial pressure pattern of a piston ring	46
3.3	Power stroke phase of the engine	47
3.4	Radial pressure distribution of a piston ring	48
3.5	Dimensionless temperature distribution generated on the liner surface	51
3.6	Dimensionless lubricant surface tension distribution	52
3.7	Dimensionless lubricant viscosity distribution	53
3.8	Dimensionless film thickness variation along the circumferential direction for different temperature increase values	54

3.9	The surface moved due to the Marangoni effect as a function of the engine speed (N)	55
3.10	Lubricant geometry distribution before the ring passage along the liner . .	56
3.11	Pressure distribution in the contact after one passage of the ring along the liner	56
3.12	Cavitated zones after one passage of the ring along the liner	57
3.13	Comparison of the pressure distribution after the first and the tenth passage of the ring along the liner	58
3.14	Lubricant distributions before and after the ring passage	59
3.15	Numerical results and curve-fit surface redistributed as a function of h_0 .	59
3.16	Numerical results and curve-fit surface redistributed as a function of λ . .	60
3.17	Numerical results and curve-fit surface redistributed as a function of the number of passages	60
3.18	Scuffing initiation limit as a function of the ring tension (F_{ring}) and the surface temperature increase (ΔT)	62
3.19	Scuffing initiation limit as a function of the ring tension and the surface temperature increase for different engine speeds	63
3.20	Thrust load distribution for an engine cycle	64
3.21	The scuffing initiation limit as a function of the ring tension and the temperature increase without and with the thrust load	65
4.1	Algorithm of the thermo-mechanical loop	69
4.2	Ring surface temperature distribution	70
4.3	Ring surface deformation as a result of the surface temperature distribution shown in figure 4.2	71
4.4	Numerical and analytic results of the additional load as a function of the ring diameter	72
4.5	Numerical and analytic results of the temperature successive increase . .	73
4.6	Stribeck curve: the coefficient of friction as a function of the temperature and the ratio of the film thickness over the surface roughness when the temperature is higher than the limit temperature	74
4.7	Temperature evolution over the thermo-mechanical loop	75
4.8	Coefficient of friction evolution over the thermo-mechanical loop	76
4.9	Temperature evolution over the thermo-mechanical loop	77
4.10	Coefficient of friction evolution over the thermo-mechanical loop	77
4.11	Scuffing initiation limit as a function of the ring tension and the temperature increase for different heated zone widths	79
4.12	Scuffing initiation limit as a function of the ring tension and the temperature increase for different oil supply regimes	79
B.1	Temperature distribution of a ring (3D model analysis)	102
B.2	Ring surface deformation as a result to the temperature variation (see figure B.1) (3D model analysis)	102

B.3	Ring surface deformation when it is exposed to a load (F) at the hot-spot (3D model analysis)	103
B.4	Temperature distribution of a ring (2D model analysis)	104
B.5	Ring surface deformation as a result of the temperature variation (see figure B.4) (2D model analysis)	104
B.6	Ring surface deformation when it exposed to a load (F) at the hot-spot (2D model analysis)	105
B.7	Case 1: mesh grid of the ring surface	106
B.8	Case 2: mesh grid of the ring surface	106
B.9	Case 3: mesh grid of the ring surface	107
B.10	Case 4: mesh grid of the ring surface	108
C.1	Liner surface with a moving heat flux	109
C.2	(X, Y) plane of the liner surface with a moving heat flux	110
C.3	Dimensionless temperature distribution on the liner surface caused by a moving heat flux	110
C.4	Liner surface with mean heat flux	111
C.5	Mesh grid of the liner surface	111
D.1	Constant contact pressure distribution	113
E.1	Lubricant kinematic viscosity as a function of the temperature	116
E.2	Lubricant density as a function of the temperature	116
E.3	Phase diagram [8]	117

List of Tables

- 2.1 Hydrodynamic dimensionless parameters 30
- 2.2 Thermal dimensionless parameters 36

- 4.1 Contribution of the coupled effects to scuffing initiation 82

- B.1 Parameters at hot-spot for the 2D and 3D analyses 103
- B.2 Parameters at hot-spot for different mesh size cases 105

- E.1 Geometric parameters 115
- E.2 Operating parameters 116

Notation

α	material conductivity [$W/m/K$]
α_{th}	thermal expansion coefficient [$1/K$]
$\bar{\eta}$	dimensionless lubricant viscosity
$\bar{\gamma}$	dimensionless lubricant surface tension
\bar{T}	dimensionless temperature
\bar{t}	dimensionless time
η	lubricant viscosity [$Pa.s$]
γ	lubricant surface tension [N/m]
Λ	dimensionless wavelength
λ	film wavelength [m]
μ	coefficient of friction
ϕ	nominal ring diameter [m]
ϕ_c	Couette flux [m^2/s]
ρ	lubricant density [Kg/m^3]
σ	surface roughness [m]
σ_{th}	thermal stress [N/m^2]
$\tau_{Marangoni}$	Marangoni stress [N/m^2]
$\tau_{viscous}$	viscous stress [N/m^2]
θ	void fraction
ε_{th}	thermal expansion
C	stroke length [m]

Notation

E	young's modulus [N/m^2]
e_d	thermal domain thickness [m]
$F_{additional}$	additional load [N]
$F_{contact}$	contact load [N]
$F_{tension}$	ring tension [N]
F_{thrust}	thrust load [N]
H	dimensionless film thickness
h	film thickness [m]
h_0	minimum film thickness [m]
H_{mean}	dimensionless mean film thickness
h_{mean}	mean film thickness [m]
H_{var}	dimensionless film variation
h_{var}	film variation with respect to h_{mean} [m]
N	engine frequency [rpm]
P	dimensionless pressure
p	pressure [Pa]
$p_{additional}$	additional pressure [Pa]
$p_{tension}$	mean ring tension pressure [Pa]
p_{thrust}	thrust pressure [Pa]
Q	dimensionless heat flux
q	heat flux [W/m^2]
R_x	ring radius of curvature [m]
s	width of the starved zone [m]
s_d	thermal domain width [m]
T	temperature [K]
t	time [s]

T_0	initial temperature [K]
t_{axial}	ring axial thickness [m]
T_{limit}	limit temperature for lubricant additives desorption [°C]
$t_{passage}$	time of a passage [s]
t_{radial}	ring radial thickness [m]
u_m	mean velocity [m/s]
v	lubricant velocity [m/s]
W_1	dimensionless load per unit length
w_1	load per unit length [N/m]
X	dimensionless axial coordinate
x	axial direction coordinate
x_a	inlet meniscus position [m]
x_b	outlet position [m]
Y	dimensionless circumferential coordinate
y	circumferential direction coordinate
y_a	left limit of the domain [m]
y_b	right limit of the domain [m]
Z	dimensionless depth coordinate
z	depth direction coordinate

Introduction

An internal combustion engine (ICE) is a heat engine in which the burn of fuel is the basic process of energy release. This liberated energy is then converted to work. The engine is composed of fixed cylinders and moving pistons. The expansion of the combustion gases pushes the piston down, which in turn rotates the crankshaft. This motion drives the vehicle wheels through a system of gears and power-train.

The ICE can be a spark-ignition (SI) gasoline engine or a compression-ignition (CI) diesel engine. In most cases and for both types, the engine operates on the four-stroke cycle. Figure 1 shows the four-stroke operating cycle of an ICE which comprises:

- **the intake stroke:** it starts with the piston at the top dead center (TDC) and ends with it at the bottom dead center (BDC). In the gasoline engine, a fuel-air mixture is drawn in the combustion chamber, whilst in the diesel engine, only air is drawn,
- **the compression stroke:** the piston compresses the mixture in the gasoline engine, a spark ignites and the combustion phase starts. In the diesel engine, the air is compressed by the piston and then the fuel is sprayed into the hot compressed gases causing it to ignite. The cylinder pressure rises rapidly,
- **the power stroke or expansion stroke:** the high-temperature and high-pressure gases push the piston down and force the crankshaft to rotate,
- **the exhaust stroke:** the remaining burned gases exit the cylinder through the exhaust ports.

In recent years, the pursuit of enhancing vehicle performance while optimizing the fuel economy and meeting the pollutant emission standards forced researchers and car manufacturers to seek green technology. One promising solution for the short term is the hybrid electric vehicle (HEV). An HEV adds an electrical machine to the conventional power-train leading to the downsizing of the engine which is beneficial for energy conservation, fuel efficiency and power losses.

The different architectures of the hybrid electric vehicle are shown in figure 2 and listed below:

- **parallel hybrid:** the electric motor and the internal combustion engine are connected to a mechanical transmission. The vehicle can be powered individually by one motor or by both collaboratively. In this configuration, the electric motor is used as a generator in order to recuperate energy for recharging the battery,

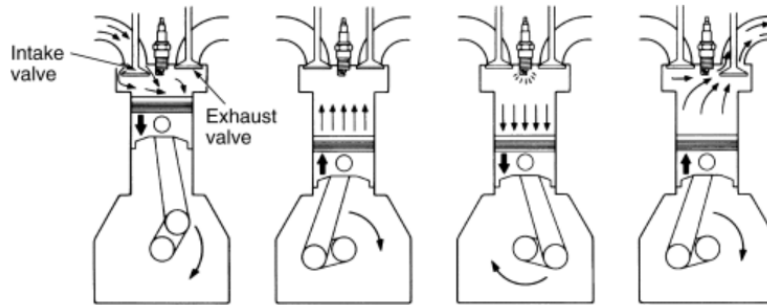


Figure 1: Four-stroke operating cycle of an ICE engine [1]

- **series hybrid:** in this configuration, the internal combustion engine drives the electric generator. The latter in turn charges the battery and powers the electric motor which is connected to the wheels, allowing the vehicle to move,
- **power-split hybrid:** the parallel and series configurations are coupled in order to combine their advantages. The vehicle can be powered by either the ICE or the electric motor working alone or by both operating simultaneously.

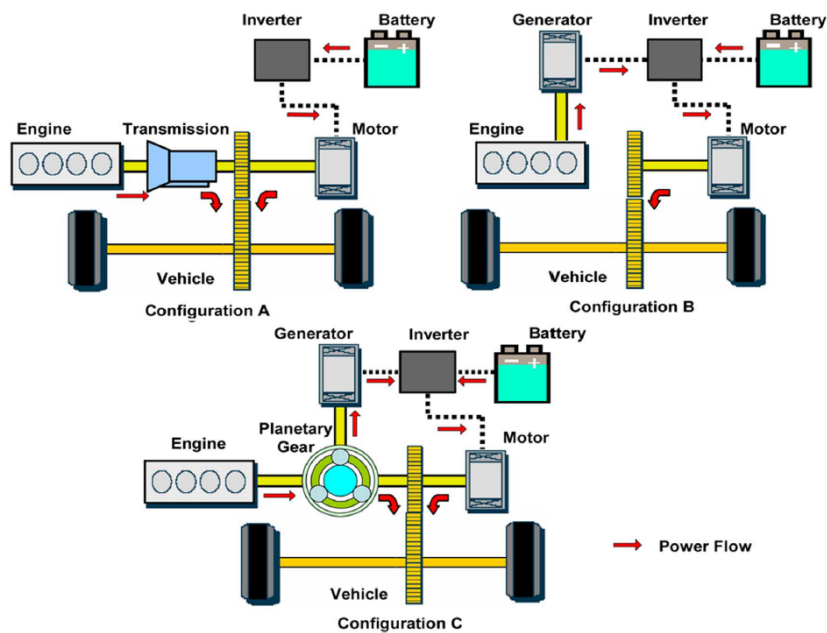


Figure 2: Hybrid electric configurations: (A): parallel; (B) series; (C) split-power [2]

For the HEV, a stop and start technology is applied for fuel saving purposes. When the vehicle is at rest, at a traffic light for example, the engine is shutting down so the energy is conserved. When the driver pushes the pedal again, the engine restarts automatically. The repetition of this feature impacts the lubrication system of the engine.

When the engine is stopped, the mechanical parts no longer receive lubricant even though the engine temperature is high. At restarting, this critical lubrication condition can lead to wear and might initiate scuffing. Scuffing is a sudden failure characterized by severe degradation of the surfaces in contact and might cause a total engine failure. Moreover, the piston-ring/cylinder-liner (PRCL) pack causes half of the engine losses [9]. So a thorough understanding of this contact and its lubrication system is needed to enhance the overall engine performance. Even though the occurrence of scuffing in the ICE is rare, experimental studies are carried on prototypes to predict and prevent its initiation. Modeling and simulation appear to be new approaches that facilitate the study of scuffing initiation. The objective of the present research is to develop a numerical model combining the parameters and phenomena causing scuffing in the PRCL contact in order to prevent its initiation.

This thesis is structured as follow:

- **Chapter 1:** this chapter gives an overall description of the lubrication circuit in an ICE, its purposes and types. It also describes the piston-ring/ cylinder-liner pack (PRCL) and its functions in the engine. Scuffing failure is also described in this chapter and the phenomena leading to its initiation,
- **Chapter 2:** this chapter introduces the numerical model coupling the parameters and phenomena influencing the scuffing initiation. It also presents the equations used for modeling,
- **Chapter 3:** this chapter analyses the phenomena impacting oil distribution and then the influence of lubricant distribution on scuffing initiation in the PRCL contact,
- **Chapter 4:** in this chapter the impact of the thermo-mechanical effect on the contact performance and its contribution to scuffing initiation are presented,
- **Chapter 5:** the main results of the current work and recommendations for future work are drawn in this chapter.

Chapter 1

State of the art

Contents

1.1	Introduction	10
1.2	Engine lubrication	10
1.2.1	Lubrication purpose	10
1.2.2	Lubrication circuit	11
1.2.3	Lubrication types	11
1.2.4	Stribeck curve	13
1.3	Piston Ring Cylinder Liner (PRCL)	14
1.3.1	PRCL description	14
1.3.2	Piston ring functions	16
1.3.3	Scuffing	16
1.4	Heat transfer	17
1.4.1	Description	17
1.4.2	Thermal-Marangoni convection	18
1.4.3	Thermo-mechanical effect	18
1.5	Conclusion	19

1.1 Introduction

The piston-ring/ cylinder-liner (PRCL) pack has an impact on the overall engine efficiency and lifetime. To optimize the PRCL pack performance and prevent its failure, one has to study the phenomena acting in this contact. A correct lubrication is the key to enhance the contact conditions and avoid its failure.

This chapter precedes the numerical study of the PRCL contact. It introduces the mechanisms occurring in the PRCL contact.

First, the importance of the lubrication process for engine reliability is presented. The lubrication purposes, method and types are also described.

The second section describes the PRCL contact and the functions of the rings. The failures that can occur in the contact such as wear and scuffing are then presented. The parameters and conditions leading to their initiation are also detailed.

Finally, the thermal effects: the Marangoni and the thermo-mechanical effects impacting the PRCL contact performance are presented.

1.2 Engine lubrication

1.2.1 Lubrication purpose

The components of the tribological systems of the engine such as gear teeth, piston rings, cylinders and cams are exposed to several failure modes that might affect engine performance and lifetime [10]. A correct lubrication is crucial to prevent engine failure and enhance its performance.

The main purposes of lubrication are [11]:

- reduces friction thus reduces engine losses,
- prevents wear,
- protects the pieces from corrosion,
- cools the heated or thermally loaded surfaces.

The lubrication process consists of injecting a fluid called lubricant between the moving parts to separate them and prevent a solid-to-solid contact [12]. A formulated lubricant is composed of base oil and additives. The additives are chemical products that enhance or add properties to the base oil. Some main additives are [13]:

- **viscosity-index improvers (VII):** prevent the oil from losing viscosity at high temperatures. They are long-chain molecules that change shape with the temperature,
- **anti-oxidants:** protect the lubricant from oxidation reactions that produce undesired species and degrade the lubricant,

- **corrosion inhibitors:** prevent corrosion by forming a barrier film on the surface,
- **extreme pressure (EP):** prevent severe surface damage like scuffing caused by direct solid-to-solid contact under high pressure by forming a coating on the metallic surface [14],
- **anti-wear (AW) agents:** reduce wear of two bodies interacting in the boundary regime where asperities contact occurs. Solid nano-particles are added to the rough surface in order to carry some of the load [15]. Due to the oil ageing process AW additive decomposition can occur [16],
- **friction modifiers:** reduce friction that can occur between the contacting surfaces. They are molecules that interact with the metal surface.

The longer the lubricant remains in service, the lower the efficiency of its additive package [17]. Moreover, when the lubricant temperature exceeds its recommended value, additive desorption can take place [18] which affects the engine performance [16].

1.2.2 Lubrication circuit

The lubrication circuit of an ICE is shown in figure 1.1. The oil is stored in a sump (oil sump/oil pan) located below the crankcase. An oil pump supplies the lubricating oil under pressure to the oil filter for filtration. Then, the oil reaches the different moving parts of the engine (crankshaft, camshaft, bearings, valves and piston pin) and is sprayed to the cylinder wall and piston rings through oil galleries. To enhance the oil distribution, a jet spray oil system can be used, especially in large, slow, two stroke, marine diesel engines [19]. Gravity pulls the oil back to the sump and the cycle is repeated.

The hot oil is cooled down by an oil cooler, which works as a radiator that transfers the heat from the lubricating oil to the coolant through its fins. It prevents the engine from overheating and retains the oil quality.

The oil supply to the PRCL pack has a significant effect on the contact performance [20] and the oil must be provided to the contact under all operating conditions of the engine. However, the oil supply to the moving parts is not controlled and the lubricant is not uniformly distributed to the piston rings and cylinder wall. For this reason, the PRCL contact might operate under mixed lubrication conditions depending on the operating conditions [21].

1.2.3 Lubrication types

1.2.3.1 Hydrodynamic Lubrication (HL)

The basics of hydrodynamic lubrication have been clarified experimentally in 1883 by Beauchamp Tower [4]. Figure 1.2 is a simplification scheme of this experiment. It is composed of a journal bearing, a bearing bush (component A) and a bearing cap (component B). From above, a load is acting on the bearing which is submerged in an oil bath.

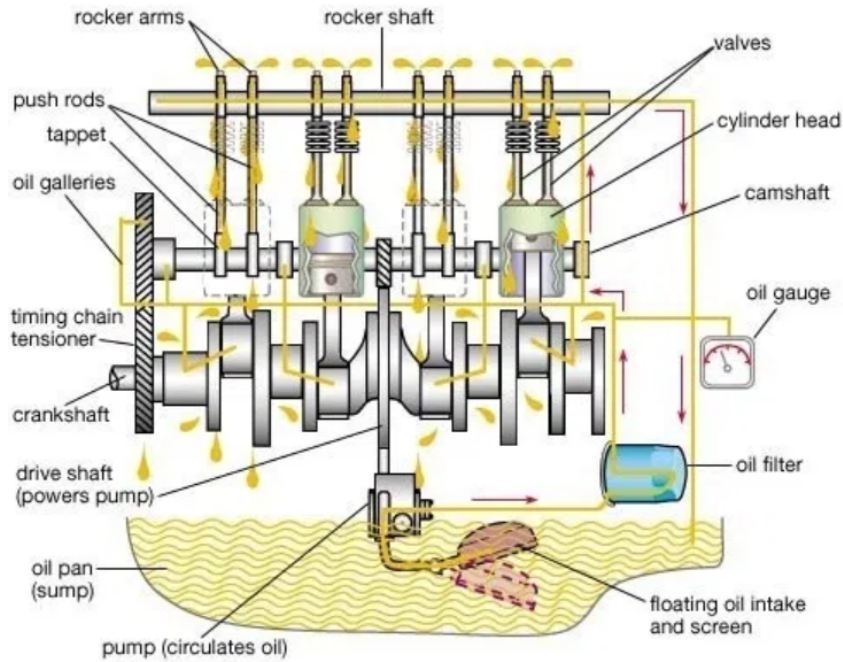


Figure 1.1: Lubrication circuit of an ICE [3]

The oil is supplied to the bearing clearance by rotating the bearing. The main discovery is that the bearing floats on an oil film subjected to a pressure which is due to the imposed load. Reynolds studied Tower's experiments theoretically and explained the generated pressure for a thin film lubricant. By combining the equations of motion and mass continuity and by taking into consideration the following assumptions, the Reynolds equation is obtained (equation 1.1) [22].

- the lubricant adheres to the surface,
- the inertia and gravitational effects can be neglected compared with the viscous effect,
- the pressure variation across the fluid film is neglected,
- the lubricant is assumed to behave as a Newtonian fluid,
- the film thickness is small compared to the radius of curvature of the ring, so the dimension along the z -direction is small compared to those in the x and y directions,
- the flow is laminar.

$$\underbrace{\frac{\partial}{\partial x} \left(\frac{\rho h^3}{12\eta} \frac{\partial p}{\partial x} \right) + \frac{\partial}{\partial y} \left(\frac{\rho h^3}{12\eta} \frac{\partial p}{\partial y} \right)}_{\text{Poiseuille}} - \underbrace{\frac{\partial (u_m \rho h)}{\partial x}}_{\text{Couette}} - \underbrace{\frac{\partial (\rho h)}{\partial t}}_{\text{transient}} = 0 \quad (1.1)$$

The first two terms of equation 1.1 represent the Poiseuille terms, they are the flow due to the pressure gradient. The third term of equation 1.1 represents the Couette term, it is the flow due to the mean velocity of the surfaces. Note that $u_m=(u_1+u_2)/2$, where u_1 and u_2 are the velocities of the two contact bodies. The last term of the equation is the transient term, it is the variation of the film thickness as a function of time.

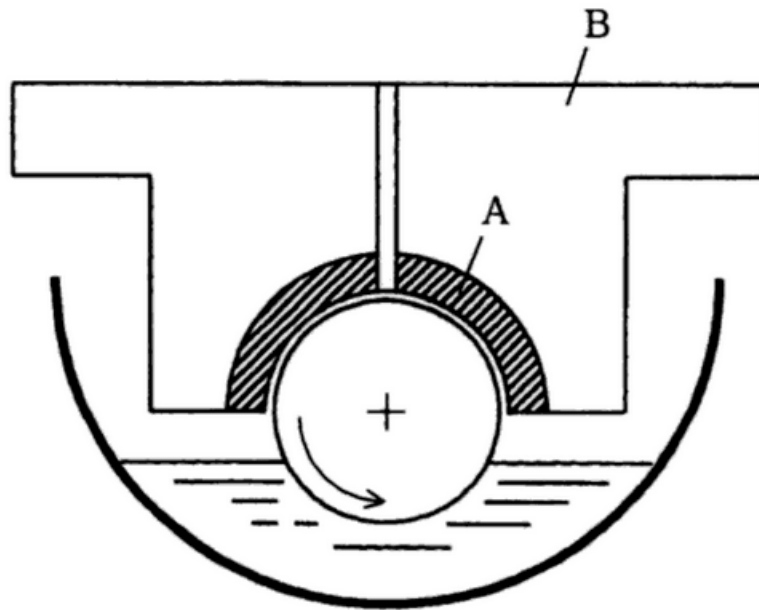


Figure 1.2: Tower's test rig [4]

1.2.3.2 Elasto-Hydrodynamic Lubrication (EHL)

The elasto-hydrodynamic lubrication is based on the phenomenon described in the previous paragraph, but in this case, the contact pressure is high enough to generate surface deformation which can change the geometry of the lubricating film [23]. Examples of machine elements that operate under EHL are rolling element bearings, gear teeth and cam [24].

1.2.4 Stribeck curve

The Stribeck diagram represents the experimental results of Richard Stribeck on journal bearings [25, 26]. The obtained results were plotted in a single curve for different lubrication regimes [27–31]. The diagram presents the coefficient of friction as a function of the dimensionless number $\eta u_m/w_1$ where η is the lubricant viscosity, u_m is the velocity and w_1 is the normal load per unit length as shown in figure 1.3. It is divided into three different regimes [32, 33]:

- **the boundary regime:** at low velocity (u_m), high load (w_1), the friction has its highest value. A high proportion of solid-to-solid contact occurs. The load is supported by the solid roughness and the role of the oil is largely lost, it does not carry load. It acts as a reservoir for additives,
- **the mixed regime:** this is the intermediate regime, it lies between the boundary and the fully flooded regimes. The load is carried by both the surface roughness and the lubricant and the friction decreases,
- **the fully flooded regime:** where a sufficiently thick film separates the surfaces and carries the entire load, this is the ideal lubrication, the friction is low. Depending on the contact pressure level, the lubrication might be hydrodynamic (HL) or elasto-hydrodynamic (EHL).

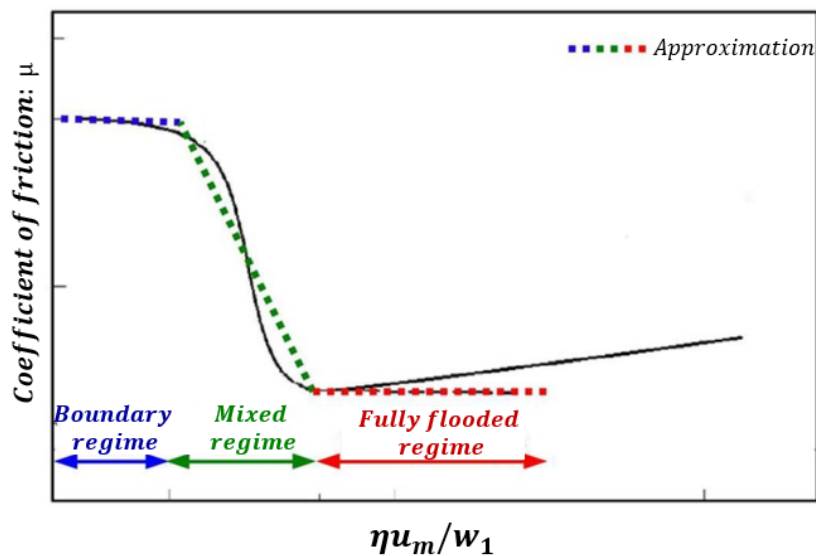


Figure 1.3: Stribeck curve illustrating the three lubrication regimes: boundary regime, mixed regime and fully flooded regime [5]

1.3 Piston Ring Cylinder Liner (PRCL)

1.3.1 PRCL description

Piston rings: The piston rings are elastic rings that fit in the piston grooves located between the piston and the cylinder wall. A piston ring is shown in figure 1.4.

The PRCL pack of the engine contains commonly three rings:

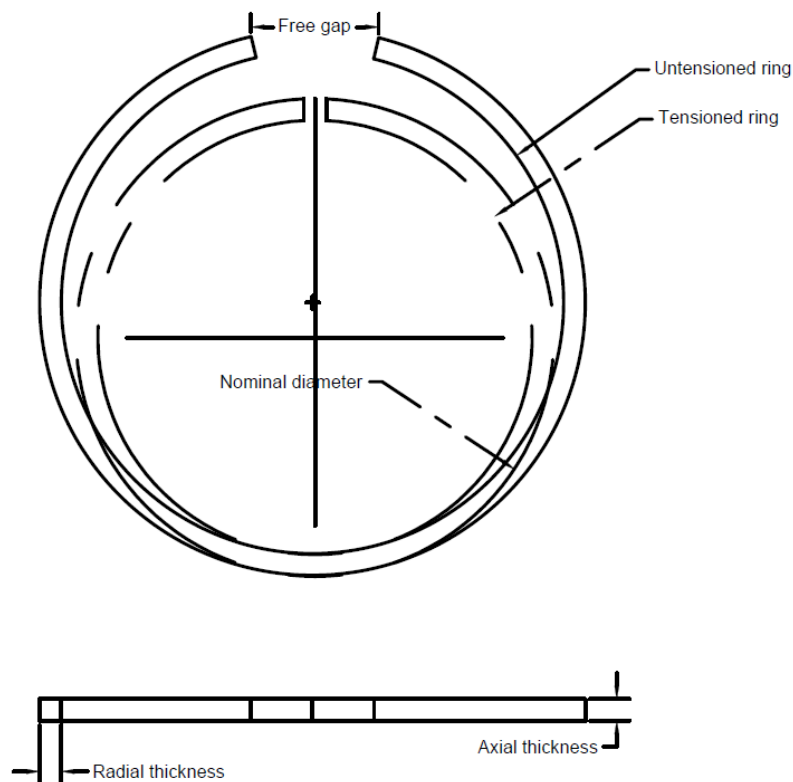


Figure 1.4: Piston ring

- **the compression ring:** it is the top ring, closest to the combustion chamber so it is exposed to the highest pressure and temperature. Its carrying surface shape is parabolic. Its main function is to seal the combustion chamber from leakage during the combustion phase. Its tension ranges between 5 and 20 N,
- **the wiper ring:** it is the second ring, located between the compression and the oil control rings. It has sealing and oil control functions. Its tension ranges between 5 and 30 N,
- **the oil control ring:** it is the closest to the crankcase, it has two running faces. Its main function is to control the oil by wiping and guiding it to the oil reservoir through its holes. Its tension ranges between 10 and 50 N.

Cylinder liner: The cylinder liner is the inner wall of an engine cylinder, where the piston and the piston rings move. It is exposed to high temperature and pressure. The liner surface material must support heat and temperature. So far, cast iron is the most common material used for the liners as it offers an optimal price-quality ratio [34].

1.3.2 Piston ring functions

The primary functions of the piston rings are:

- **the sealing function:** the rings avoid the passage of the compression gases generated during the ignition phase through the clearance between the piston and the cylinder. In that way, they prevent that the oil degrades and loses its property as a lubricant. It is a reciprocating function, they also prevent oil leakage to the combustion chamber. In that case, the oil burns causing undesirable emissions and the output engine power decreases. In addition, the sealing function prevents over-consumption of the oil,
- **the lubrication function:** since the piston is moving along the cylinder liner, a minimum amount of oil is sent to the piston and the piston rings so they move smoothly with minimum friction and wear. The oil consumption is controlled.

Their secondary functions are:

- **the heat transfer:** the heat generated during the ignition time accumulates inside the piston. The piston rings contribute to release the heat and transfer it to the cylinder,
- **the piston support:** piston rings prevent the knocking of the piston on the cylinder liner.

1.3.3 Scuffing

A common failure that occurs in the PRCL contact is wear [35]. Wear is a slowly progressing mechanism similar to corrosion and abrasion failures [36]. Ting et al. [37] developed a model to study wear occurring on the cylinder liner. The wear rate is observed to depend on the friction and the contact load. The higher the contact time, the higher the wear rate [38]. Moreover, the wear rate depends on the material coatings and the lubricant types [39,40]. A high coefficient of friction is an indicator for wear occurrence [41] and the wear rate is proportional to the contact load [42,43]. In addition, high temperature is another factor for wear appearance [44–46]. Chui et al. [47] observed that wear rate is important on the thrust and anti-thrust sides where the stresses are important.

Moreover, the PRCL contact might be exposed to scuffing. Scuffing is an uncommon failure and its initiation is rare but once it initiates the damage is catastrophic and permanent. Scuffing is the tribological failure the least understood because of the large number of variables involved in its initiation and the diversity of machine operating conditions. It occurs primarily in a lubricated contact with sliding bodies [48,49]. It is commonly accompanied by a sudden increase in friction, temperature and vibrations [50–54]. Numerous definitions are proposed to describe this failure such as : “gross damage characterized by formation of local welds between sliding surfaces” [55], “surface roughening by plastic flow whether or not there is material loss or transfer” [36] and “localized damage caused

by solid-phase welding between sliding surfaces” [56]. Dyson [55] considered that the failure of the lubricating film is the main reason for scuffing initiation. Shuster et al. [57] and Obert et al. [43] showed in their experimental study on scuffing that the oil quantity and the temperature are vital parameters. Another approach of scuffing is studied by Shen et al. [58], they concluded that the lubricant desorption leads to an increase in friction and then accelerate scuffing initiation. The rate of lubricant desorption increases also with the temperature as shown by Li et al. [59] when they study the lubricant decomposition under heat treatment. Qu et al. and Van et al. [46, 60] showed that scuffing initiates in the vicinity of the top dead center where the lubrication conditions are the worst. Johnson et al. [61] related the temperature to another approach which is the thermo-elasticity as it affects the tribological performance of the PRCL contact, see [62] and Xiaoming et al. [63]. The temperature variation taking place in the contact causes the surface deformation which in turn increases the heat flux generated and contributes to initiating failure. Barunovis et al. [64] reported wear maps and scuffing limits for a pin on disc model test as a function of the contact load and the sliding speed. From the maps, one can conclude that scuffing is reached sooner when the speed increases. Based on that, exists a probability that scuffing may occur at mid-stroke where the velocity is high. Moreover, the insufficient oil supply to the PRCL contact, might cause it to operate under mixed lubrication conditions [65–75]. Under this critical lubrication condition, solid-to-solid contact occurs increasing friction and causing failure. Another approach for scuffing prediction is based on the instability of the shear stress generated. Scuffing initiates when the shear stress exceeds the critical one, this is observed when plastic deformation occurs [76, 77]. The shear stress was identified to depend on the lubricant additives [78]. The time to scuff depends on the surface material and its wear resistance as shown by Wan et al [79]. Surface coatings such as Carbon-based, diamond-like are used for components operating in a solid-to-solid contact [80–83]. They increase the surface scuffing resistance and delay the scuffing initiation [54, 84–86].

1.4 Heat transfer

1.4.1 Description

Heat transfer is the discipline that concerns the generation, conversion and exchange of thermal energy (heat) between physical systems.

It can occur by one of the three following phenomena [87]:

- **conduction:** the heat flow is within and through the body itself and it is particularly important with metals,
- **convection:** the heat transfers from one place to another due to the movement of fluid,
- **radiation:** the heat transfers in form of waves that can travel through the air or even through empty space.

In the PRCL contact, the heat and temperature generation are caused by the presence of friction. Blok [88] initiated the study of the contact temperature caused by the heat as a result of friction (heating by friction). The study is done by considering a band-shaped heat flux moving along the solid with a constant speed. It is shown that the maximum temperature depends on the heat flux value, width and velocity and the thermal conductivity of the material.

Making fire by friction is a common example of heating by friction. By rubbing two pieces of wood for example, the temperature increases to a critical value where the oxidation of the powdered wood begins and ignition takes place with the presence of air [89]. The contact temperature is one of the key factors influencing the lubricating properties, hence the contact performance. High temperature reduces the oil viscosity, so a smaller lubricant film is formed causing the contact to operate in the boundary regime [44, 90], see figure 1.3.

1.4.2 Thermal-Marangoni convection

The Marangoni effect was identified in 1855 by James Thomson [91] in the tears of wine analysis shown in figure 1.5. When swirling a glass of wine partially filled, a thin film of wine is created on the surface of the glass. The alcohol evaporates and the leftover mixed water-wine on the side of the glass has a higher surface tension than the surface tension of the wine. As a result, the liquid flows from the lower surface tension zones to the higher ones, thus droplets are created on the side of the glass that are so-called tears of wine. The convection of fluid because of the surface tension gradient is known as the Marangoni effect [92, 93]. This effect is of primary importance in many separation processes such as distillation, absorption and extraction [94].

Velarde et al. [95] described the Marangoni effect as the physics that transforms the surface energy to a fluid flow. As a result of the fluid convection, film rupture might occur as mentioned by Fanton et al. [96] and Monti et al. [97]. When the surface tension gradient is caused by a temperature gradient, the convection effect is called thermo-capillary convection or thermal-Marangoni convection, see Gugliotti et al. [98].

1.4.3 Thermo-mechanical effect

The thermo-mechanical discipline couples two physics: the solid heat exchanges and the solid mechanics. It studies the variation of the mechanical properties of the material as a response to the heat exchange occurring in the material.

When a body is exposed to a temperature field, the mechanical properties of the surface change [99] and a thermal expansion effect takes place causing a change in its size and volume. The rate of expansion is proportional to the temperature increase, and the coefficient of proportionality is the coefficient of thermal expansion of the material (equation 2.20).

The thermo-mechanical effect appears to have an important influence on the tribological systems. In a sliding contact, the generated friction and local thermal expansion can re-

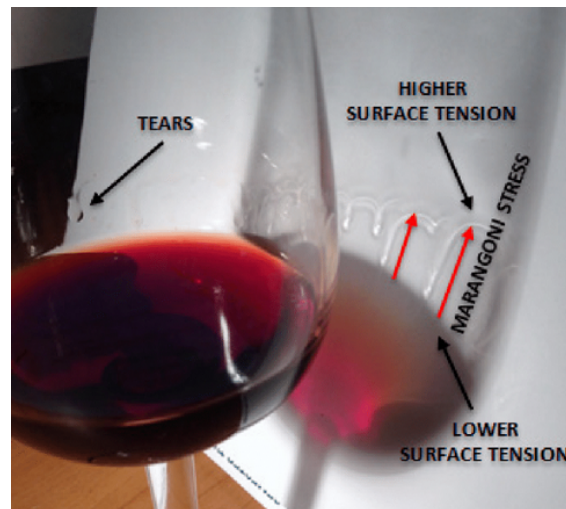


Figure 1.5: Tears of wine [6]

sult in an instability [100]. Zones with higher temperature, higher thermal expansion and then, higher stresses.

PRCL contact in ICE is exposed to a surface temperature gradient because of the friction, contact pressure and velocity of the surface. The temperature gradient affects the properties of the material [101] and causes a surface deformation. The thermal stresses created as a result of the temperature variation of the material are additional stresses to the contact. They might have a significant effect on the overall contact performance [102], hence on its service life and on the engine reliability and durability [103].

1.5 Conclusion

This chapter presented the piston-ring/ cylinder (PRCL) contact and enumerated different phenomena impacting its tribological performance.

The chapter started by presenting the lubricating mechanism and its importance in improving the engine performance by highlighting its purposes. It also described the method and types of lubrication.

The second section presented the piston-ring/cylinder-liner contact. The piston ring characteristics and roles were also described. The failure known as scuffing was presented and the parameters influencing its initiation were detailed.

The last section was dedicated to thermal effects: the Marangoni effect and the thermo-mechanical deformation which contribute to scuffing initiation.

To prevent scuffing, a thorough understanding of this failure and the physics leading to it is important. The following chapters present the numerical model coupling the parameters and phenomena influencing scuffing in order to predict its initiation as a function of the operating parameters.

Chapter 2

Numerical model

Contents

2.1	Introduction	22
2.2	Hydrodynamic theory	24
2.2.1	Piston rings/cylinder liner	24
2.2.2	Geometry and calculational domain	24
2.2.3	Hydrodynamic operating assumptions	25
2.2.4	Lubricant supply to the contact	26
2.2.5	Equations	27
2.2.6	Hydrodynamic model implementation	30
2.3	Thermal effect	31
2.3.1	Geometry and calculational domain	31
2.3.2	Thermal operating assumptions	33
2.3.3	Thermal Marangoni effect	33
2.3.4	Equations	33
2.3.5	Thermal theory calculation	37
2.4	Scuffing prediction model	38
2.5	Conclusion	40

2.1 Introduction

The basis of this study comes from the observation of the wear appearance and scuffing initiation marks on a liner surface. Figure 2.1 is a cylinder liner that has endured a severe scuffing test (full fired, load engine test that took 500 hours). The worn area is referred to as the mirror-like area. The SENSOFAR 3D profilometer is used to measure the surface profiles at five different positions along the stroke and the worn area is quantified as shown in figure 2.2. One can remark that the wear of the mirror-like area is nearly constant from the top dead center (TDC) to the bottom dead center (BDC). In fact, the piston ring velocity varies significantly from top dead center to mid stroke and likewise for the temperature gradient (note that the temperature gradient along the liner was significant since the engine test was performed full power.) Based on this analysis, one expects a variation of wear between these positions. However, there is no such variation of wear along the liner surface. Such we concluded that the ring velocity and the temperature have no primary influence on wear appearance and scuffing initiation. Moreover, wear measurement in the y -direction was carried out and given in figure 2.3. The figure shows the rapid appearance of wear and the severe transition from the unworn to the worn area. We assumed that an abrupt difference in lubricant presence was the reason for this severe transition.

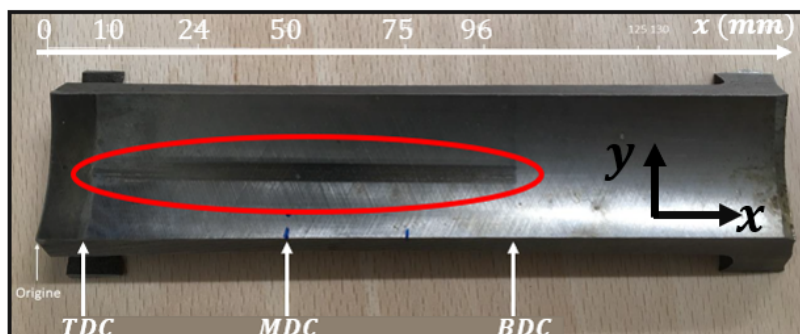


Figure 2.1: Surface liner [7]

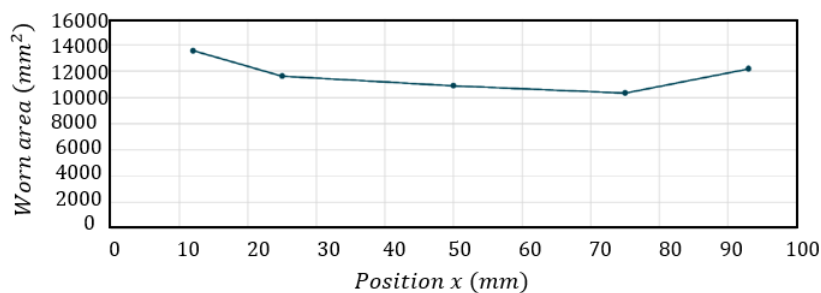


Figure 2.2: Worn area [7]

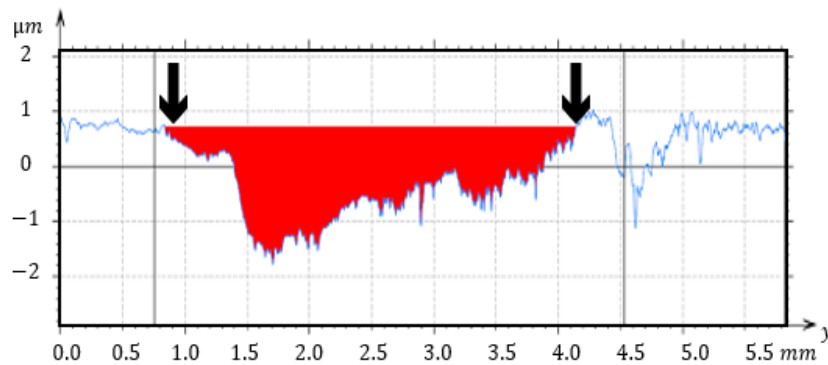


Figure 2.3: Wear measurement in the y -direction [7]

Even though scuffing occurrence in internal combustion engines of vehicle series model is rare, experimental studies are carried out on prototypes to predict and avoid its initiation. Modeling and simulation are new approaches that can facilitate the scuffing initiation study, as they provide valuable solutions by giving clear insights into real complex problems. The numerical model for scuffing occurrence prediction in the PRCL contact is detailed in this chapter. The first section describes the PRCL contact model and the hydrodynamic assumptions, equations and numerical implementation.

The hydrodynamic equations are:

- the film thickness equation,
- the oil distribution equation,
- the Reynolds equation,
- the modified Reynolds equation when considering starvation.

The second section describes the thermal effects: the thermo-mechanical and the Marangoni effects caused by a local temperature gradient. It also presents the thermal assumptions, equations and numerical calculation methods.

The thermal equations are:

- the Fourier equation,
- the surface heat flux equation,
- the Marangoni equation,
- the thermal expansion equation,
- the linear elasticity equation.

The hydrodynamic and thermal theories are combined to create a model regrouping the parameters influencing the scuffing initiation risk. The algorithm of the numerical model is detailed in the last section.

2.2 Hydrodynamic theory

2.2.1 Piston rings/cylinder liner

By neglecting the free gap, the piston rings geometry is considered being a torus. The first and second rings have a parabolic carrying surface shape, whilst the third ring has usually two flat faces. The different carrying surface shapes are shown in figure 2.4. The compression ring is the main interest of this study as it is the closest to the combustion chamber so it is exposed to the most severe operating conditions. Its radius of curvature R_x is considered constant for calculation purposes and its surface is considered being smooth.

The cylinder liner or cylinder sleeve is the inner wall of the cylinder. Because of the honing process, the liner texture is composed of plateaux and cross-hatched grooves. This micro-geometry has an impact on the contact which can be beneficial. Thorough research projects on this topic are still going on worldwide to optimize the texturing geometry to enhance the tribological performance of the contact [104]. Hu et al. [105] demonstrated that a shallow groove texture with optimum groove density is beneficial for non-flat ring friction and for a flat ring a sparse groove pattern with optimum groove depth is required. In addition, the liner texture improves the oil distribution in the contact as demonstrated by Organisciak et al. [106]. To simplify the model by decreasing the number of parameters, the liner surface is considered a smooth surface in the current study.

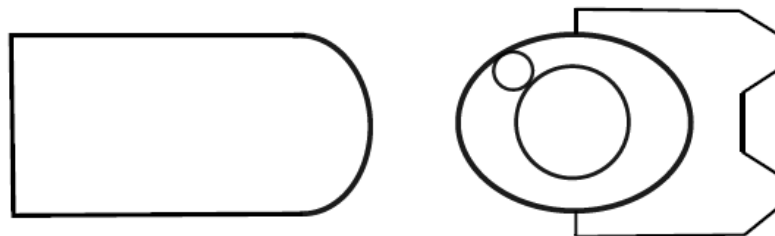


Figure 2.4: Ring cross sections

2.2.2 Geometry and calculational domain

Considering the three piston rings and the cylinder liner pack as a single model to study the PRCL contact is complex. Each piston ring is studied separately. The oil distribution varies along the circumferential direction, so a 2D model is needed to fully study the contact. x and y represent respectively the axial (motion) and the circumferential directions. The problem parameters such as the velocity, the contact load and the ring geometry are considered being constant in time thus a stationary analysis is applied.

Two main parameters limit the calculational domain width in the x -direction:

- the ring axial thickness,
- the degree of starvation.

Figure 2.5 shows the contact domain. x_a is the initial position of the ring at t_0 while x_b is the last position of the ring after a short time t_f . Based on the fact that the oil film thickness is small compared to the nominal ring radius $\phi/2$, the domain in the y -direction is flat. The choice of the values of y_a and y_b is related to the boundary conditions and the width of the domain needed for the study.

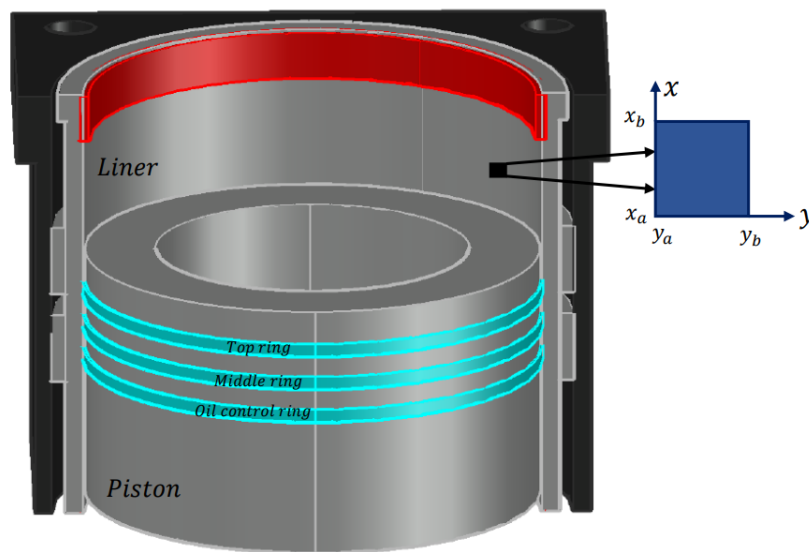


Figure 2.5: Contact zone model

2.2.3 Hydrodynamic operating assumptions

Several assumptions have been used to simplify the hydrodynamic model:

- the crucial one is that the PRCL contact is considered as a hydrodynamic lubricated contact, which means that the contacting surfaces are rigid,
- the ring velocity is constant along the x -direction and equal to the mean speed as its variation has no primary effect on scuffing initiation (see paragraph 2.1),
- the lubricant properties (viscosity and density) are considered constant in the contact and independent of the local temperature and pressure,
- the surface roughness is considered constant and the surface texturing is not taken into consideration to decrease the number of the problem parameters. Moreover, precursor scuffing initiation, the wear process removes the surface texturing and creates a mirror-like surface (see paragraph 2.1).

- the squeeze is negligible which describes the variation of the film thickness as a function of time.

2.2.4 Lubricant supply to the contact

This section describes the oil supply regimes.

2.2.4.1 Fully flooded lubrication

Figure 2.6 shows the oil distribution in the PRCL contact in the fully flooded lubrication regime. In this case, it is assumed that the inlet meniscus position tends to $-\infty$ so the ring shape in the x -direction is similar to an infinite parabola and the contact zone is filled with oil.

In reality, the ring is neither infinitely thick nor is the contact endlessly supplied with lubricant. Hence the importance of introducing the starved lubrication condition in the study to get closer to reality.

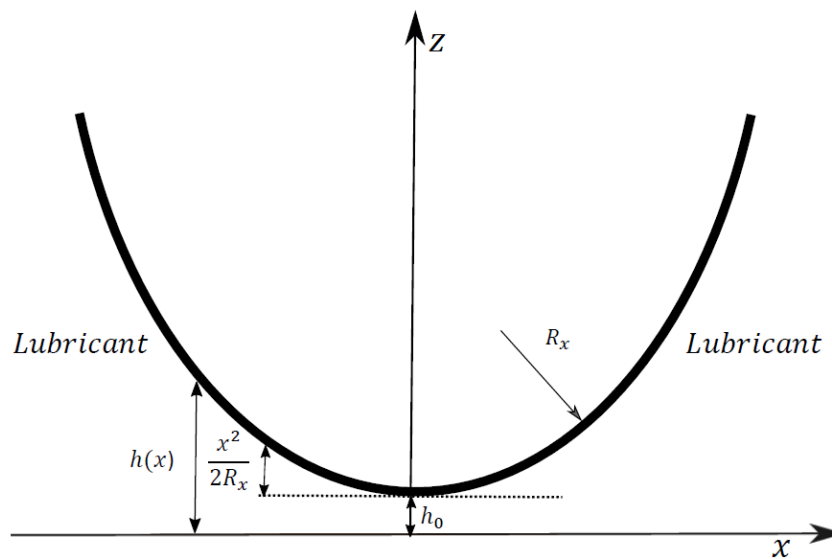


Figure 2.6: Fully flooded lubrication regime

2.2.4.2 Starved lubrication

Lack of lubricant: Figure 2.7 shows the oil distribution in starved lubrication condition, where a limited amount of oil is available in the contact.

Geometric starvation: A second reason for starvation is the ring geometry. The position of the inlet meniscus x_a , where the pressure generation initiates, depends on the ring

thickness and defines the degree of starvation. The pressurized zone is narrower than the one in fully flooded conditions.

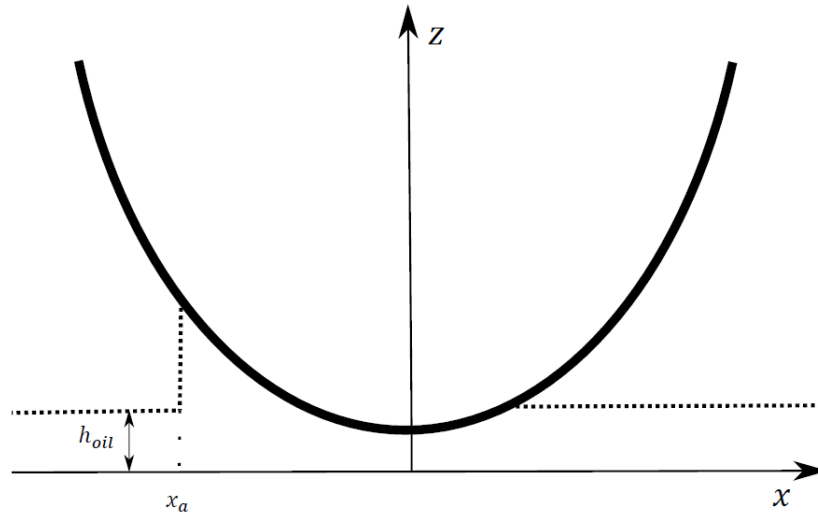


Figure 2.7: Starved lubrication regime

2.2.5 Equations

2.2.5.1 Film thickness equation

The film thickness equation (equation 2.1) describes the gap between the two contact bodies as shown in figure 2.6. It is composed of the following terms:

- the minimum film thickness h_0 ,
- the compression ring shape, which is a parabola with a radius of curvature R_x .

$$h(x, y) = h_0 + \frac{x^2}{2R_x} \quad (2.1)$$

Note that the oil film thickness can be measured using several methods [107]

- electrical methods, such as resistance-induced and capacitance-based,
- optical methods, such as laser-induced fluorescence,
- acoustic methods, such as ultra sound reflectance

Moreover, the film thickness varies along an engine stroke because of the variation of the ring velocity. At mid stroke, the velocity is high and the oil film is thick whilst, at the top/bottom dead center, the velocity is low and the oil film is thin [107].

2.2.5.2 Oil distribution equation

Because of a non-uniform oil distribution, a local starvation might occur in the contact. The oil distribution shown in figure 2.8 is used to model the local lack of lubricant. The equation of the distribution is given in equation 2.2.

$$h_{oil}(y) = h_{mean} - h_{var} \cos\left(\frac{2\pi y}{\lambda}\right) \quad (2.2)$$

where:

- h_{mean} is the average oil film thickness,
- h_{var} is the oil variation with respect to h_{mean} , it defines the maximum and the minimum thickness of the film at the inlet of the contact,
- λ is the wavelength.

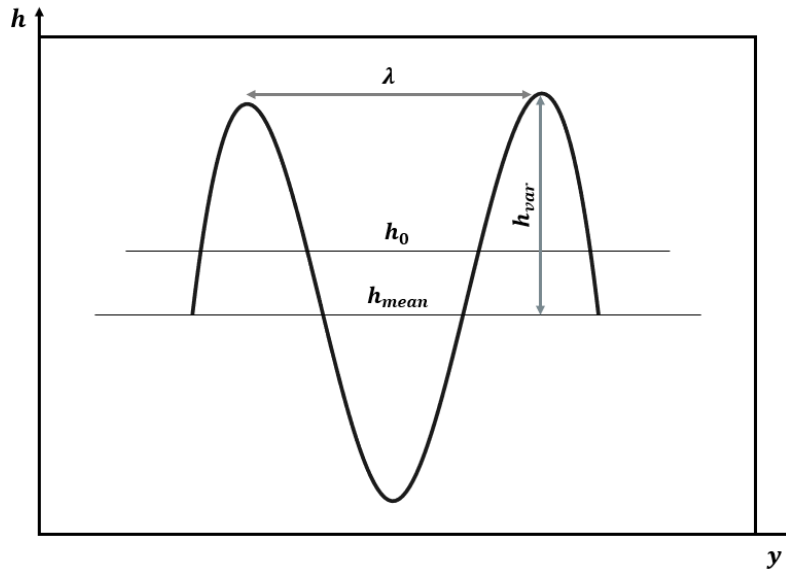


Figure 2.8: Oil distribution geometry

2.2.5.3 Reynolds equation

The Reynolds equation describes the flow of a thin film occurring between two surfaces. The iso-viscous, constant density and steady-state equation is:

$$\frac{1}{12\eta} \frac{\partial}{\partial x} \left(h^3 \frac{\partial p}{\partial x} \right) + \frac{1}{12\eta} \frac{\partial}{\partial y} \left(h^3 \frac{\partial p}{\partial y} \right) = u_m \frac{\partial h}{\partial x} \quad (2.3)$$

The pressure solution obtained from the Reynolds equation is either positive in the converging gap ($\partial h/\partial x < 0$) or negative in the diverging gap ($\partial h/\partial x > 0$). When the pressure goes below zero, the oil evaporates and a discontinuity of the film is created in this zone. This is the cavitation process. The pressure is limited to the lubricant vapor pressure. Since the vapor pressure is negligible compared to the contact pressure, it is considered null so $p=0$ in the cavitated zone.

2.2.5.4 Reynolds equation with starvation

To analyze the fluid film in a starved condition, a parameter θ is introduced, which is the void fraction (1-ratio between the oil film thickness (h_{oil}) and the geometry gap between the surfaces (h)). The Reynolds equation is then modified as given in equation 2.4 to take into consideration θ and to describe the starved lubrication regime. Its value ranges between 0 and 1 ($0 \leq \theta \leq 1$).

$$\frac{1}{12\eta} \frac{\partial}{\partial x} \left(h^3 \frac{\partial p}{\partial x} \right) + \frac{1}{12\eta} \frac{\partial}{\partial y} \left(h^3 \frac{\partial p}{\partial y} \right) = u_m \frac{\partial((1-\theta)h)}{\partial x} \quad (2.4)$$

2.2.5.5 Dimensionless equations

The values of the dimensionless parameters vary around 1, which enables one to obtain maximum precision in the numerical calculations. In addition, they limit the total number of parameters by regrouping them.

Table 2.1 defines the variables with a 0 index. Upper case letters denote the dimensionless parameters:

$$X = \frac{x}{x_0} \quad (2.5)$$

$$Y = \frac{y}{y_0} \quad (2.6)$$

$$Z = \frac{z}{z_0} \quad (2.7)$$

$$\Lambda = \frac{\lambda}{\lambda_0} \quad (2.8)$$

$$H = \frac{h}{h_0} \quad (2.9)$$

$$H_{mean} = \frac{h_{mean}}{h_0} \quad (2.10)$$

$$H_{var} = \frac{h_{var}}{h_0} \quad (2.11)$$

$$P = \frac{p}{p_0} \quad (2.12)$$

$$W_1 = \frac{w_1}{w_0} \quad (2.13)$$

x_0	y_0	h_0	λ_0	p_0	w_0
a	a	h_0	a	$12\eta u_m a / h_0^2$	$12\eta u_m a^2 / h_0^2$

Table 2.1: Hydrodynamic dimensionless parameters

The dimensionless equations are:

Reynolds equation

$$\frac{\partial}{\partial X} \left(H^3 \frac{\partial P}{\partial X} \right) + \frac{\partial}{\partial Y} \left(H^3 \frac{\partial P}{\partial Y} \right) - \frac{\partial((1-\theta)H)}{\partial X} = 0 \quad (2.14)$$

Film thickness equation

$$H(X, Y) = 1 + \frac{a^2}{2R_x h_0} X^2 \quad (2.15)$$

Lubricant distribution equation

$$H_{oil}(Y) = H_{mean} - H_{var} \cos\left(\frac{2\pi Y}{\Lambda}\right) \quad (2.16)$$

2.2.6 Hydrodynamic model implementation

The lubricant is supplied to the PRCL contact by an oil flung and an oil jet spray. They do not distribute the oil uniformly in the contact and only a small amount of oil reaches the top ring, it operates under starved conditions [108]. As a result, drier zones may temporarily exist in the contact due to the lack of lubricant and the rings operate under a starved regime.

The ring displacement along the liner redistributes the oil, hence helps to avoid starvation. In order to study the ring displacement impact on the lubricant distribution, the oil geometry is imposed as non-uniform in the circumferential direction at the inlet of the contact as given in equation 2.16.

A mass-conserving solver [109] is used for Reynolds equation resolution. The calculation outputs are the pressure and the oil distributions after the passage of the ring along the liner. The redistribution is studied and quantified by comparing the oil geometry imposed and the one obtained after the ring passage.

2.3 Thermal effect

The heat exchange occurring in the PRCL contact has an impact on the lubrication mechanism and then on scuffing initiation.

To describe locally the scuffing initiation, a local study of the thermal effect is required. The heat exchange generates a temperature gradient on the contact surface. As the temperature is no longer uniformly distributed in the body, a localized surface deformation can take place as a result of the thermo-mechanical effect and a local lack of lubricant can appear because of the Marangoni effect. The thermal impact on the lubricant distribution and then on the contact performance is studied.

2.3.1 Geometry and calculational domain

The temperature of the liner and the ring surfaces is considered initially constant and equal to T_0 , (assuming that the conductivity is the same in all directions of the material, thus the heat transferred from the combustion chamber to the surfaces is uniformly diffused in the bodies). However, under certain conditions, when considering the occurrence of a temporarily local lack of lubricant due to non-uniform oil distribution in the contact, the coefficient of friction increases. Then an additional heat flux is locally generated. The additional heat flux generated ($q_{heated-zone}$) is given in the equation below:

$$q_{heated-zone} = \zeta \mu p_{contact} u_m \quad (2.17)$$

where μ is the coefficient of friction, $p_{contact}$ is the contact pressure applied to the contact, u_m is the mean velocity of the ring along the stroke and ζ is the ratio of the heat exchange occurring between the liner and the ring. Its value ranges between 0 and 1. 0 means that there is no heat transferred to the surface whilst 1 means that the heat is totally transferred to the surface.

The thermo-mechanical modeling and the calculation of the thermal deformation of the piston ring are carried out via COMSOL Multiphysics software using the finite elements method as detailed in appendix A. The thermal ring model is shown in figure 2.9. The localized heated zone (red zone on the figure) refers to the additional heat flux generated as a result of an increase in the coefficient of friction due to a local lack of lubricant and causes a temperature increase. To simulate the worst-case scenario, the heat is assumed to be totally transferred to the ring surface, the value of ζ is 1. For more details about the piston ring modeling see appendix B.

For the study of the Marangoni effect occurring on the liner, the temperature distribution on the surface is required. Figure 2.10 shows the liner thermal model used for the temperature distribution calculation. As the heat flux generated is moving along the liner surface, thus the model is a transient 3D model. However, as mentioned in paragraph 2.1, the variation of the temperature gradient along the stroke has no primary influence on the scuffing initiation so the heat flux is averaged (q_{mean}) along the axial direction (direction of movement x) and the surface is considered infinitely long in the x -direction, thus the 3D transient model becomes a stationary 2D model. The transition from the 3D model

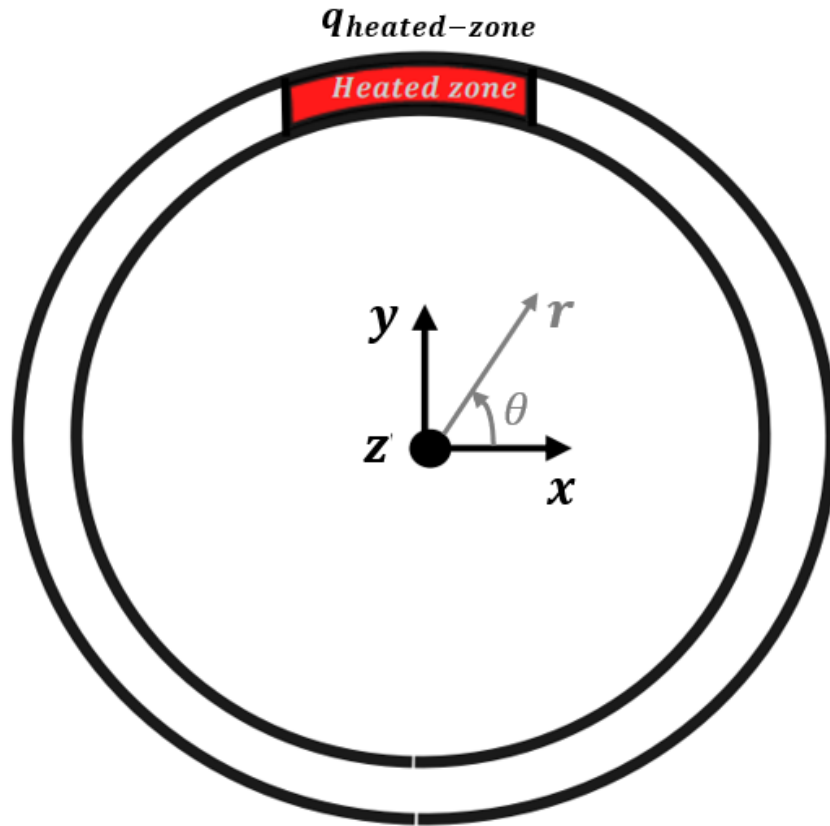


Figure 2.9: Ring thermal model

to the 2D model and the expression of q_{mean} are detailed in appendix C. The domain size (s_d) is wide enough to guarantee that the Dirichlet boundary conditions do not influence the temperature increase calculation.

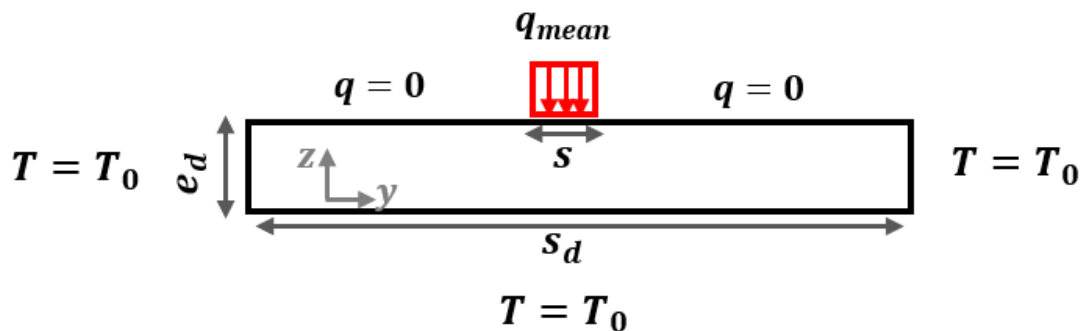


Figure 2.10: 2D liner thermal model

2.3.2 Thermal operating assumptions

Several assumptions have been used to simplify the thermal model:

- the material is considered to be isotropic; the conductivity is the same in all directions,
- the thermal deformation caused by the temperature increase is considered to be linear,
- no heat stored in the lubricant,
- the heat exchange occurring between the liner and the ring surfaces with their surroundings is not studied in the current model,
- Neumann boundary conditions are used to simulate the heat flux generated in the starved/heated zone (q imposed), whilst Dirichlet boundary conditions (T_0 imposed) are used elsewhere, where T_0 is the nominal liner temperature at which minimum friction occurs, its upper bound ranges around 140° C [34]. This is the simplest boundary condition to be considered to simplify the model,
- the heat equation calculations are stationary.

2.3.3 Thermal Marangoni effect

The lubricant surface tension or also known as inter-facial tension is the force acting on the lubricant surface. It depends on the local surface temperature. As mentioned in paragraph 2.3, a temperature gradient is generated on the liner surface as a result of an additional local heat flux, which in turn leads to a surface tension gradient. As a result, a lubricant displacement occurs. This phenomenon is called the thermal Marangoni effect. Figure 2.11 shows the Marangoni effect taking place as a result of the surface tension gradient. The lubricant flows from the high-temperature zone (low surface tension γ) to the low-temperature zone (high surface tension γ). The lubricant is submitted to the Marangoni ($\tau_{Marangoni}$) and viscous stresses ($\tau_{viscous}$). The lubricant distribution perturbation occurring along the y direction is the interest of this study.

2.3.4 Equations

The thermal equations are detailed in this section:

2.3.4.1 2D Fourier heat equation

The stationary heat equation without an internal heat generation is shown below:

$$\frac{\partial}{\partial y} \left(\alpha_y \frac{\partial T}{\partial y} \right) + \frac{\partial}{\partial z} \left(\alpha_z \frac{\partial T}{\partial z} \right) = 0 \quad (2.18)$$

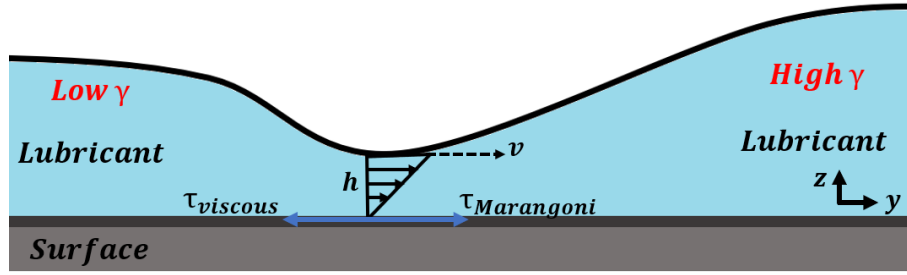


Figure 2.11: Thermal Marangoni model

where α_y, α_z are the conductivity in both directions. As mentioned in paragraph 2.3.2, the material is isotropic hence $\alpha_y = \alpha_z = \alpha$.

2.3.4.2 Thermal boundary conditions

The boundary conditions considered for the liner and ring surfaces are presented respectively in figures 2.10 and 2.9. Neumann boundary conditions (q) are imposed as given in the equation below to simulate the heated zone where a heat flux is generated due to a local lack of lubricant.

$$q = -\alpha \frac{\partial T}{\partial z} \quad (2.19)$$

Dirichlet conditions are used elsewhere, so a reference temperature T_0 is imposed.

2.3.4.3 Thermal expansion

Due to the temperature variation, a thermal expansion occurs causing a shape variation of the surface. The strain rate (ϵ_{th}) depends on the coefficient of thermal expansion of the material (α_{th}) as shown in equation 2.20.

$$\epsilon_{th} = \alpha_{th}(T - T_0) \quad (2.20)$$

2.3.4.4 Linear elasticity

The thermal stress and deformation for elastic material are connected by a linear equation similar to Hooke's law as shown in equation 2.21.

$$\sigma_{th} = E\epsilon \quad (2.21)$$

2.3.4.5 Lubricant surface tension

The local lubricant surface tension depends on the local temperature. The increase in the latter leads to a decrease in the surface tension of the lubricant as given in equation 2.22.

$$\gamma = \gamma_0 \left(1 - \frac{T}{T_c}\right)^n \quad (2.22)$$

where T_c is the critical temperature of the lubricant. The critical point represents the state at which two phases (liquid-vapor) of fluid become indistinguishable from one another [8]. Note that at the critical temperature, the lubricant surface tension is null. The phase diagram of fluid is presented in figure E.3.

2.3.4.6 Lubricant viscosity

The equation used to calculate the lubricant viscosity as a function of the local temperature is shown below. The viscosity decreases when the temperature increases.

$$\log(\log(\eta + 0.7)) = a \log(T) + b \quad (2.23)$$

where a and b are constants depending on the lubricant. The lubricant viscosity curve as a function of the temperature is presented in figure E.1.

2.3.4.7 Marangoni effect equations

As mentioned in paragraph 2.3.3 the lubricant is exposed to the viscous and the Marangoni stresses. The Marangoni stress is composed of the surface tension gradient along the y -direction as given in equation 2.24. The viscous stress generated in the film is a function of the oil film thickness (h), velocity (v) and viscosity (η) as given in equation 2.25.

$$\tau_{Marangoni} = \frac{\partial \gamma}{\partial y} \quad (2.24)$$

$$\tau_{viscous} = \eta \frac{v}{h} \quad (2.25)$$

The variation of the oil film thickness because of the Marangoni effect is given in equation 2.28. It results of the combination of two equations:

- the equilibrium of the Marangoni and the viscous stresses ($\tau_{Marangoni} = \tau_{viscous}$), so the equation of the oil velocity is obtained:

$$v = \frac{h}{\eta} \frac{\partial \gamma}{\partial y} \quad (2.26)$$

- the equilibrium of the variation of the oil film over time ($\partial h / \partial t$) and the Couette flux ($\partial \phi_c / \partial y$) along the y direction ($\partial h / \partial t = \partial \phi_c / \partial y$),

where

$$\phi_c = \frac{vh}{2} \quad (2.27)$$

The velocity term in equation 2.27 is replaced by equation 2.26 and the second equilibrium is solved to obtain the Marangoni equation:

$$\frac{\partial h}{\partial t} = -\frac{\partial}{\partial y} \left(\frac{h^2}{2\eta} \frac{\partial \gamma}{\partial y} \right) \quad (2.28)$$

2.3.4.8 Dimensionless equations

The dimensionless parameters are given below and table 2.2 defines the variables with 0 index. The dimensionless variables are:

$$\bar{T} = \frac{T}{T_0} \quad (2.29)$$

$$Q = \frac{q}{q_0} \quad (2.30)$$

$$\bar{\gamma} = \frac{\gamma}{\gamma_0} \quad (2.31)$$

$$\bar{\eta} = \frac{\eta}{\eta_0} \quad (2.32)$$

$$\bar{t} = \frac{t}{t_0} \quad (2.33)$$

y_0	z_0	\bar{T}	q_0	γ_0	η_0	t_0
s	s	T_0	$\alpha_{th}T_0/s$	γ_{T_0}	η_{T_0}	$s^2\eta_0/h_0\gamma_0$

Table 2.2: Thermal dimensionless parameters

The thermal dimensionless equations are given below:

2.3.4.9 Heat equation

$$\frac{\partial^2 \bar{T}}{\partial Y^2} + \frac{\partial^2 \bar{T}}{\partial Z^2} = 0 \quad (2.34)$$

2.3.4.10 Marangoni equation

$$\frac{\partial H}{\partial \bar{t}} = -\frac{\partial}{\partial Y} \left(\frac{H^2}{2\bar{\eta}} \frac{\partial \bar{\gamma}}{\partial Y} \right) \quad (2.35)$$

2.3.5 Thermal theory calculation

2.3.5.1 Heat equation resolution

The thermal system to be solved in order to obtain the temperature distribution generated on the liner surface (see figure 2.10) required for the Marangoni calculation is:

$$[A]\{\bar{T}\} = \{f\} \quad (2.36)$$

where A is a matrix, \bar{T} is the unknown temperature field vector to be calculated and f is the right hand side depending on the boundaries conditions. The heat equation and the Neumann boundary condition (surface flux) are discretized using second order centered scheme as shown in the equation below:

$$\frac{\bar{T}_{j+1,k} - 2\bar{T}_{j,k} + \bar{T}_{j-1,k}}{(\Delta Y)^2} + \frac{\bar{T}_{j,k+1} - 2\bar{T}_{j,k} + \bar{T}_{j,k-1}}{(\Delta Z)^2} = 0 \quad (2.37)$$

where j and k are Y and Z indices respectively, ΔY and ΔZ are the space mesh sizes. The equation below gives the discretization of the boundary condition:

$$Q_{j,k} = \frac{\bar{T}_{j,k+1} - \bar{T}_{j,k-1}}{2\Delta Z} \quad (2.38)$$

As the flux boundary condition is imposed on the surface ($k=0$), the ghost points method is applied to the discretization, where the points at $k=-1$ are virtual.

$$Q_{j,0} = \frac{\bar{T}_{j,1} - \bar{T}_{j,-1}}{2\Delta Z} \quad (2.39)$$

Once the system is defined, the temperature field is calculated by a simple matrix calculation:

$$\{\bar{T}\} = [A]^{-1}\{f\} \quad (2.40)$$

The 2D liner surface model with the discretized domain are shown in figure C.5.

2.3.5.2 Thermal expansion calculation

As mentioned in paragraph 2.3.2 the material deformation is assumed to be elastic-linear. The thermal deformations and stresses are calculated via COMSOL Multiphysics software and the calculation procedure is detailed in appendices A and B. The ring thermal deformation along the radial direction is the interest of this study. As the ring is thin in the axial direction (t_{axial} of the ring is for about a few millimeters), plane-stress applies for the deformation calculation [110] and the problem is solved using the finite elements method.

2.3.5.3 Marangoni equation resolution

The Marangoni equation is a 1D parabolic equation. The discretization of the equation in space and time is given in the equation below:

$$H_j^{n+1} = H_j^n - \frac{\Delta \bar{t}}{\Delta Y^2} \left(\frac{\bar{\gamma}_{j+1} - \bar{\gamma}_j}{4} \right) \frac{(H_{j+1} + H_j)^2}{(\bar{\eta}_{j+1} + \bar{\eta}_j)} - \frac{\Delta t}{\Delta Y^2} \left(\frac{\bar{\gamma}_{j-1} - \bar{\gamma}_j}{4} \right) \frac{(H_{j-1} + H_j)^2}{(\bar{\eta}_{j-1} + \bar{\eta}_j)} \quad (2.41)$$

where n and j are time and space indices respectively, ΔY is the space mesh size and $\Delta \bar{t}$ is the time step.

2.4 Scuffing prediction model

Figure 2.12 regroups the parameters and phenomena leading to scuffing. The three major phenomena are:

- the thermo-mechanical effect,
- the thermal Marangoni effect,
- the oil redistribution effect.

Assuming that a local lack of lubricant can temporarily occur in the contact due to a non-uniform distribution of lubricant, then the coefficient of friction increases. The latter generates an additional heat flux. The starvation zone, where the heat flux is generated is called the starved or the heated zone. As a result, a temperature gradient is generated. Due to the temperature variation occurring in the contact, the thermo-mechanical effect causes a ring deformation. An additional load is then considered to the contact which is equal to the one needed to bend the ring into its original position. Subsequently, the heat flux increases as it depends on the contact pressure (equation 2.17). The lubricant surface tension and viscosity gradients are calculated in function of the temperature (2.22 and 2.23) and then the minimum film thickness is calculated via:

- equation 2.42 that is obtained by a numerical study carried out by Moes [111] in a fully flooded lubrication regime,

$$h_0 = 2.45 \frac{\eta u_m R_x}{w_1} \quad (2.42)$$

- equation 2.43 that is obtained by Biboulet et al [112] in a starved lubrication regime.

$$h_0^3 \left(\frac{5.745 R_x^2}{x_a^4} \right) + h_0^2 \left(\frac{4.809 R_x}{x_a^2} \right) + h_0 = 2.45 \frac{\eta u_m R_x}{w_1} \quad (2.43)$$

where w_1 is the load per unit length ($w_1 = p_{contact} t_{axial}$). Note that η used in these equations is calculated with the highest temperature. When the contact load increases, the film thickness decreases leading to an increase in the coefficient of friction (μ). The latter is obtained by the Stribeck curve as a function of the film thickness (h_0) and the surface roughness (σ), as shown in figure 2.13. From the curve, it can be concluded that the lower the film thickness, the higher the coefficient of friction and the risk for boundary lubrication regime. The values shown in the curve are generic ones. In fact, the coefficient of friction depends on the types of lubricant and on the surface materials as demonstrated by Neville et al. [113] when they identified experimentally the coefficient of friction for several material couples lubricated by several lubricant types. Note that the surface roughness (σ) is considered constant in the model.

The coefficient of friction combined with the additional load obtained due to the thermo-mechanical effect increases the heat flux generated thus the temperature which constitutes a positive feedback loop. The progressive increase in the temperature might cause it to reach the limit temperature when lubricant desorption initiates leading to a sudden increase in friction. Lubricant additive has a major contribution to scuffing prevention. In this study, its contribution is limited to its desorption influence on friction and then scuffing. Note that the study is carried out for a given lubricant in order to predict the critical operating conditions which lead to scuffing.

As a result of the lubricant surface tension gradient, the Marangoni effect occurs and causes lubricant displacement. These two effects, the thermo-mechanical and the Marangoni effects accentuate the risk of scuffing initiation. In addition, the lubricant distribution is affected by the displacement of the ring along the liner. It redistributes the oil on the surface and helps to avoid local starvation, thus scuffing initiation. The scuffing loop regroups the three mentioned phenomena in order to study their coupled contribution to scuffing initiation.

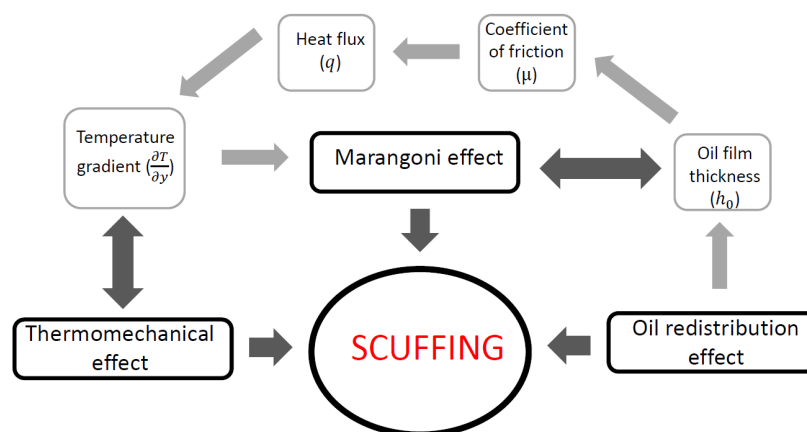


Figure 2.12: Scuffing loop model

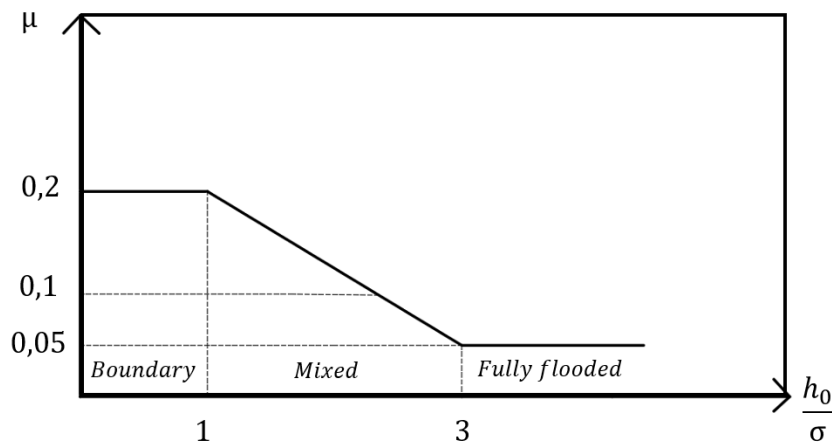


Figure 2.13: Stribeck curve: coefficient of friction as a function of the film thickness over the surface roughness

2.5 Conclusion

This chapter presented the numerical model used to study the scuffing initiation prediction in the PRCL contact. Starvation and thermal effects are major causes of scuffing. Local starvation can result from the two following processes:

- the non-uniform distribution of the lubricant along the liner,
- the Marangoni effect in response to the surface tension gradient on the interface lubricant/liner surface.

The first source is simulated by the model via the Reynolds equation that accounts for θ , the void ratio. The oil and pressure distributions in the contact after the ring passage along the liner are calculated in order to study the influence of the ring passage on the oil distribution and then on scuffing.

The second source is a thermal one. The Marangoni effect is related to the surface tension gradient caused by the temperature field generated on the surface. The oil tends to flow from the zone with low surface tension (high temperature) to the zone with high surface tension (low temperature). As a result, a localized lack of lubricant might occur. The Marangoni effect is modeled by quantifying the surface moved in response to the local temperature variation and surface tension gradient. Moreover, the thermo-mechanical effect influences scuffing initiation. The local increase in the temperature due to a local heat flux causes a thermo-mechanical ring deformation. The force needed to bend the ring into its initial position is considered as an additional load to the contact. It increases the contact pressure and then the surface heat flux, which initiates a positive feedback loop. The complexity of this study is due to the plethora of interacting parameters influencing scuffing. A detailed schematic algorithm for the model is presented in figure 2.14. The scuffing initiates via one or both of the following situations :

- the temperature obtained by the thermo-mechanical effect exceeds the temperature limit of the oil additive desorption, which causes a sudden increase in friction,
- the oil displacement caused by the Marangoni effect is more pronounced than the redistribution caused by the ring passage.

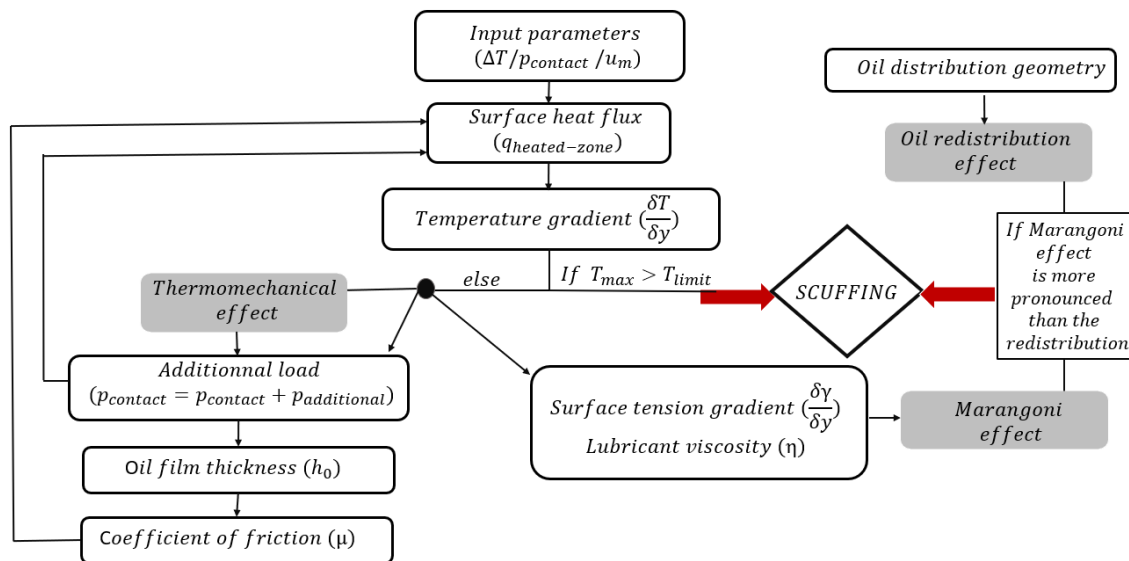


Figure 2.14: Detailed scuffing algorithm

Chapter 3

Scuffing initiation caused by local starvation in the piston ring cylinder liner

Contents

3.1	Introduction	44
3.2	Model presentation	44
3.2.1	Lubricant distribution model	44
3.2.2	Contact load	45
3.2.3	Model input parameters	49
3.3	Lubricant distribution	50
3.3.1	Marangoni effect	50
3.3.2	Ring passage effect	55
3.3.3	Interpretation	61
3.4	Scuffing initiation limit	61
3.4.1	Contact load depends on the ring tension only	62
3.4.2	Composed contact load	63
3.4.3	Interpretation	64
3.5	Conclusion	65

3.1 Introduction

The contribution of the Marangoni and the ring displacement effects to scuffing initiation is presented in this chapter. The Marangoni effect might accelerate the scuffing initiation since it provokes oil starvation by causing an oil displacement from the warmer contact zones to the colder ones. On the other hand, the passage of the ring along the liner redistributes the oil in the contact, which helps to prevent starvation, thus avoids scuffing. This chapter analyses the influence of lubrication starvation and distribution on the scuffing initiation. The first section presents the parameters influencing the lubricant distribution. Then, the oil displaced due to the Marangoni effect and the oil redistributed due to the ring passage are quantified as a function of the problem parameters in the second section. In the third section, the scuffing initiation limit is quantified and presented in charts as a function of the operating parameters. The last section summarizes the major results obtained in this chapter.

3.2 Model presentation

3.2.1 Lubricant distribution model

Figure 3.1 summarizes the model of the lubricant distribution in the contact. A detailed explanation of the algorithm presented in the figure is given below:

Assuming that under certain operating conditions, a local lack of lubricant might temporarily occur due to an oil displacement and a non-uniform oil distribution in the contact. As a result, the coefficient of friction increases (figure 2.13) which in turn leads to a temperature increase of the liner surface (ΔT) compared to the initial surface temperature (T_0). The surface tension and viscosity gradients depending on the temperature are obtained (equations 2.22 and 2.23). The minimum oil film thickness (h_0) is then defined depending on the oil supply regime detailed in paragraph 2.2.4:

- if the oil supply regime is fully flooded, the contact is considered to be filled with oil which is the best lubrication condition, h_0 is calculated using equation 2.42,
- if oil starvation is taken into consideration, which means that the contact is partially filled with oil, h_0 is calculated by equation 2.43.

A Marangoni calculation is then carried out to predict the oil variation (h_{var}) caused by surface tension gradient compared to the mean film thickness (h_{mean}) which is considered to be equal to the minimum film thickness ($h_{mean} = h_0$).

The last part quantifies the following surfaces:

- the surface displaced due to the Marangoni effect ($S_{Marangoni}$) as a function of the temperature increase (ΔT), the minimum oil film thickness (h_0), the lubricant surface tension and viscosity gradients. In fact, the volume flow rate of the displaced oil is presented as a moving surface in order to compare it to the one moved due to the ring passage,

- the surface moved due to the ring passage ($S_{redistributed}$) as a function of the minimum oil film thickness and the oil geometry distribution parameters (h_{mean} , h_{var} and λ).

If $S_{Marangoni}$ is larger than $S_{redistributed}$ ($S_{Marangoni} > S_{redistributed}$), which meaning that the lubricant starvation caused by the Marangoni effect is more pronounced than the lubricant redistribution caused by the ring passage, scuffing might initiate. Else, when starvation is balanced by the oil redistribution, the local lack of lubricant is avoided and no risk of scuffing exists.

The purpose of this model is to study the contact performance when it is exposed to local heating yet the lubricant is re-supplied. The question to explore is that despite the local heating, will the contact perform normally when it is re-lubricated?

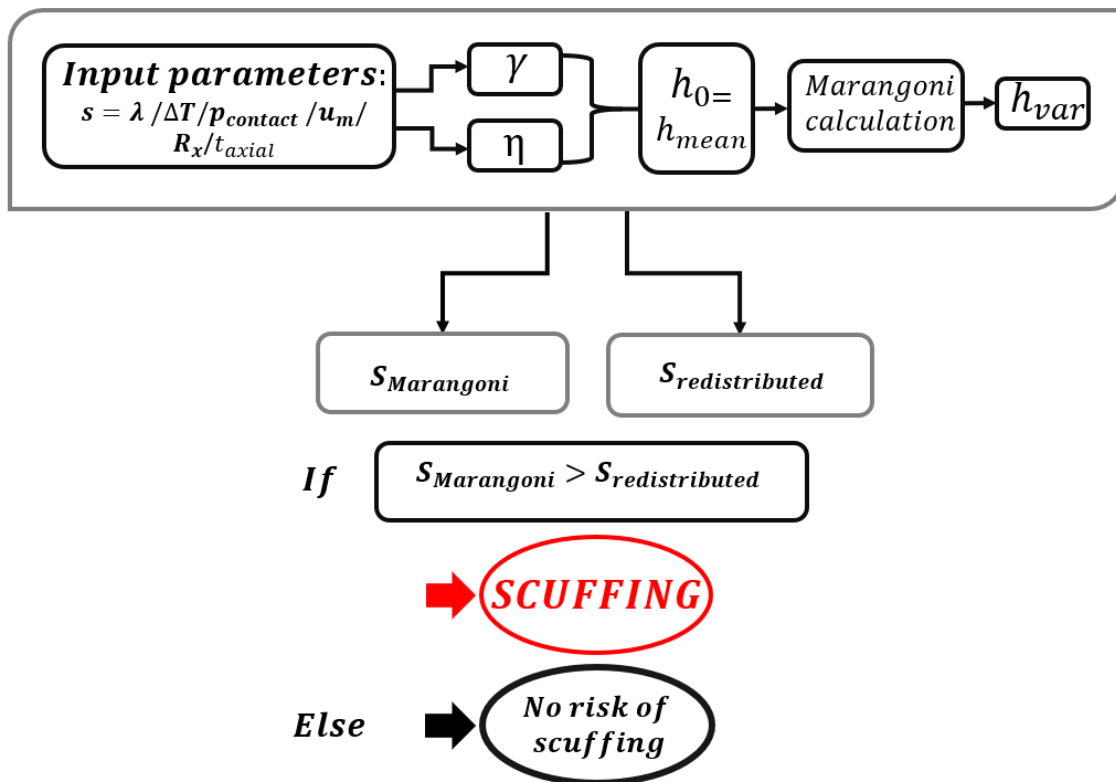


Figure 3.1: Lubricant distribution model

3.2.2 Contact load

The contact load which presses the piston ring against the cylinder wall is composed of the normal external loads as detailed below:

3.2.2.1 Ring tension

The rings are self-tensioning springs with a free gap. When installed, the free gap is reduced and elastic deformation is created. This deformation generates a spring force, hence a pressure against the cylinder wall as shown in figure 3.2.

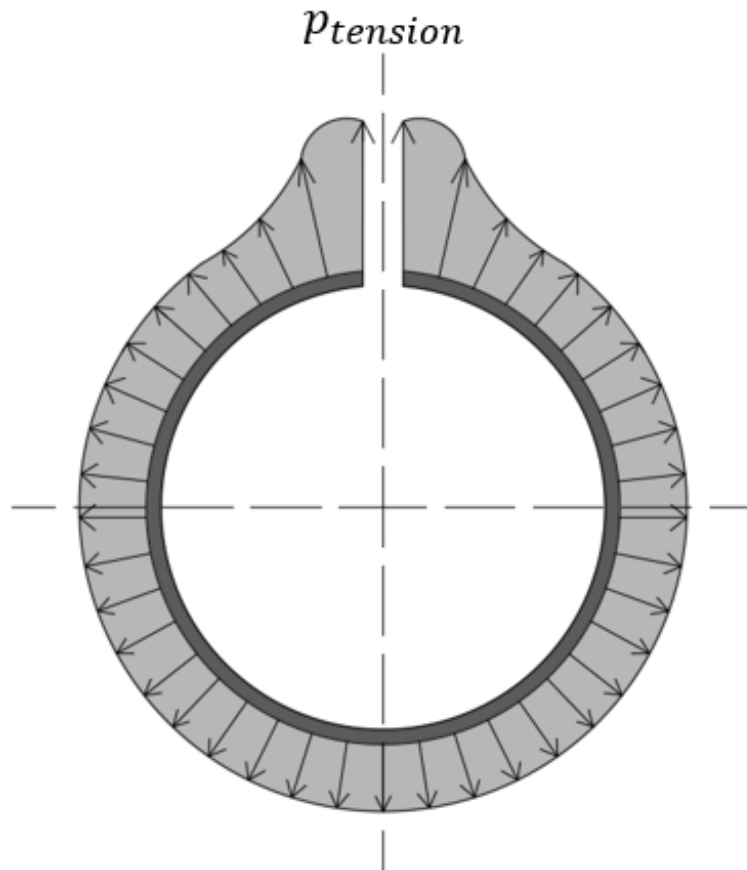


Figure 3.2: Radial pressure pattern of a piston ring

The mean radial pressure applied by the ring itself is calculated from the ring tension (F_{ring}) via the equation below:

$$p_{tension} = \frac{2F_{ring}}{\phi t_{axial}} \quad (3.1)$$

where ϕ is the nominal ring diameter and t_{axial} is the ring axial thickness. Appendix D details how equation 3.1 was obtained.

3.2.2.2 Thrust load

Figure 3.3 shows the major/minor thrust sides in the combustion stroke phase of the engine cycle. During the combustion stroke phase, the high-temperature and high-pressure gases push the piston down and the crankshaft rotates. Because of the charge caused by the angle of the connecting rod (F_r) and the charge caused by the combustion pressure (F_g) acting above the piston, the piston is pushed to one side of the cylinder wall called the major thrust side. This process is known as the piston slap [114] and the resulting load is known as the thrust load (F_{thrust}). In figure 3.3 the crankshaft rotation is clockwise, the major thrust side is on the left side of the cylinder wall and the minor thrust side is on the right side of the cylinder.

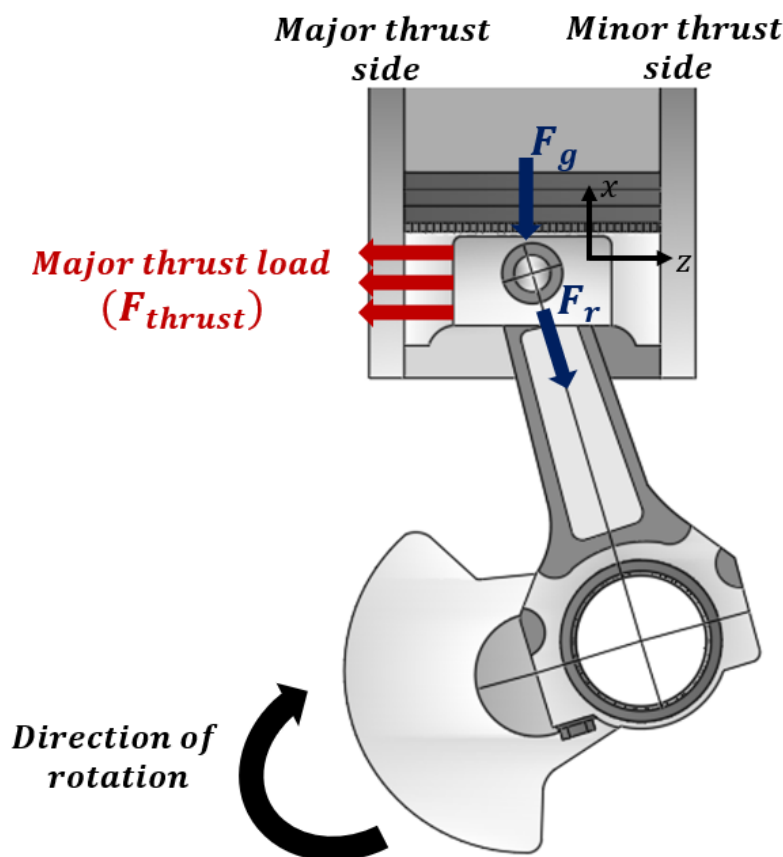


Figure 3.3: Power stroke phase of the engine

As the piston slap is an important source of vibration and noise in internal combustion engines, research was carried out to study the conditions leading to piston slap occurrence during an engine cycle to reduce noise and vibration. The piston slap occurrence can be identified when the thrust load changes direction [115]. The minimum oil film thickness and the maximum heat transfer are other criteria of piston slap occurrence. When the

piston slap takes place, the piston-liner contact is intensified and the oil film thickness takes its minimal value [116]. Moreover, the piston slap is assumed when the maximum of energy is transferred to the cylinder surface [114]. Because the thrust load acts on one side of the cylinder wall, the radial pressure distribution of the ring is circumferentially uneven. The pressure is higher where the thrust load occurs and the pressure distribution can be presented as an ovality as shown in figure 3.4.

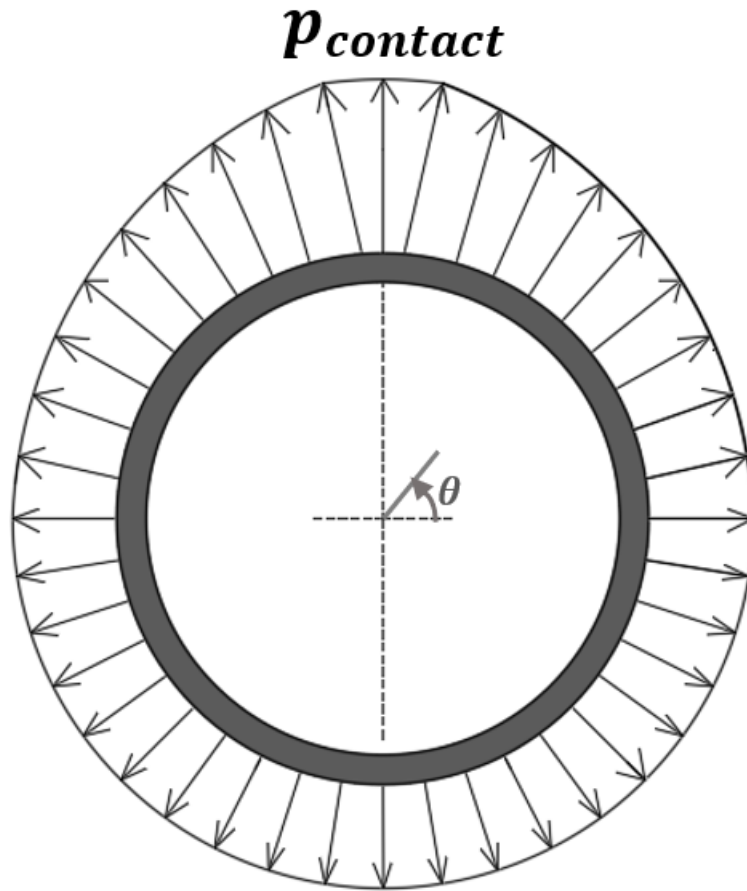


Figure 3.4: Radial pressure distribution of a piston ring

In this study, the thrust load distribution of an engine cycle is given and the thrust load is assumed to be acting on the ring surface circumferentially from $\theta=0$ to $\theta=\pi$ (see figure 3.4). The thrust load is averaged over the engine cycle (see paragraph 3.4.2), thus the pressure caused by the thrust load is considered constant. The mean pressure (p_{thrust}) is obtained as given below:

$$p_{thrust} = \frac{2F_{thrust}}{\pi\phi t_{axial}} \quad (3.2)$$

The total contact pressure that pushes the ring against the cylinder wall is the sum of the ring tension and the thrust pressures as given in the equation below:

$$p_{contact} = p_{tension} + p_{thrust} \quad (3.3)$$

3.2.3 Model input parameters

3.2.3.1 Operating parameters

Engine speed: The engine frequency in rpm (N) is one of the parameters impacting the lubricant distribution. It defines the mean ring velocity (u_m) and the time of a passage ($t_{passage}$).

Piston mean velocity: As the piston ring velocity varies along the stroke (low at the top and bottom dead centers and high at mid-stroke), the mean ring velocity (u_m) along the stroke is used in the model. It depends on the engine frequency in rpm and the stroke length (C) as shown in equation 3.4. It increases with the engine speed. As the engine speed and the stroke distance are both considered to be constants in the model, the piston velocity is also constant.

$$u_m = \frac{NC}{30} \quad (3.4)$$

Time of the ring passage: The time of the ring passage ($t_{passage}$) depends on the stroke length (C) and the piston mean velocity (u_m). It decreases with the piston speed as shown in the equation below:

$$t_{passage} = \frac{C}{u_m} \quad (3.5)$$

Thermal parameters: The thermal parameters are:

- the initial temperature of the liner surface which is considered to be constant (T_0),
- the temperature increase (ΔT) compared to the nominal temperature (T_0) which depends on the level of the heating occurring in the contact,
- the width of the starved zone where a heat flux is generated (s). As a local study is applied, s is small compared to the calculational domain and at the same time, it is relatively large enough for a temperature field generation. Its value ranges between 1 and 6.25 mm.

Lubricant properties: The initial lubricant properties such as the initial surface tension (γ_0) and the initial viscosity (η_0) at the initial temperature are input parameters in the model. They impact the surface tension and viscosity gradients hence determine the surface moved due to the Marangoni effect. The model is applied for a given lubricant.

Lubrication supply regime: The lubricant supply regime defines the oil quantity supplied to the contact (see paragraph 2.2.4 for more details), thus the minimum oil film thickness which is a vital parameter for the model and the scuffing initiation limit.

Initial lubricant geometry: The initial lubricant geometry is an input of the model allowing the simulation of the non-uniform oil distribution occurring in the circumferential direction. It is considered to be a sinusoidal function by defining the mean oil film thickness (h_{mean}), the variation (h_{var}) compared to h_{mean} and the wavelength (λ) (see paragraph 2.2.5.2).

The chosen operating and geometric parameters for the numerical model are detailed in appendix E.

3.3 Lubricant distribution

3.3.1 Marangoni effect

Assuming that a local lack of lubricant occurs in the contact which increases the coefficient of friction (as shown in the Stribeck curve in figure 2.13, the coefficient of friction increases when the minimum oil film thickness decreases). As a result, an additional heat flux is generated leading to a temperature increase in the starved/heated zone. In this section, the Marangoni effect is studied as a function of the temperature gradient occurring on the liner surface. Since it is more practical and concrete to choose a temperature increase as an input instead of a heat flux, the temperature increase (ΔT) compared to the nominal surface temperature (T_0) is chosen as a first step. Based on that, the heat flux to be imposed to obtain a temperature distribution on the liner surface with the chosen temperature increase is known. Note that the relation between the heat flux and the temperature increase is linear ($q = c\Delta T$), where c is a constant.

3.3.1.1 Temperature gradient

In order to analyze the temperature gradient generated on the liner surface as a result of the occurrence of a starved zone, a heat flux is imposed on the liner surface over the width of the starved zone s to obtain a temperature increase up to $20K$ in the starved zone. The thermal model is shown in figure 2.10 and the thermal calculation is detailed in paragraph 2.3.5.1. Figure 3.5 is an example of the dimensionless temperature distribution generated on the liner surface when assuming that the width of the starved zone is $s=4.4mm$, the nominal surface temperature is $T_0=90^\circ C$ and the obtained temperature increase compared

to T_0 is equal to the one chosen in the first step ($\Delta T = 20K$). Note that the temperature increase is $\Delta T = (1.055 - 1)(T_0 + 273)$.

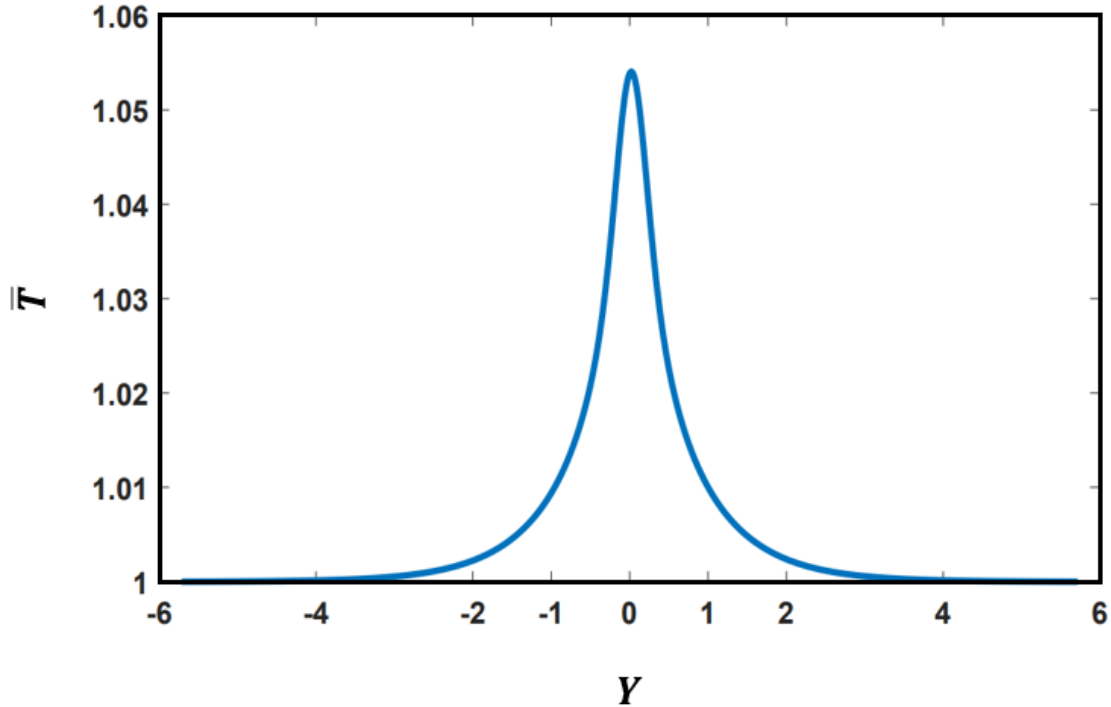


Figure 3.5: Dimensionless temperature distribution generated on the liner surface

As shown in the figure, the highest value of the temperature is located in the middle of the contact and the temperature gradient extends from $Y=-1$ to $Y=1$, this is the starved/heated zone.

As a consequence of the temperature gradient, a lubricant surface tension gradient is generated as shown in figure 3.6.

The increase in temperature leads to a decrease in the lubricant surface tension (equation 2.22), so the surface tension has its lowest value in the heated zone.

In addition, the temperature gradient leads to a lubricant viscosity gradient as shown in figure 3.7, and the increase in the temperature decreases the lubricant viscosity (equation 2.23).

3.3.1.2 Numerical oil flow as a function of the temperature gradient

Starting with the hypothesis that an increase in the temperature occurs in the contact due to a localized lack of lubricant, the temperature, surface tension and viscosity distributions are defined and a Marangoni calculation is carried out. The Marangoni equation calculation is detailed in paragraph 2.3.5.3. Figure 3.8 shows the lubricant film thickness variation in the circumferential direction caused by the Marangoni effect for different

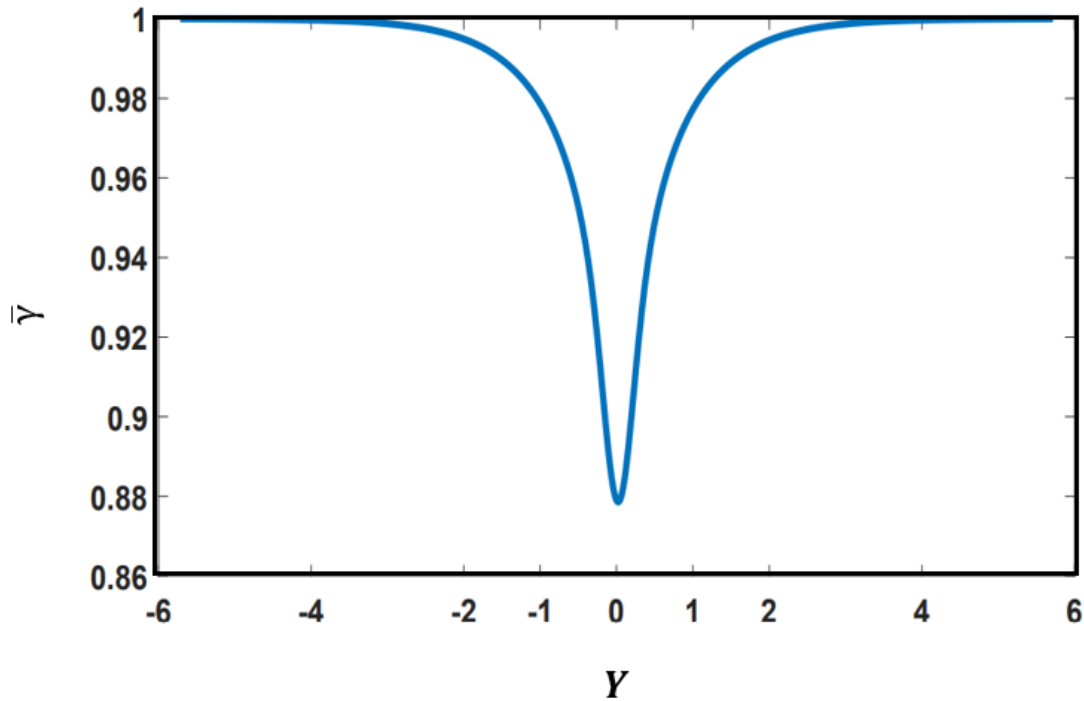


Figure 3.6: Dimensionless lubricant surface tension distribution

temperature increase cases. One can conclude that the maximum lubricant thickness variation is located in the heated zone. This is caused by the decrease in the lubricant surface tension. In fact, the lubricant tends to flow from the warmer zone (where the surface tension is at its lowest value) to the colder zone (where the surface tension is at its highest value). Note that the displacement caused by the Marangoni effect is continuous and lasts for a period of a passage ($t_{passage}$) which depends on the engine round per minute (N). Furthermore, the film thickness decrease is proportional to the temperature increase, and more precisely to the temperature gradient since the source width is kept constant in these examples ($s=4.4mm$). The surface difference (ΔS) between the initial oil distribution for $\Delta T = 0$ and the one corresponding to $\Delta T \neq 0$ represents the oil flux displaced as a result of the Marangoni effect and it is called $S_{Marangoni}$. To quantify the oil flow, the surface difference is calculated as a function of the model parameters.

Due to the Marangoni effect the temperature gradient leads to an oil displacement from the warmer zones to the colder ones which can cause a local lubricant starvation. The latter can be an explanation for the sudden wear appearance presented in figure 2.3.

3.3.1.3 Analytic oil flow

In order to quantify the displacement caused by the Marangoni effect, the differential equation 2.28 is analytically developed so the surface moved ($S_{Marangoni}$) can be obtained by equation 3.6.

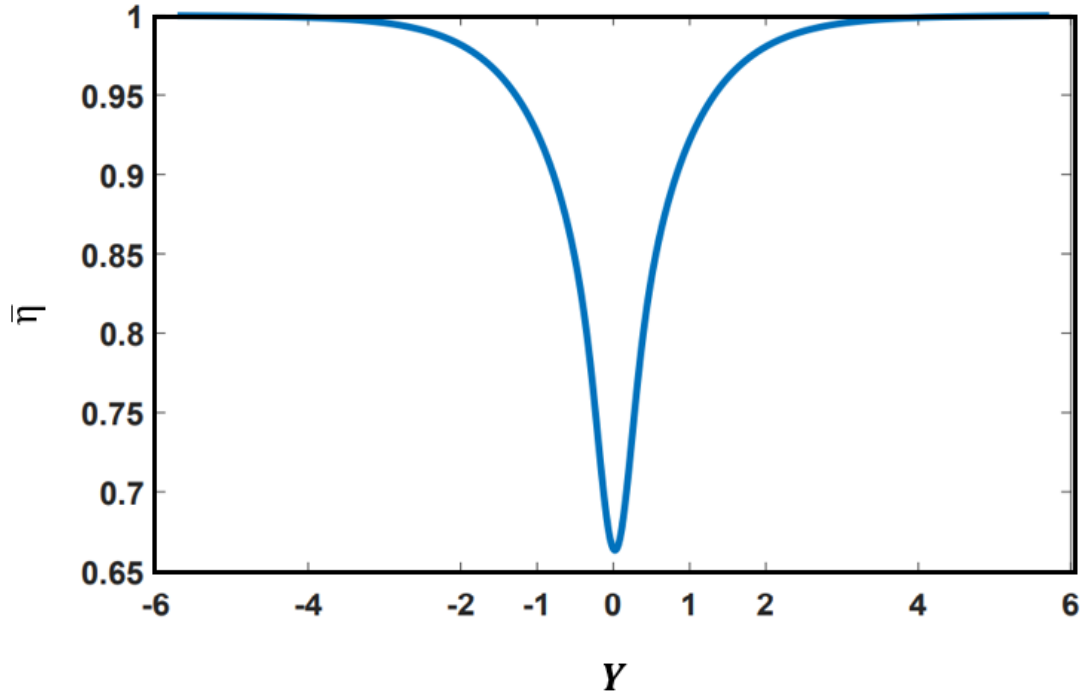


Figure 3.7: Dimensionless lubricant viscosity distribution

$$S_{Marangoni} = s \frac{h_0^2}{2} \left(\frac{\partial(1/\eta)}{\partial y} \frac{\partial \gamma}{\partial y} + \frac{1}{\eta} \frac{\partial^2 \gamma}{\partial y^2} \right) t_{passage} \quad (3.6)$$

The equation development is detailed below:

$$S_{Marangoni} = \Delta S = s \Delta h \quad (3.7)$$

The expression of Δh is obtained from equation 3.6:

$$\Delta h = \frac{h^2}{2} \left[\frac{\partial \left(\frac{1}{\eta} \right)}{\partial y} \frac{\partial \gamma}{\partial y} + \frac{1}{\eta} \frac{\partial^2 \gamma}{\partial y^2} \right] t_{passage} \quad (3.8)$$

Δh in equation 3.7 is replaced by equation 3.8 then equation 3.6 is obtained.

As the equation shows, the displacement depends on the minimum oil film thickness, the local temperature, the temperature increase, the surface tension and viscosity gradients and the time of passage.

3.3.1.4 The influence of the engine speed

The influence of the engine speed on the surface moved due to the Marangoni effect is studied. The temperature increase is $20K$, the width of the heated zone is $s = 4.4mm$ and

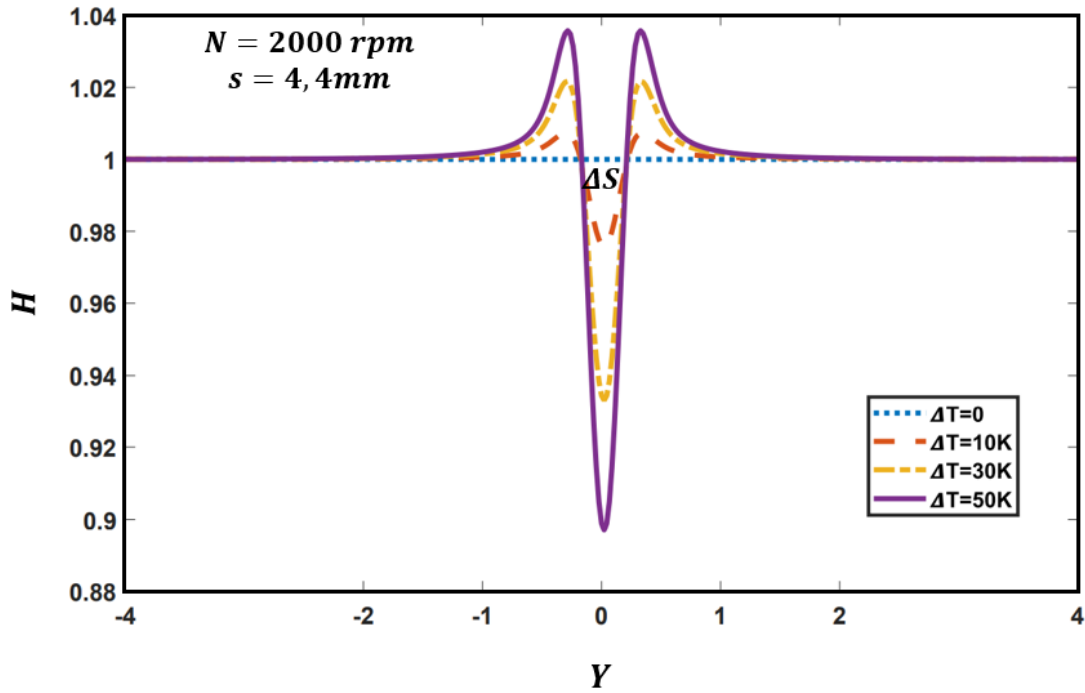


Figure 3.8: Dimensionless film thickness variation along the circumferential direction for different temperature increase values

the oil supply regime is moderately starved. Note that if h_{ff} is the oil film thickness in a fully flooded supply regime, the oil film thickness in a moderately starved regime is $h_{ff}/3$.

The increase in engine speed leads to:

- an increase in the mean velocity (u_m), hence an increase in the minimum oil film thickness (h_0) (equations 3.4, 2.42 and 2.43),
- a decrease in the passage time ($t_{passage}$) (equation 3.5).

As shown in equation 3.6, the Marangoni effect depends on the oil quantity and on the time of passage. For an imposed temperature increase, it is more pronounced when the oil quantity and/or the passage time increases.

Figure 3.9 shows that $S_{Marangoni}$ increases with the engine speed. This result indicates that the sensibility of the oil quantity on the surface moved is more important than that of the time passage.

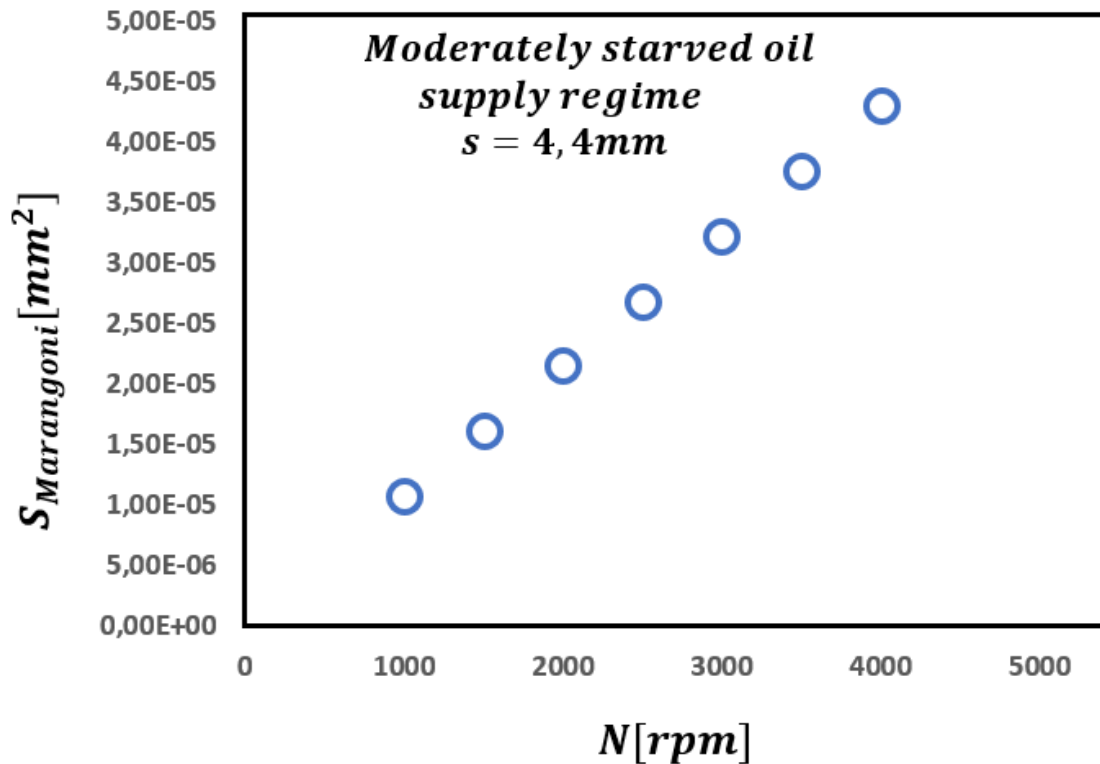


Figure 3.9: The surface moved due to the Marangoni effect as a function of the engine speed (N)

3.3.2 Ring passage effect

3.3.2.1 Lubricant redistribution

In order to study the influence of the ring passage on the oil distribution, a lubricant geometry distribution is imposed at the inlet of the contact. Figure 3.10 is an example of an oil geometry distribution before the ring passage along the liner. The contact occurs between the liner and a parabolic ring. The oil geometry distribution imposed at the inlet of the contact is shown in figure 3.14 as the continuous-blue curve.

Using a mass-conserving solver, the pressure and oil distributions after the ring passage are obtained, see Biboulet et al. [109]. The pressure distribution obtained after the first passage of the ring is shown in figure 3.11. It is divided into two zones: the pressurized and the non-pressurized zones.

- the pressurized zones are obtained where the oil quantity available is sufficient to generate pressure (the white zones on figure 3.12),
- the non-pressurized zones are obtained where the pressure can not be generated as the lack of lubricant is important. They are called the cavitated zones (the grey zones on figure 3.12).

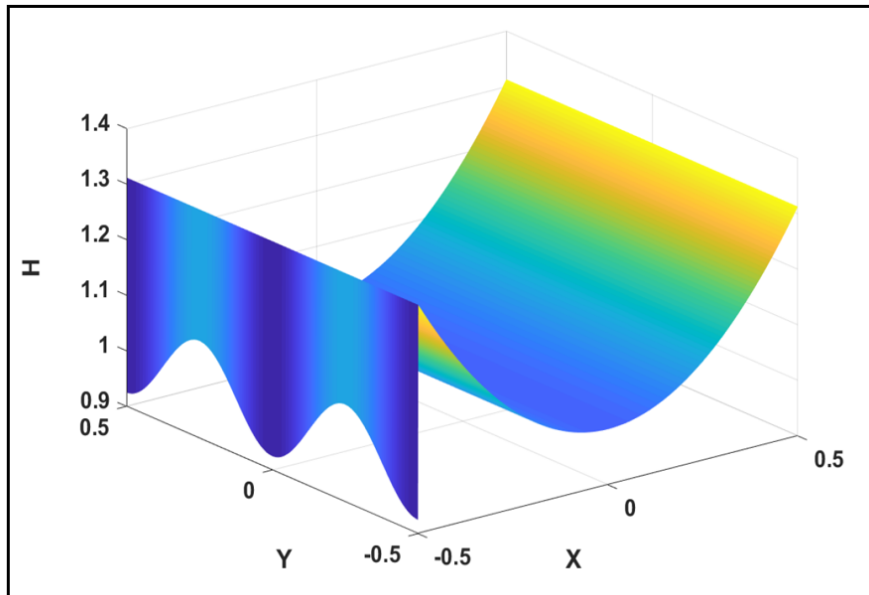


Figure 3.10: Lubricant geometry distribution before the ring passage along the liner

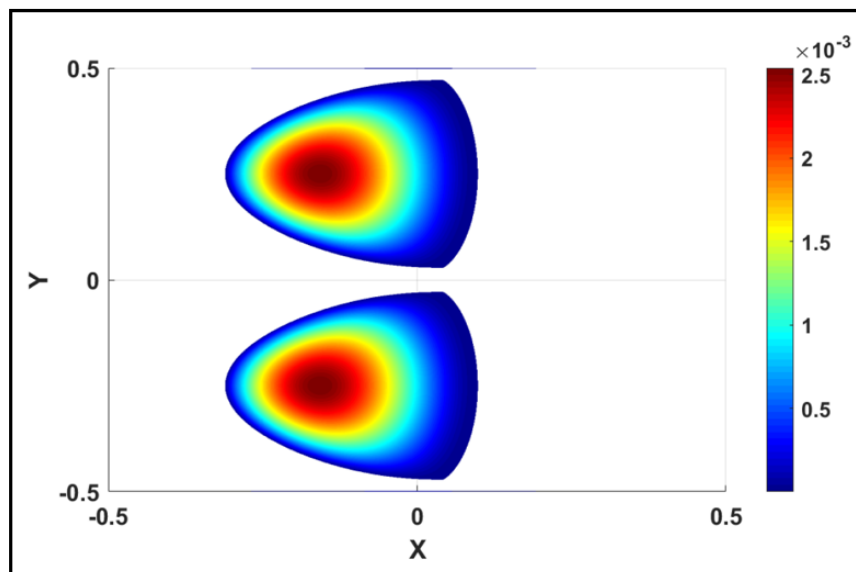


Figure 3.11: Pressure distribution in the contact after one passage of the ring along the liner

Figure 3.13, compares the pressure distributions after the first and the tenth passage of the ring along the liner. After the tenth passage, the pressurized zones are almost touching and the cavitated zone in the middle is avoided. This result indicates that the ring passage along the liner redistributes the lubricant and helps to avoid the lack of lubricant. The ring

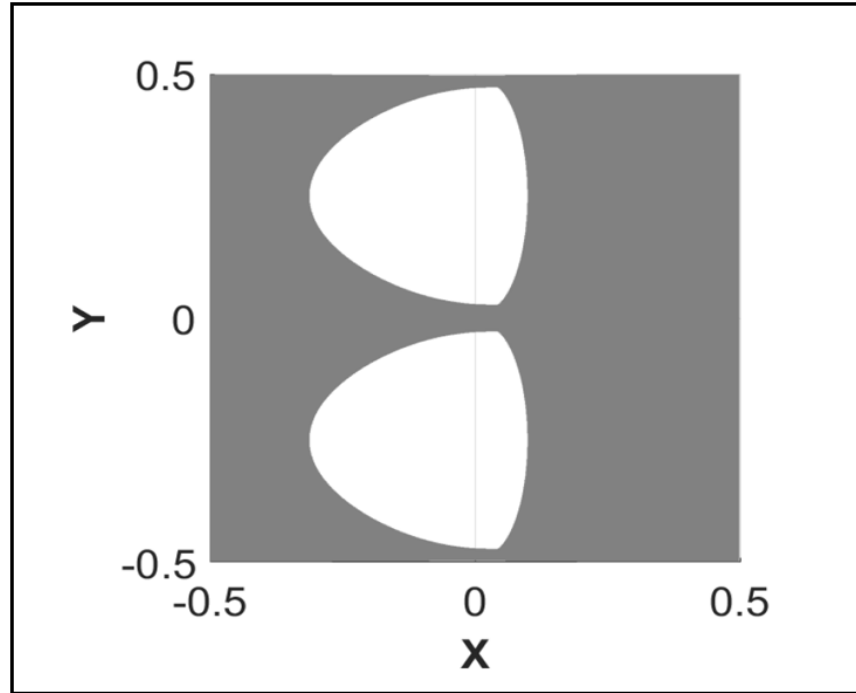


Figure 3.12: Cavitated zones after one passage of the ring along the liner

passage is beneficial for the lubricant distribution hence for the contact performance. The study of the several ring passages was carried out to validate the lubricant redistribution occurring between the ring passages. Since the lubricant distribution occurring between two ring passages is the interest of the following study, the number of passages is limited to 1.

3.3.2.2 Oil redistribution prediction

Figure 3.14 presents the imposed lubricant geometry (see equation 2.2) before the ring passage (continuous-blue curve) and the one obtained after the ring passage (dotdash-purple curve). The lubricant redistributed as a result of the ring passage is quantified as the surface difference between the two curves ($S_{redistributed} = \Delta S_1 + \Delta S_2$). The parameters of the imposed geometry in this example are:

- $H_{mean} = 1$,
- $H_{var} = 0.075$,
- $\Lambda = 0.5$.

The oil redistribution ($S_{redistributed}$) caused by the ring passage along the liner is studied as a function of the minimum oil film thickness (h_0), the wavelength of the initial oil

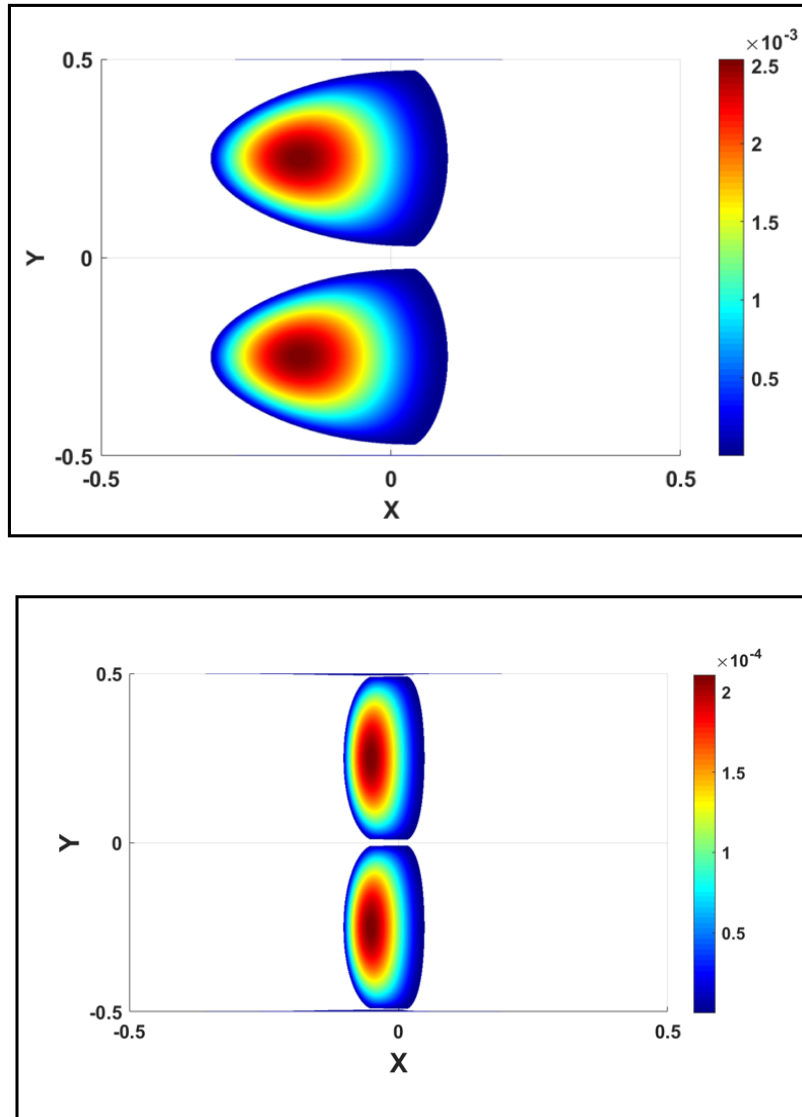


Figure 3.13: Comparison of the pressure distribution after the first and the tenth passage of the ring along the liner

geometry distribution (λ) and the number of passages ($passage$).

The numerical results have then been fitted in order to predict the redistribution as a function of the problem parameters.

The obtained curve fit equation is:

$$S_{redistributed} = \xi (h_{mean} - h_0 + h_{var})^{1.125} \left(\frac{\lambda}{passage^2} \right)^{0.875} \quad (3.9)$$

where ξ is a constant, it is the curve fit parameter.

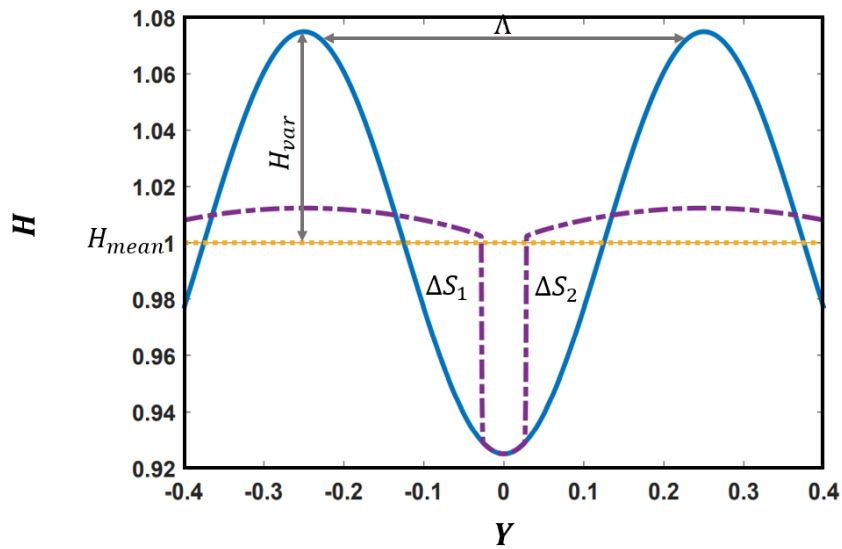


Figure 3.14: Lubricant distributions before and after the ring passage

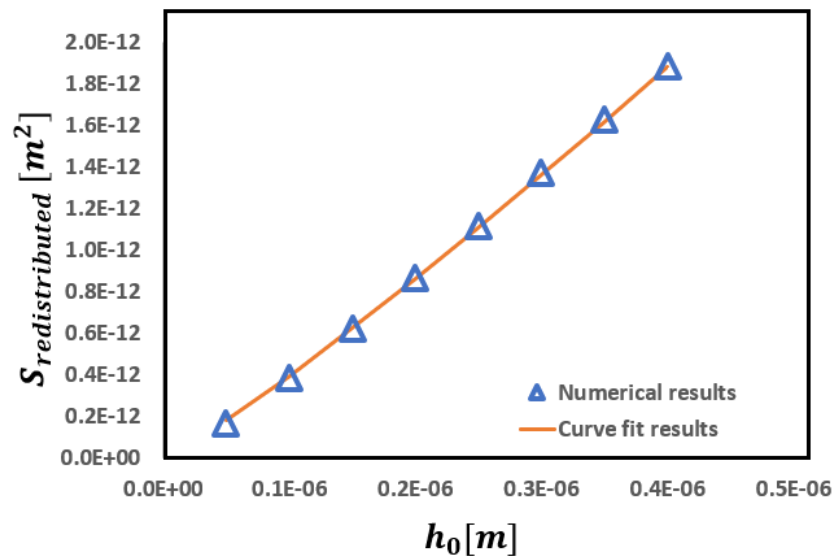


Figure 3.15: Numerical results and curve-fit surface redistributed as a function of h_0

Influence of the minimum oil film thickness: Figure 3.15 shows that the redistribution increases with the oil film thickness. The redistribution depends on the oil quantity supplied to the contact, it is more important when the oil supply is more pronounced. In fact, the redistribution is a result of the pressure gradient generated by the lubricant. When the oil quantity is more important, the pressure gradient generated is also more important and the redistribution is more effective.

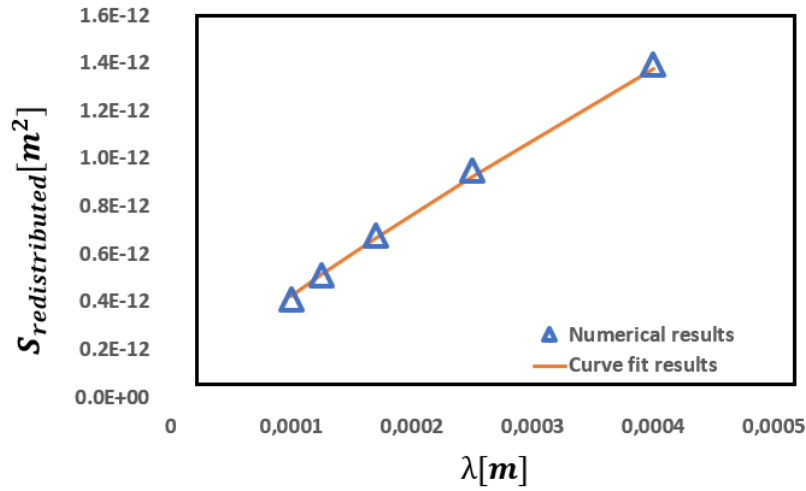


Figure 3.16: Numerical results and curve-fit surface redistributed as a function of λ

Influence of the wavelength: The wavelength of the oil distribution geometry impacts the lubricant redistribution. Results show that the latter increases with the wavelength. When the wavelength increases, the number of cavitated zones decreases as well as the degree of non-uniformity of the oil distribution, which enhances the oil redistribution.

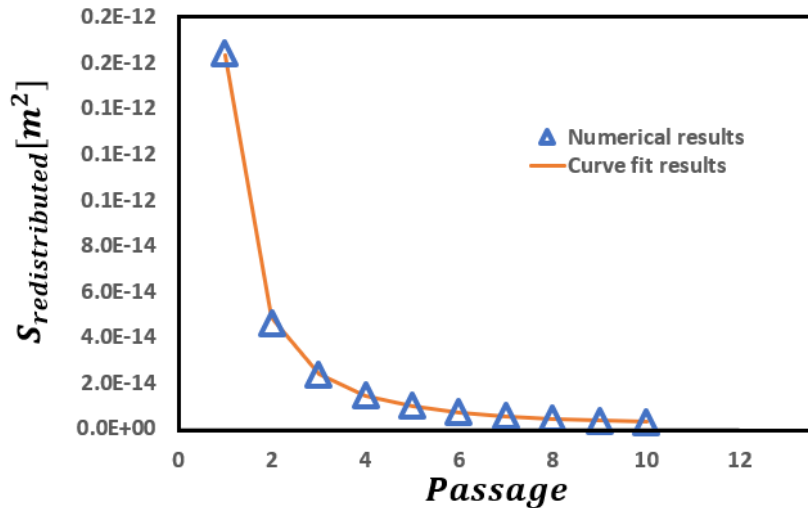


Figure 3.17: Numerical results and curve-fit surface redistributed as a function of the number of passages

Influence of the number of passages: The redistribution is a repetitive process that takes place at each passage of the ring along the liner. Figure 3.17 shows that the re-

distribution slows down with the number of passages or with time since the oil quantity available in the non cavitated zones decreases after each passage. Note that as the lubricant distribution occurring between two passages is the interest of this study, the number of passages is limited to 1.

3.3.3 Interpretation

Once again, the Marangoni effect has an important influence on the oil distribution in the contact. The temperature gradient generated on the surface as a result of a local lack of lubricant and starvation impacts the lubricant surface tension and viscosity. The increase in the temperature leads to a decrease in the lubricant surface tension and viscosity. As a result, the lubricant flows from the warmer zone where the surface tension is low to the colder zone where the surface tension is high leading to a temporarily local lack of lubricant. Results show that the lubricant flows from the middle of the contact where the high temperature is located to the edges. The oil displacement due to the Marangoni effect is quantified as a moving surface ($S_{Marangoni}$) which depends on several parameters. It increases with the temperature increase, the oil quantity and the engine speed.

The ring passage along the liner is another phenomenon that impacts the lubricant distribution in the contact. Results have shown that the passage of the ring redistributes the oil in the contact. The oil flows from the non cavitated zones where the oil quantity available is sufficient for lubrication and for pressure generation to the cavitated ones where there is a lack of oil for lubrication. This effect avoids the local lack of lubricant hence enhances the lubrication conditions and the overall performance of the contact. The redistribution is quantified as a moving surface ($S_{redistributed}$). The redistribution is more effective when the oil quantity and/or the wavelength of the oil distribution geometry increases, whilst it slows down with the number of passages or with time.

3.4 Scuffing initiation limit

The algorithm presented in paragraph 3.2.1 is applied to quantify the oil displaced due to the Marangoni effect ($S_{Marangoni}$) and the oil redistributed due to the ring displacement effect ($S_{redistributed}$) as a function of the operating parameters. Then, the moving surfaces are compared in order to study the scuffing initiation limit. When the moving surfaces are balanced, the lack of lubricant is prevented hence the starvation is limited and scuffing is avoided. This is called the safe zone, the contact operates under normal conditions. Whilst, when the Marangoni effect predominates the ring passage effect, which means that the oil flow is higher than the oil redistributed and the starvation is not limited by the redistribution effect, scuffing might initiate and the contact no longer operates in the safe zone. The scuffing initiation can take place more rapidly when the Marangoni effect becomes more and more pronounced compared to the redistribution effect.

The scuffing initiation limit is presented as a curve. The safe zone where scuffing is prevented is located below this curve. Whilst above it, scuffing can occur. The limit is studied as a function of the model parameters such as the contact load ($F_{contact}$), the

engine speed (N) and the thermal parameters as the heated zone width (s) and the local temperature increase (ΔT). This section intends to present the dependency of the scuffing initiation limit as a function of these parameters.

3.4.1 Contact load depends on the ring tension only

In this subsection, the contact load is considered to be composed of the ring tension (F_{ring}) only, without considering the thrust load (F_{thrust}).

3.4.1.1 Influence of the thermal parameters

Figure 3.18 is a chart giving the scuffing initiation limit as a function of the ring tension and the local temperature increase for different widths of the heated zone and a moderately starved oil supply regime.

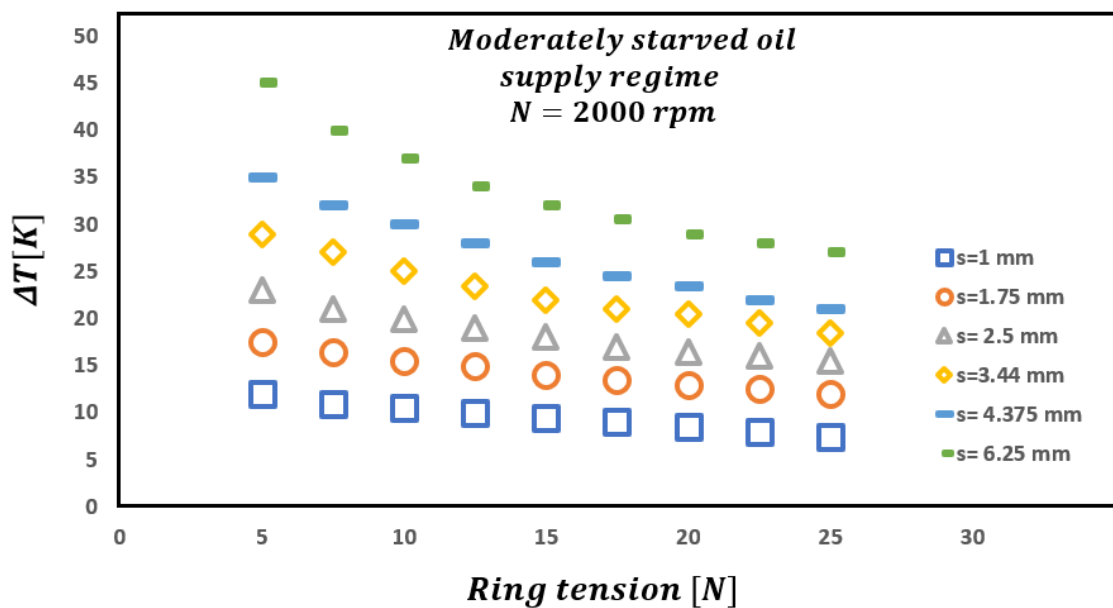


Figure 3.18: Scuffing initiation limit as a function of the ring tension (F_{ring}) and the surface temperature increase (ΔT)

From this chart, two vital conclusions can be drawn:

- for the same ring tension and surface temperature increase, the scuffing initiation limit shifts by increasing the width of the heated zone thus the safe zone becomes wider,
- for the same width of the heated zone and by increasing the ring tension, the required surface temperature increase causing scuffing initiation decreases. This is caused by the increase in the contact load.

The temperature increase is a vital variable impacting the oil flow caused by the Marangoni effect. As the temperature gradient is more and more important, the surface moved by the Marangoni effect increases and scuffing might initiate more rapidly.

3.4.1.2 Influence of the engine speed

Figure 3.19 presents the scuffing initiation limit for different engine speeds. It shows that the scuffing initiation limit is shifted when the engine speed increases. In fact, the surface displaced due to the Marangoni effect increases with the engine speed due to the increase in the minimum oil film thickness as shown previously in figure 3.9. Moreover, the surface redistributed due to the ring displacement effect increases also with the oil film thickness which increases with the engine speed as shown in figure 3.15. The balance between the moving surfaces seems to be more pronounced when the engine speed increases thus scuffing initiation is delayed.

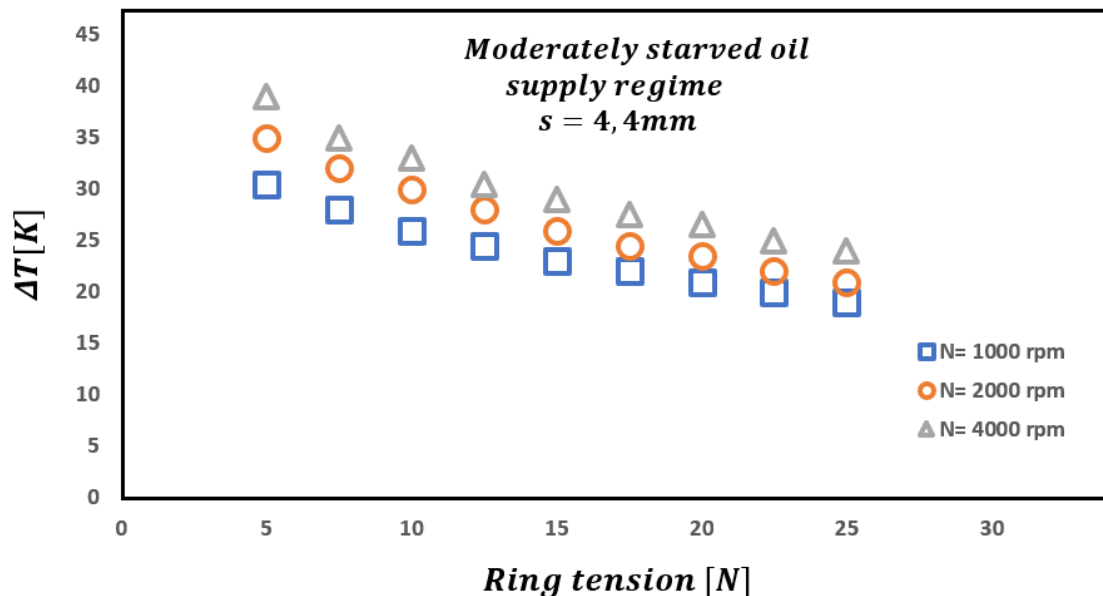


Figure 3.19: Scuffing initiation limit as a function of the ring tension and the surface temperature increase for different engine speeds

3.4.2 Composed contact load

In this subsection, the thrust load described in paragraph 3.2.2.2 is taken into consideration as an additional load to the ring tension in order to study its impact on the scuffing initiation limit. Figure 3.20 is an example of the thrust load distribution given for an engine cycle for a frequency in rpm is $N = 2000$ rpm.

The averaged thrust loads of the engine strokes are given below:

- $F_{explosion} = -2267$ N,

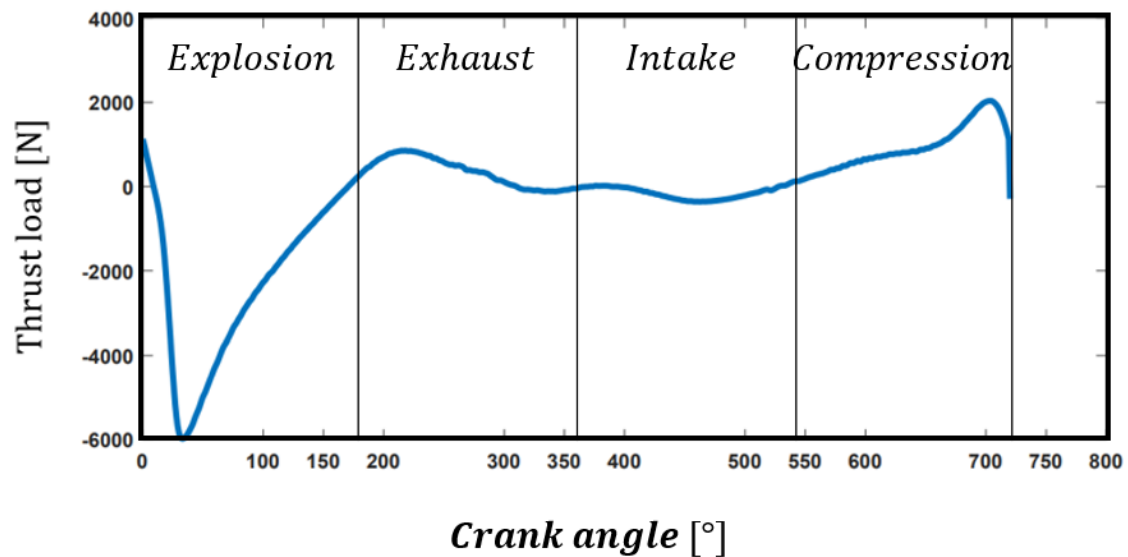


Figure 3.20: Thrust load distribution for an engine cycle

- $F_{exhaust}=350$ N,
- $F_{intake}=-150$ N
- $F_{compression}= 902$ N.

The highest thrust load is obtained during the power stroke phase because of the high pressure in the combustion chamber. The averaged thrust load over an engine cycle is $F_{thrust}=\frac{\sum F}{4}$.

3.4.2.1 Influence of the averaged thrust load

The comparison between the scuffing initiation limit with and without considering the thrust load is shown in figure 3.21. When the thrust load is considered, the contact load increases hence the contact condition becomes more critical and scuffing might initiate more rapidly in this case. In fact, the minimum oil film thickness depends on the liner load (w_1) as given in equation 2.42 and equation 2.43. The higher the liner load, the lower the minimum oil film thickness. Note that $w_1=p_{contact} t_{axial}$ where $p_{contact}$ is given in equation 3.3.

3.4.3 Interpretation

The scuffing initiation limit depends upon two opposing effects, the Marangoni and the ring displacement effects.

The temperature gradient generated in the contact as a result of the lack of lubricant leads to the Marangoni effect which in turn increases the starvation level in the contact.

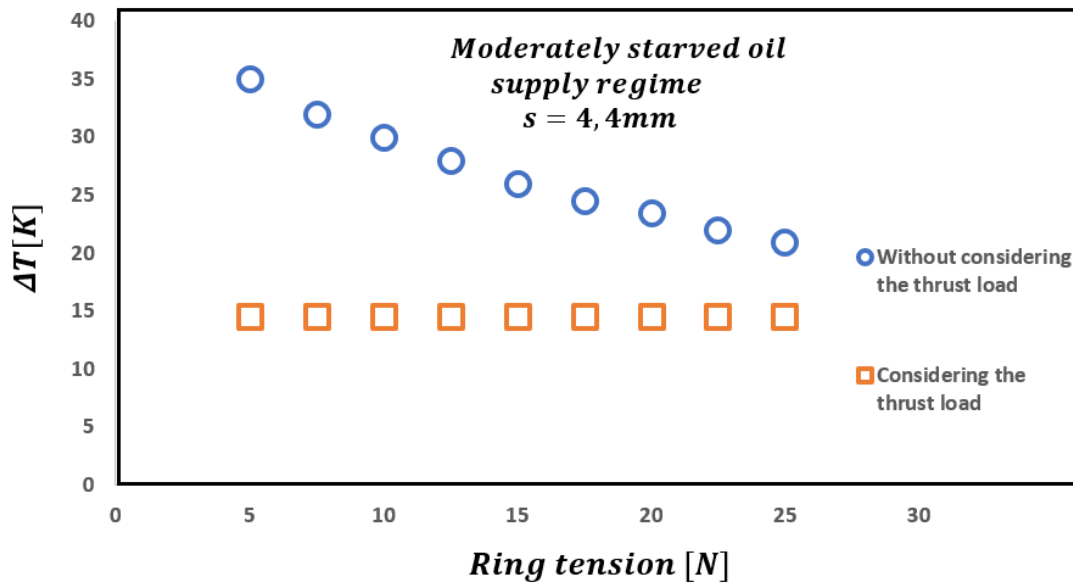


Figure 3.21: The scuffing initiation limit as a function of the ring tension and the temperature increase without and with the thrust load

On the other side, the passage of the ring along the liner redistributes the lubricant which helps to avoid starvation.

The scuffing initiation limit has been studied as a function of the model parameters such as the engine speed, ring tension, thrust load, oil supply regime and the thermal parameters as the width of the heated zone and the temperature increase compared to the surface initial temperature.

The main conclusions from this study are:

- for the same temperature increase and contact load, the scuffing initiation limit is shifted when the width of the heated zone increases,
- when the ring tension decreases, the safe zone becomes wider as the contact load decreases,
- when the engine speed increases the scuffing initiation limit is shifted and the safe zone becomes wider,
- when considering the thrust load, the contact load increases and scuffing might initiate sooner compared to the case where only the ring tension is taken into consideration,

3.5 Conclusion

The influence of two effects on the lubricant distribution and the scuffing initiation limit is studied in this chapter:

- the Marangoni effect, which tends to create a local lack of lubricant due to the temperature gradient generated on the surface. The lubricant tends to flow from the high-temperature zones to the low- temperature zones because of the lubricant surface tension gradient. This displacement generates a local lack of lubricant and increases the severity of starvation. This lubrication condition might accelerate the scuffing initiation,
- the ring passage along the liner, which contributes to redistribute the oil in the contact. This redistribution helps to avoid starvation and shifts the scuffing initiation limit.

When the contact is exposed to heating, its lubrication conditions are affected and temporarily starvation can occur. After re-lubricating the contact, one of the following cases will happen:

- if the starvation is balanced with the re-lubrication, the heating is avoided and the contact will perform normally as it operates in the safe zone,
- if the heating is important to the level where the starvation is not avoided by the re-lubrication hence the contact no longer operates in the safe zone and risk of scuffing initiation exists.

Chapter 4

Scuffing initiation caused by surface heating in the piston ring cylinder liner

Contents

4.1	Introduction	68
4.2	Model presentation	68
4.2.1	Thermo-mechanical loop	68
4.2.2	Prediction of the additional load	69
4.2.3	Thermo-mechanical effect: temperature increase	72
4.3	Scuffing initiation limit	73
4.3.1	Lubricant additive desorption	73
4.3.2	Thermo-mechanical effect outcomes	75
4.3.3	Scuffing initiation limit	78
4.4	Coupled effects	80
4.4.1	Complete model	80
4.4.2	Coupled effects: scuffing initiation limit	80
4.5	Conclusion	83

4.1 Introduction

Due to a non-uniform lubricant distribution in the PRCL contact, local starvation can temporarily occur, which increases the coefficient of friction. An additional local heat flux is then generated, leading to a temperature increase in the contact. As a result, a surface deformation occurs due to the thermo-mechanical effect. The latter initiates a loop that can have two aspects. These aspects and their effect on scuffing initiation are studied in this chapter. Moreover, the thermo-mechanical effect is coupled with the effects studied in the previous chapter (the Marangoni and the oil redistribution effects) in order to study their contribution to scuffing initiation. The first section presents the loop caused by the thermo-mechanical effect and the second section presents the effect of the loop on scuffing initiation. The contribution of the coupled effects to scuffing initiation is presented in the third section. Finally, the conclusions obtained in this chapter are presented.

4.2 Model presentation

4.2.1 Thermo-mechanical loop

The algorithm of the thermo-mechanical loop shown in figure 4.1 is detailed below. Assuming that due to a temporarily local lack of lubricant in the contact, the coefficient of friction increases and an additional heat flux is generated in the contact that causes an increase in the contact temperature. As a first step, the temperature increase (ΔT) compared to the nominal temperature (T_0) occurring in the contact is chosen as an input for the model. The latter leads to a ring deformation as a result of the thermo-mechanical effect. The occurrence of the ring deformation generates stress and an additional load is considered to the contact, which is equal to the one needed to return the ring surface to its nominal position. The contact load is expressed as a pressure ($p_{contact} = p_{contact} + p_{additional}$). Note that as the generated stress is proportional to the rate of deformation (equation 2.21) and the rate of deformation is proportional to the temperature variation (equation 2.20), thus the additional load is proportional to the temperature increase. The next step calculates the oil film thickness (h_0) using equation 2.42 or equation 2.43 depending on the oil supply regime detailed in paragraph 2.2.4. Then, the coefficient of friction (μ) is obtained by the Stribeck curve depending on the oil film thickness and the surface roughness. Note that the surface roughness (σ) is constant in the model. As shown in the Stribeck curve (figure 2.13), the lower the oil film thickness, the higher the coefficient of friction. The obtained coefficient of friction combined with the contact pressure and the ring velocity generates again a heat flux that leads to a temperature variation and a loop is initiated.

The thermo-mechanical loop can have two outcomes:

- if after re-lubricating the contact, the surface temperature decreases, which means that the contact re-operates under normal conditions, then the loop did not influence the contact performance negatively,

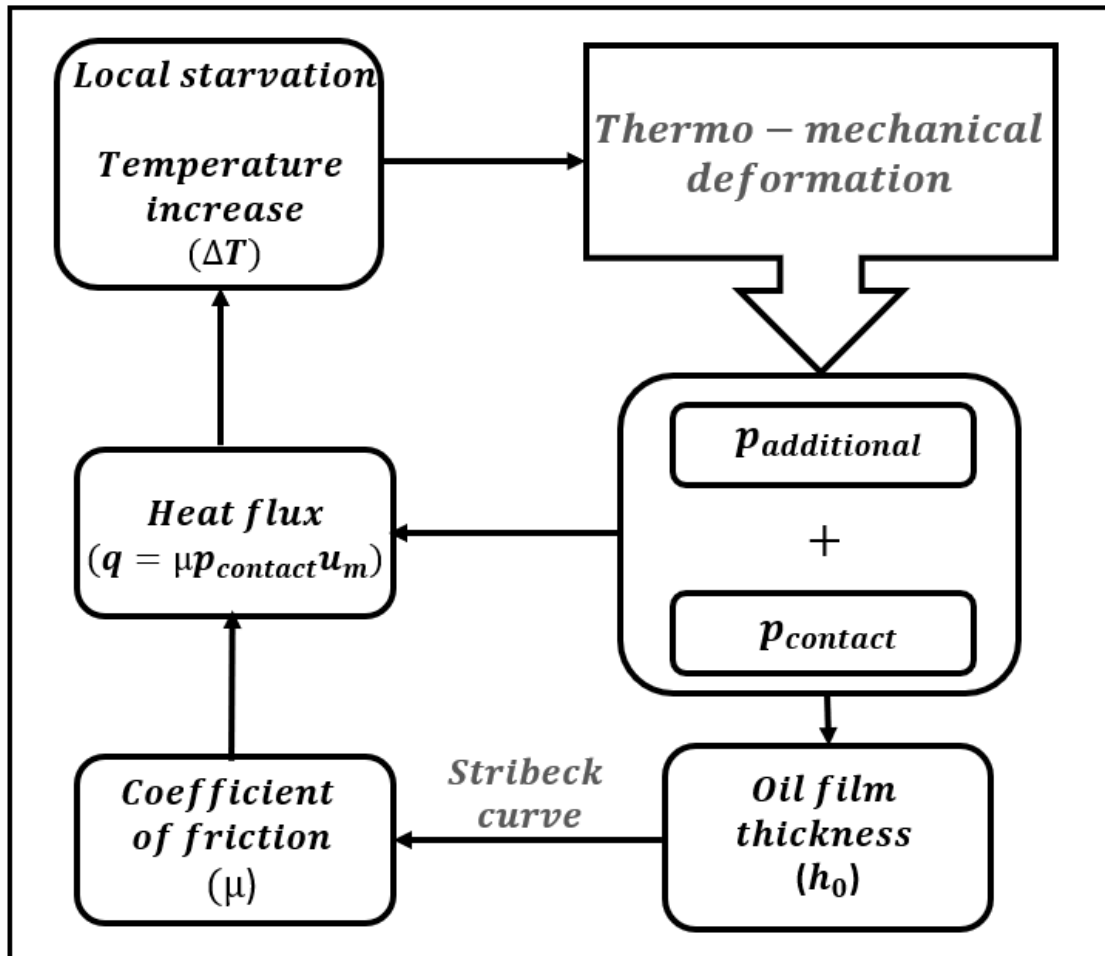


Figure 4.1: Algorithm of the thermo-mechanical loop

- if despite the re-lubricating, the coefficient of friction as well as the temperature increases continuously, a snowball effect takes place, which can lead to a catastrophic increase of the surface temperature and surface failure might occur.

The loop ends when the surface temperature is stabilized to the nominal surface temperature (T_0), which means that the contact re-operates under normal conditions or when the temperature reaches the value of the limit temperature (T_{limit}) when lubricant additive desorption happens and the coefficient of friction increases suddenly. In this case, scuffing might initiate in the contact. Note that T_{limit} depends on the lubricant type and additives.

4.2.2 Prediction of the additional load

As mentioned in the previous section, ring deformation occurs as a response to the temperature variation and an additional load is considered to the contact, which is equal to

the force needed to return the ring to its nominal position. Assuming that the deformation occurring is elastic and linear, the load ($F_{additional}$) depends linearly on the rate of deformation (ϵ). The deformation is calculated for the piston ring surface by considering that the heat is totally transferred to the ring to simulate the worst case. The calculation is carried out using COMSOL Multiphysics software by modeling a ring surface exposed to a temperature increase in the starved zone. The output is the surface deformation distribution and the additional load. The ring geometry parameters and surface modeling are detailed in appendix B. Figure 4.2, is an example of the temperature distribution of the ring surface represented by COMSOL Multiphysics. The width of the starved zone is $s = 4.4mm$ and the temperature increase is $20^\circ C$. The nominal ring temperature is imposed and $T_0=90^\circ C$ (except at the heated zone where a temperature difference takes place). Note that T_0 does not influence the load as the latter depends on the temperature variation regardless of the value of T_0 . The surface deformation occurring due to the temperature variation is then obtained using a plane-stress analysis as the axial ring thickness is about a few millimeters ($t_{axial} = 1.5mm$) [110]. The ring deformation as a response to the temperature variation of figure 4.2 is shown in figure 4.3 as a displacement. Note that the deformation is exaggerated in the figure. The maximum deformation is located where the temperature is the highest, at the hot-spot. The additional load is equal to the required load that prevents the surface deformation at the highest temperature spot (see figure B.6).

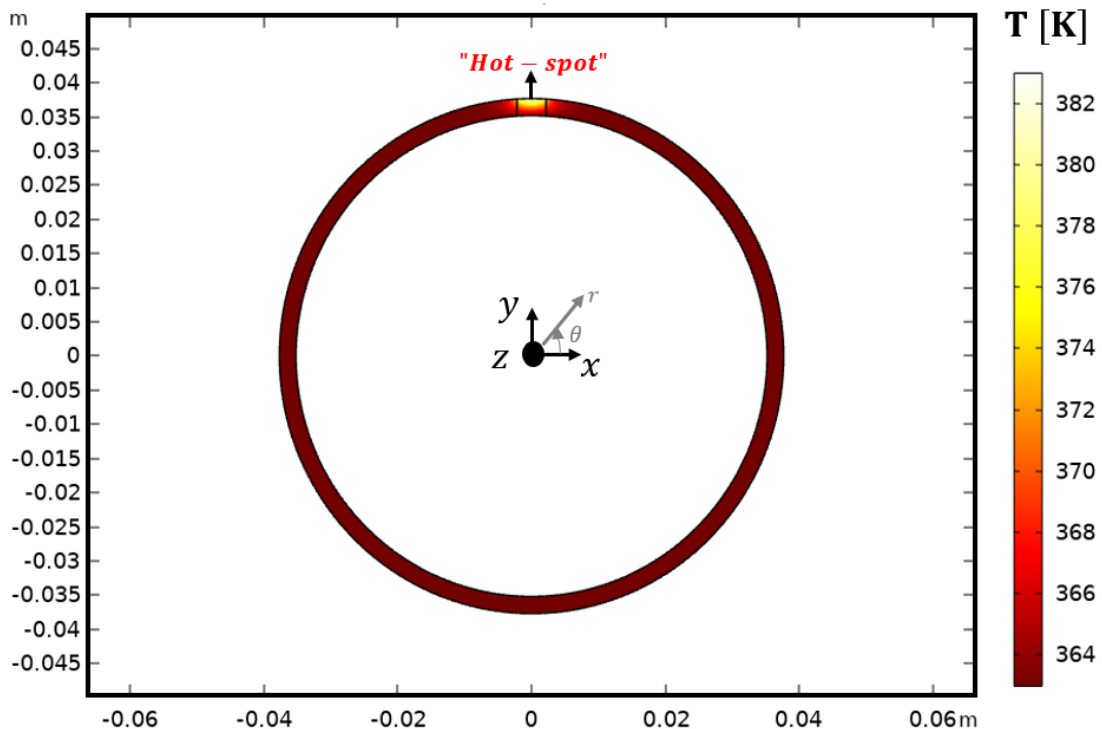


Figure 4.2: Ring surface temperature distribution

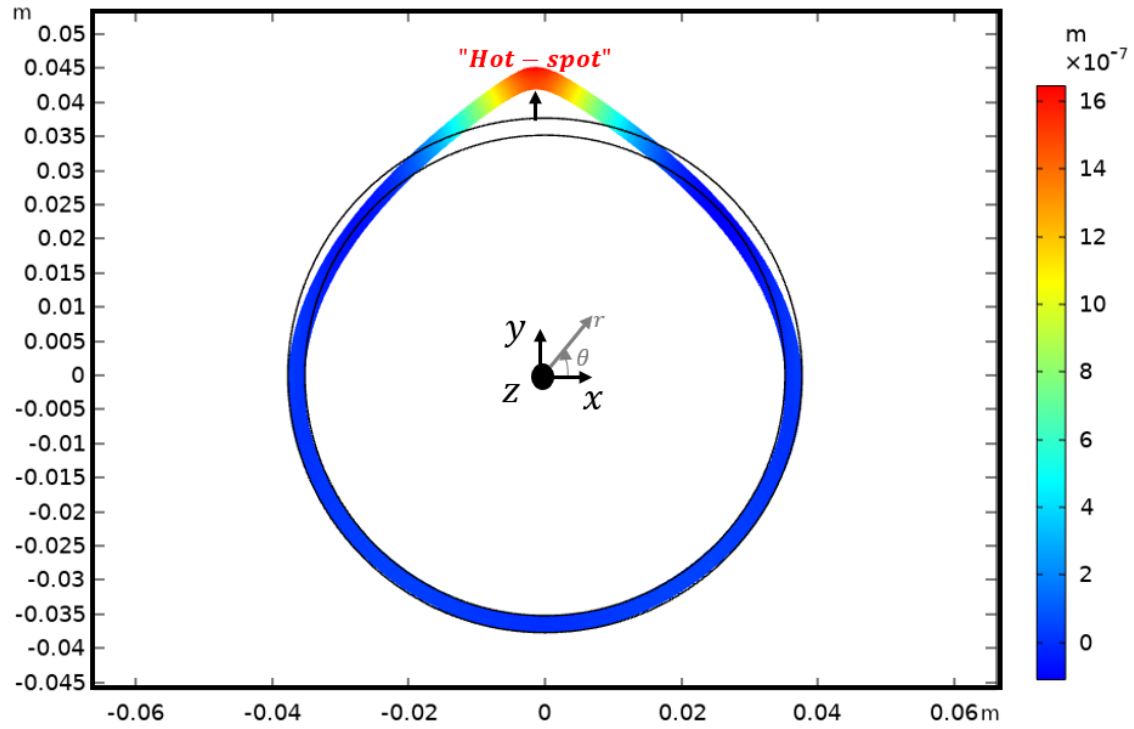


Figure 4.3: Ring surface deformation as a result of the surface temperature distribution shown in figure 4.2

In order to study the influence of the ring geometry on the additional load, the modeling via COMSOL Multiphysics is carried out for different ring diameters (ϕ) where the rings are exposed to the same temperature increase ($\Delta T = 20^\circ\text{C}$) in the heated zone compared to the surface temperature (T_0). The obtained additional load as a function of the ring diameter is shown in figure 4.4. For the same temperature increase, the additional load (equal to the required load that prevents the surface deformation at the hot-spot) decreases when the ring diameter increases. The results are then curve fitted to predict the additional load analytically. The analytic load predicted is given in the equation below:

$$F_{\text{additional}} = \kappa \left(\frac{\phi}{2} + t_{\text{radial}} \right)^{-2} \Delta T \quad (4.1)$$

where κ is the parameter of the curve fit.

Subsequently, the additional pressure is calculated by the equation below.

$$P_{\text{additional}} = \frac{F_{\text{additional}}}{s t_{\text{axial}}} \quad (4.2)$$

where s is the width of the heated zone and t_{axial} is the axial thickness of the ring.

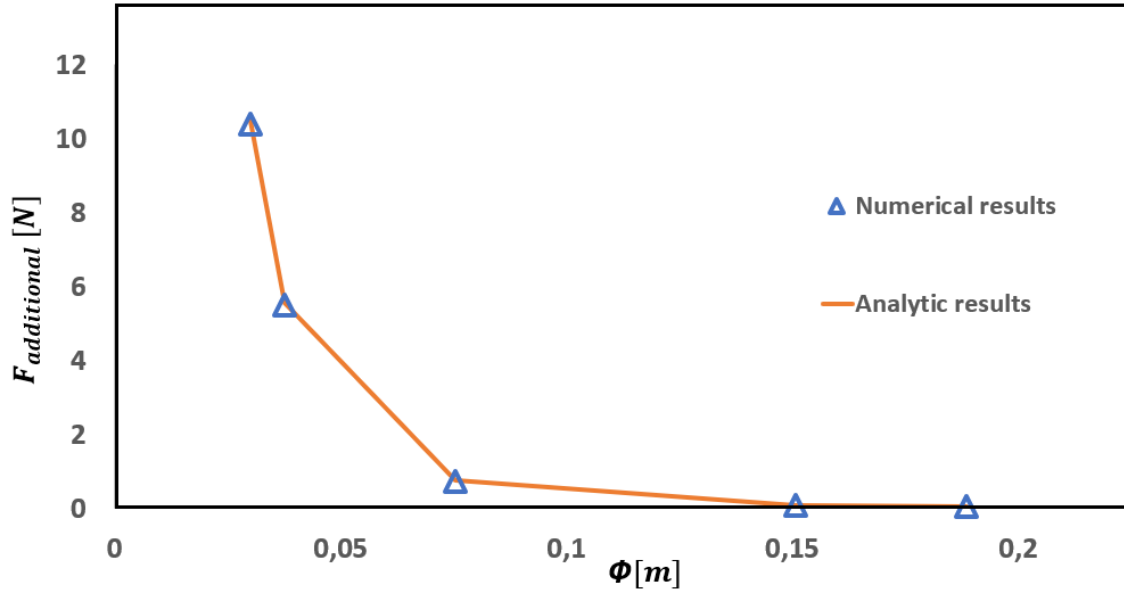


Figure 4.4: Numerical and analytic results of the additional load as a function of the ring diameter

4.2.3 Thermo-mechanical effect: temperature increase

Figure 4.5 is an example of the successive surface temperature increase (ΔT) due to the additional load generated as a result of the ring surface deformation occurring. To better understand the effect of the additional load on the temperature increase, the oil film thickness (h_0) hence the coefficient of friction ($\mu=0.08$) are constants in this example. At every iteration, the additional load is calculated in function of the temperature increase as given in equation 4.1. Due to the additional load, the generated heat flux increases, which leads again to a surface deformation and an additional load. The loop is running until convergence is reached. ΔT_1 is the temperature increase at the first iteration because of the ring tension only ($F_{ring}=7.5$ N), then the temperature increases progressively due to the additional load that generates at every iteration to the converged temperature increase $\Delta T_{converged}$. One can conclude that the converged temperature increase is multiplied by a factor approximately equal to 8 compared to the initial increase due to the ring tension only. The obtained numerical results are curve fitted to get an analytic prediction equation of the temperature increase.

The curve fit equation is:

$$\Delta T_n = \Delta T_1 \left(1 + \zeta_1 \sum_{i=2}^n \exp(-\zeta_2 i) \right) \quad (4.3)$$

where ζ_1 and ζ_2 are constants, ΔT_1 is the temperature increase at the first iteration (caused by the ring tension only), ΔT_n is the temperature increase at iteration n . The temperature increases until convergence occurs.

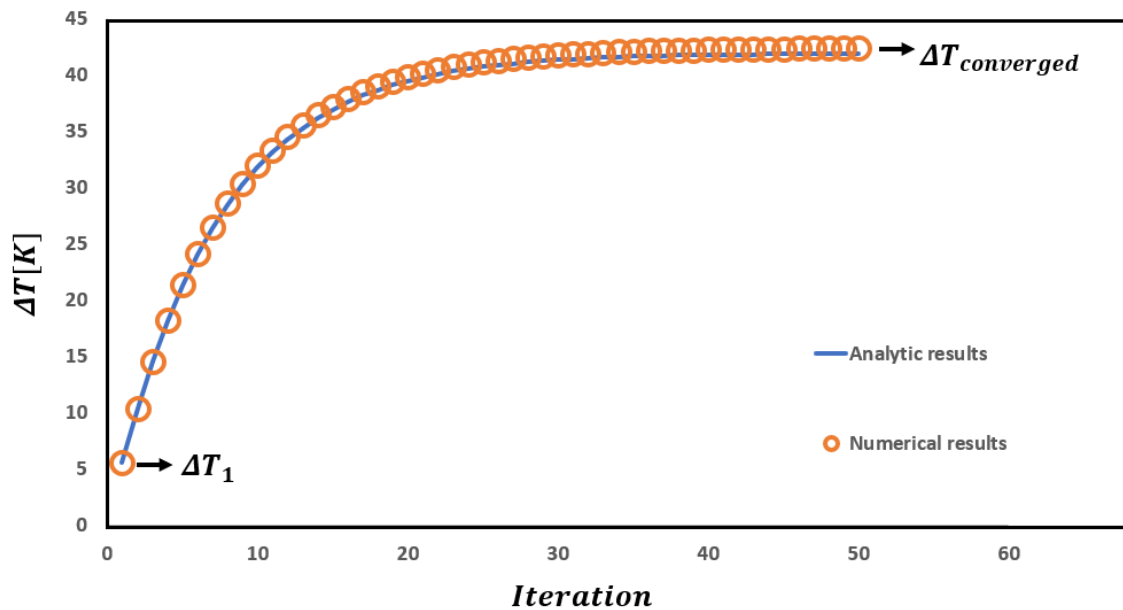


Figure 4.5: Numerical and analytic results of the temperature successive increase

4.3 Scuffing initiation limit

As mentioned in the previous sections, local starvation causes the increase in the coefficient of friction, which generates a surface temperature difference that causes the thermo-mechanical effect. Hence, the latter increases the contact load and impacts the surface temperature. As a result, two scenarios might take place. The first one is that the surface temperature re-stabilizes to the nominal one (T_0) when the contact is re-lubricated, which means that the contact operates in the safe zone where there is no risk of scuffing. The second one is that the surface temperature increases continuously despite re-lubricating the contact. In this case, the temperature might reach the limit temperature and additive desorption occurs. Hence, the role of the additives is lost, thus the coefficient of friction increases suddenly, which can initiate scuffing. The lubricant additive desorption and its effect on scuffing initiation are detailed in this section.

4.3.1 Lubricant additive desorption

The majority of the engine lubricants contain around 15 % of additives [117]. They are chemical products that improve the lubricant properties under different operating conditions and contribute to lower friction and wear in the contact [118] when boundary lubrication regime occurs. However, a lubricant might lose its additive when it degrades. In fact, surface wear can cause lubricant degradation. The metal wear particles act as a catalyst that speeds up lubricant degradation [18].

Another factor causing lubricant degradation is the temperature. When the lubricant is exposed to a temperature higher than its recommended stable one, the lubricant might

decompose and its additive can be removed. This is called the thermal breakdown [18]. An important temperature to be considered is the temperature at the flash point of the lubricant. By definition, the flash point is the minimum temperature at which the vapor of the lubricant is ignited if given an ignition source [119, 120]. The flash point of lubricant is one of the properties given in its technical sheet data. For engine oil, it ranges between 230 and 240°C [121–124].

In this study, the role of the lubricant additive is limited to the range of the limit temperature (T_{limit}) when its desorption initiates. The limit temperature is taken 180°C and the limit coefficient of friction is $\mu_{limit}=0.5$. Based on this analysis, when the temperature is higher than the limit temperature, the coefficient of friction depends not only on the film thickness and the surface roughness but also on the temperature. Figure 4.6 shows the Stribeck curve giving the coefficient of friction as a function of the temperature and the ratio of the film thickness over the surface roughness when the temperature is higher than the limit temperature ($T > T_{limit}$). Starting from $T=180^{\circ}\text{C}$, the lubricant additive desorption initiates and the coefficient of friction increases gradually. At $T=230^{\circ}\text{C}$, the coefficient of friction reaches 1.

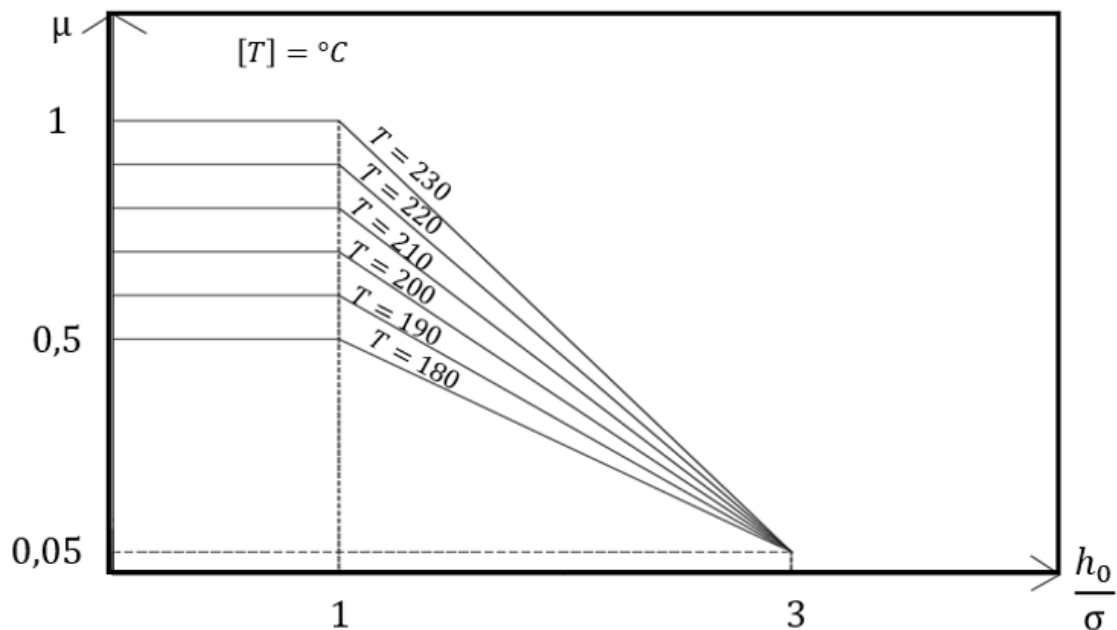


Figure 4.6: Stribeck curve: the coefficient of friction as a function of the temperature and the ratio of the film thickness over the surface roughness when the temperature is higher than the limit temperature

4.3.2 Thermo-mechanical effect outcomes

Assuming that local starvation occurs, the coefficient of friction increases and generates an additional local heat flux, which leads to a local temperature increase (ΔT) compared to T_0 . In the following cases, the width of the starved zone is $s=4.4\text{mm}$ and the nominal surface temperature is $T_0=90^\circ\text{C}$.

The two possible outcomes of the thermo-mechanical effect are a return to the nominal temperature T_0 or a thermal run away leading to failure.

4.3.2.1 The contact re-operates under normal conditions

In this case, the temperature increase is $\Delta T=15^\circ\text{C}$ in the starved zone. The variation of the temperature over the thermo-mechanical loop is given in figure 4.7. The temperature decreases and re-stabilizes to T_0 . Here, the thermo-mechanical effect does not negatively affect the contact performance and the contact re-operates under normal conditions (where the heating is avoided after re-lubricating the contact). As a result, the coefficient of friction also decreases over the loop and reaches its nominal value ($\mu=0.05$) as shown in figure 4.8.

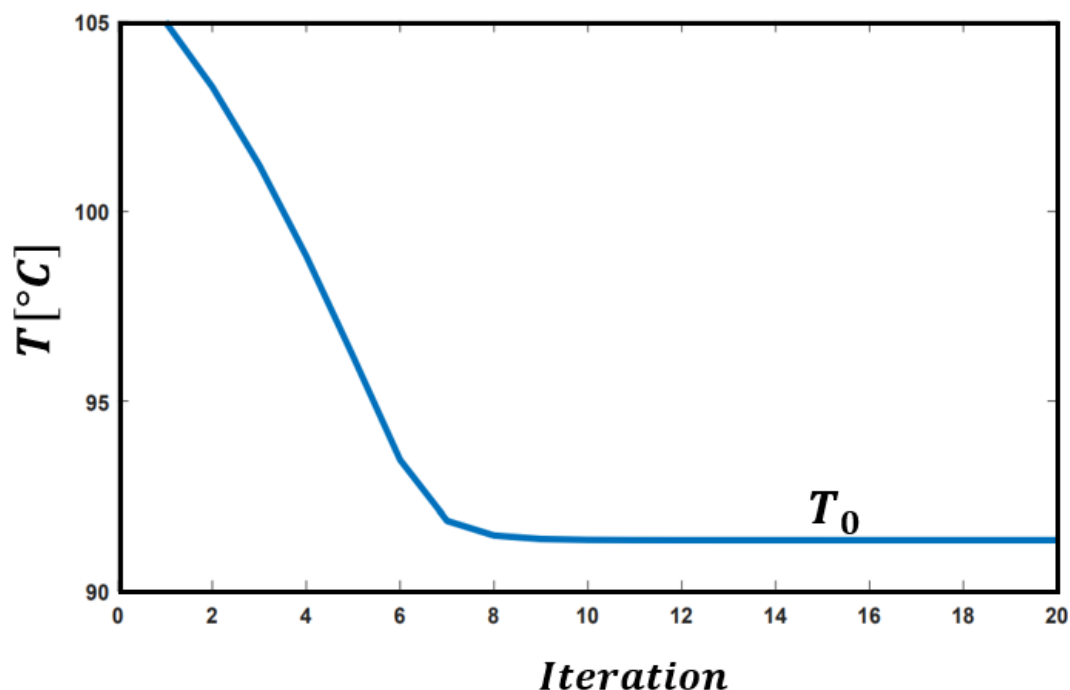


Figure 4.7: Temperature evolution over the thermo-mechanical loop

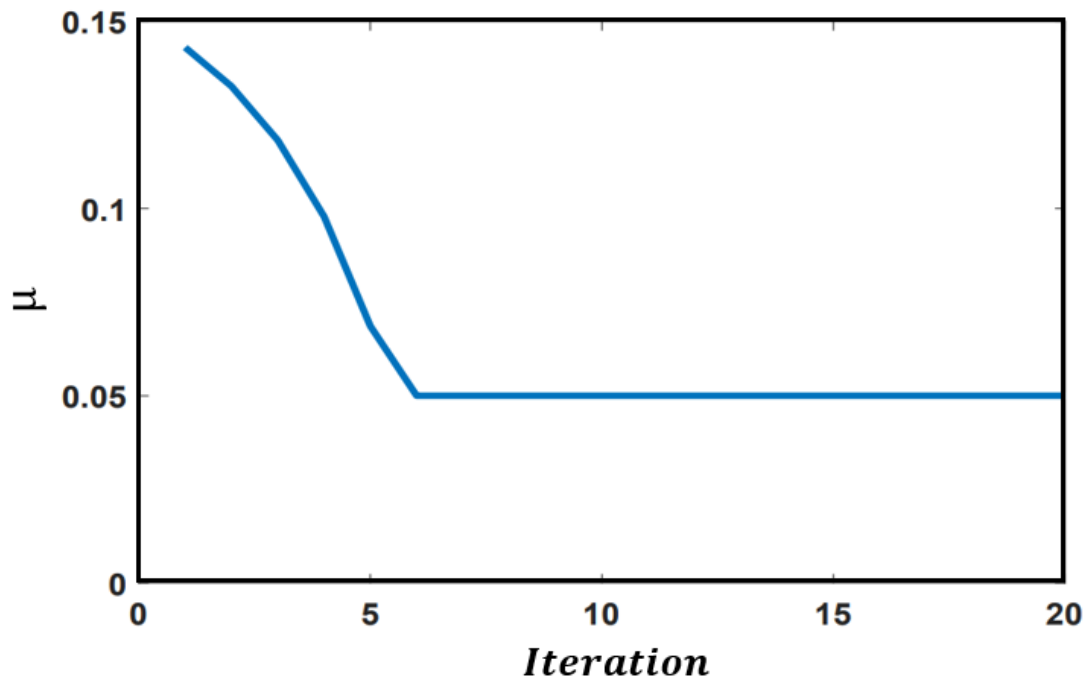


Figure 4.8: Coefficient of friction evolution over the thermo-mechanical loop

4.3.2.2 The contact conditions lead to a thermal run away

In this case, assuming that starvation is more severe than in the first case; hence, the coefficient of friction and the temperature increase are more important than in the previous case. The temperature variation is $\Delta T = 35\text{ }^{\circ}\text{C}$ in this example instead of $\Delta T=15^{\circ}\text{C}$. The temperature and the coefficient of friction evolution over the thermo-mechanical effect are shown in figure 4.9 and figure 4.10. The temperature increases gradually and reaches the limit temperature ($T_{limit}=180^{\circ}\text{C}$). As a result, additive desorption initiates and the coefficient of friction increases more rapidly and reaches its limit. The severe increase of the coefficient of friction indicates the transition from the safe zone where the contact operates under normal conditions to the risk zone where the contact conditions are severe and scuffing might initiate. Here, the thermo-mechanical loop effect causes a snowball effect. Despite re-lubricating the contact, the heating is not avoided; hence, the temperature and the coefficient of friction increase continually.

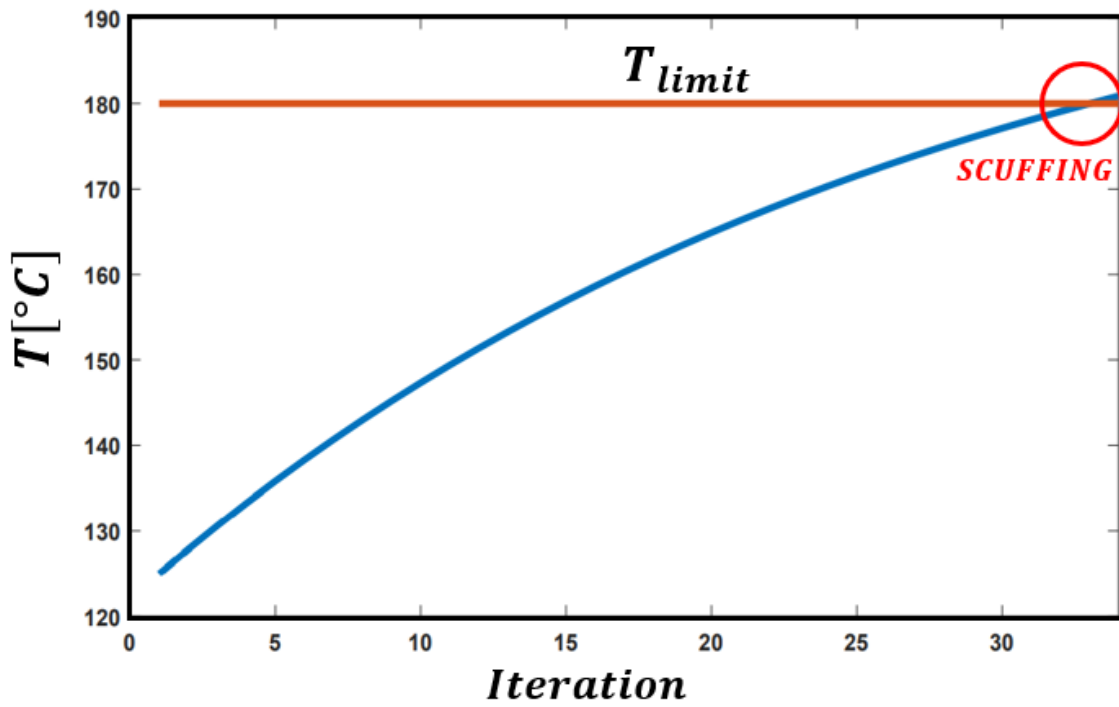


Figure 4.9: Temperature evolution over the thermo-mechanical loop

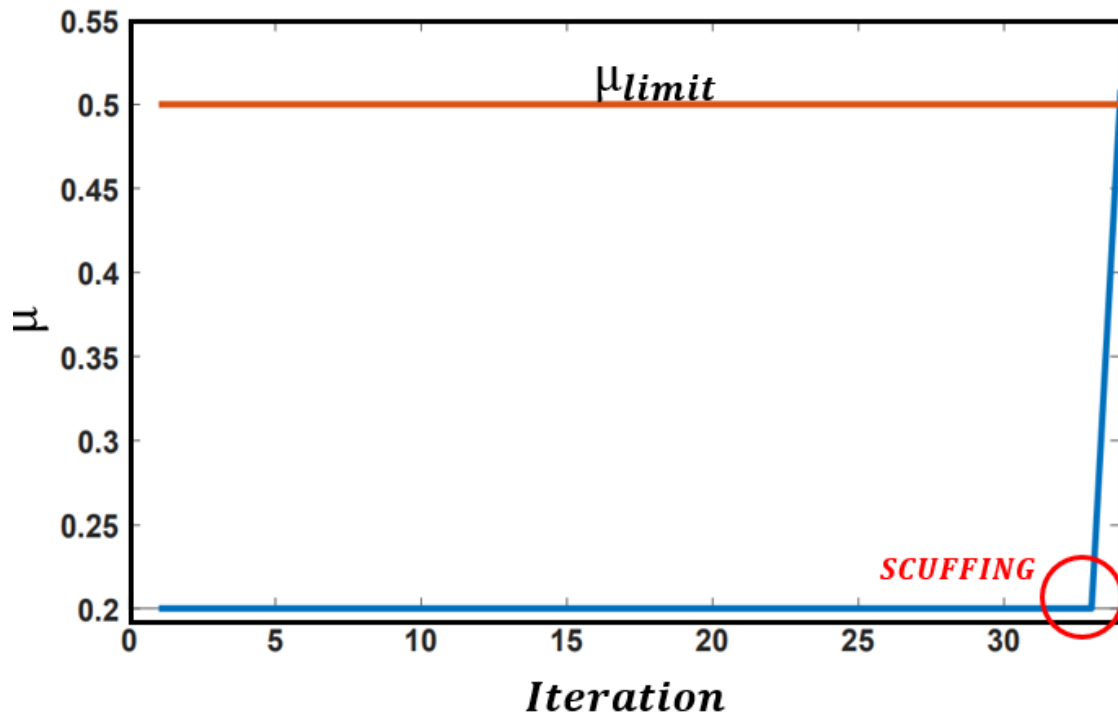


Figure 4.10: Coefficient of friction evolution over the thermo-mechanical loop

4.3.3 Scuffing initiation limit

The influence of the thermo-mechanical effect on the scuffing initiation limit is studied and is presented as a curve. The safe zone, where the thermo-mechanical effect has no negative influence on the contact performance and scuffing is prevented, is below the curve. Whilst, the risk zone, where the thermo-mechanical effect acts like a snowball effect and scuffing can occur, is above the curve.

4.3.3.1 Influence of the heated zone width

The scuffing initiation limit (scuffing curve) is presented in figure 4.11. The scuffing curve is given as a function of the ring tension and the temperature increase due to an increase in the coefficient of friction caused by local starvation. The following statements can be deduced from the figure:

- for the same heated zone width (s) and ring tension, scuffing initiates more rapidly when the temperature increase is more important. In fact, the higher the temperature, the higher the additional load ($F_{additional}$) and the heat flux (q) generated,
- when the ring tension increases for the same heated zone width, the temperature increase required for scuffing initiation decreases,
- for the same ring tension and temperature increase, when the width of the heated zone increases (s), the temperature gradient decreases. Hence, the safe zone is wider and scuffing initiation is delayed.

4.3.3.2 Influence of oil supply regime

The influence of the oil supply regime on the scuffing initiation limit is presented in figure 4.12. The different lubricant supply regimes are detailed in paragraph 2.2.4. Note that if h_{ff} is the oil film thickness in the fully flooded regime, the oil film thickness in the moderately starved regime is $h_{ff}/3$ and in the severe starved regime is $h_{ff}/6$. Results show that the safe zone is wider for the moderately starved regime than that of the severe starved regime. When the film thickness decreases, the coefficient of friction increases, hence the additional heat generated and the temperature gradient. As a result, the surface deformation and the additional load increase, thus scuffing might initiate more rapidly.

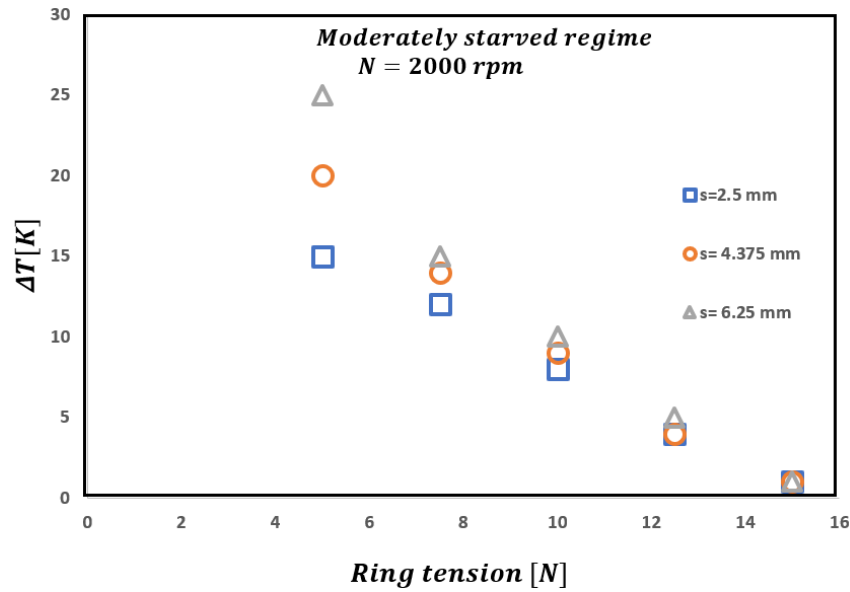


Figure 4.11: Scuffing initiation limit as a function of the ring tension and the temperature increase for different heated zone widths

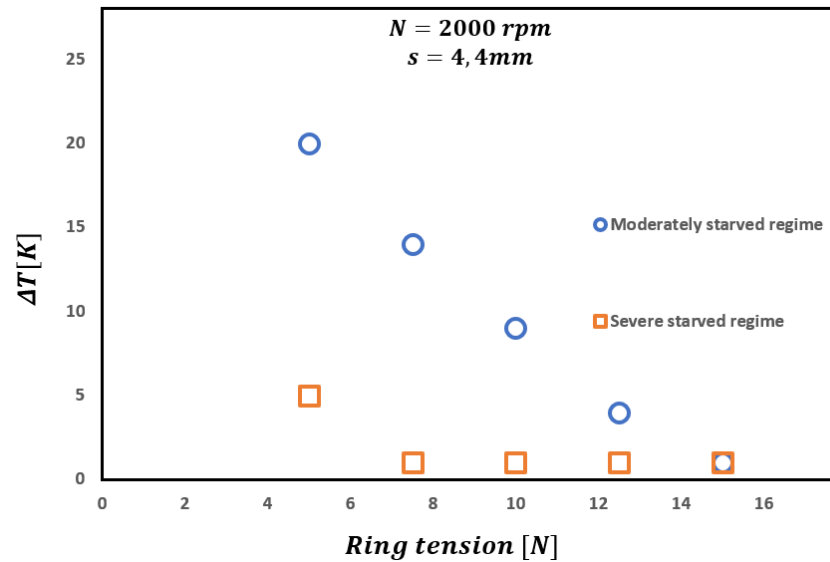


Figure 4.12: Scuffing initiation limit as a function of the ring tension and the temperature increase for different oil supply regimes

4.4 Coupled effects

In this section, the effects influencing scuffing initiation are combined in order to study the contribution of the coupled effects to scuffing initiation.

4.4.1 Complete model

The effects influencing scuffing initiation are:

- the Marangoni effect, which creates local starvation as the lubricant is displaced from the warmer zone to the colder zone as a result of the surface tension gradient generated due to the surface temperature gradient, which might cause scuffing initiation,
- the thermo-mechanical effect, which causes surface deformation that generates an additional load and can increase the surface temperature and might cause scuffing,
- the oil redistribution effect (caused by the ring passage along the liner), which can help to avoid starvation and thus scuffing initiation is prevented.

The algorithm of the model coupling the effects listed above is shown in figure 2.14 and detailed in paragraph 2.4. When assuming that local starvation takes place in the contact due to a non-uniform lubricant distribution, additional heat flux is generated and leads to the thermo-mechanical effect that causes surface deformation and generates an additional load. As a result, heat flux is generated again, leading to a temperature gradient, and a loop is taking place. The loop ends when the surface temperature is re-stabilized to T_0 or when it reaches the limit temperature (T_{limit}) causing desorption of the lubricant additives. Then a Marangoni calculation is carried out in order to calculate the film thickness variation (h_{var}) compared to the mean film thickness (h_{mean}) and the Marangoni and redistributed surfaces ($S_{Marangoni}$, $S_{Redistributed}$) are obtained. Scuffing might initiate if either one or both the two following cases happens:

- if the oil displaced caused by the Marangoni effect quantified as $S_{Marangoni}$ is higher than the oil redistributed caused by the ring displacement quantified as $S_{Redistributed}$ ($S_{Marangoni} > S_{Redistributed}$),
- if the thermo-mechanical effect leads to a continuous increase in the temperature and the coefficient of friction, thus they reach their limit and lubricant additive desorption starts ($T > T_{limit} / \mu > \mu_{limit}$).

4.4.2 Coupled effects: scuffing initiation limit

Table 4.1 displays different cases studied when the three effects are coupled to predict if the contact operates in the safe zone (no risk of scuffing) or it operates in the risk zone (risk of scuffing exists). The input parameters are the width of the heated zone (s), the

wavelength of the oil geometry distribution (λ) which is considered equal to s , the surface nominal temperature (T_0), the temperature increase (ΔT) compared to T_0 (caused by the local starvation) occurring in the contact and the lubricant supply regime which defines the oil film thickness (h_0). The output parameters are the oil film thickness and the mean film thickness of the oil geometry distribution ($h_{mean} = h_0$), the surface temperature (T) and the surfaces moved caused by the Marangoni and the ring displacement effects ($S_{Marangoni}$ and $S_{redistributed}$). If $S_{Redistributed}$ is higher than $S_{Marangoni}$ and the temperature T is lower than the limit temperature, scuffing is prevented and the contact operates in the safe zone. In this case, the green color designates the safe zone in the table. Whilst, when $S_{Redistributed}$ is lower than $S_{Marangoni}$ or the temperature T is higher than the limit temperature, scuffing might occur and it is caused by the Marangoni or the thermo-mechanical effects. Here, the contact operates in the risk zone, which is indicated by the red color in the table.

The correct way to read the table is to compare the cells with the same color of the input parameter, which is the only parameter varied between the two different cases, in order to study its impact on scuffing. For example, the table cell of the temperature increase (ΔT) in case 1 and case 2 is the same (dark blue color), which means that to study the influence of the temperature increase, case 2 is compared to case 1.

Parameter	Unit	Case1	Case2	Case3	Case4	Case5
$s = \lambda$	mm	4.4	4.4	4.4	6.25	6.25
T_0	°C	90	90	90	90	90
ΔT	°C	15	20	15	20	20
Lubricant supply regime	—	mean oil supply regime	mean oil supply regime	severe oil supply regime	mean oil supply regime	severe oil supply regime
$h_0 = h_{mean}$	m	$8e^{-7}$	$4.3e^{-8}$	$3.4e^{-7}$	$7e^{-7}$	$4e^{-8}$
T	°C	90	182	182	90	182
$S_{redistributed}$	mm ²	$2e^{-7}$	$1.6e^{-6}$	$9.5e^{-7}$	$1.4e^{-7}$	$7e^{-7}$
$S_{Marangoni}$	mm ²	$5e^{-9}$	$1.2e^{-5}$	$8e^{-6}$	$3.4e^{-9}$	$4e^{-6}$
Operating condition	—	no risk of scuffing	risk of scuffing	risk of scuffing	no risk of scuffing	risk of scuffing

Table 4.1: Contribution of the coupled effects to scuffing initiation

By comparing case 2 to case 1, the initial temperature increase is varied between the two cases. In case 1, the increase of 15°C did not lead to scuffing initiation, and the contact operates in the safe zone. Whilst, in case 2, the temperature increase is sufficient to cause scuffing initiation and the contact no longer operates in the safe zone. In this case, both effects cause scuffing. The oil displaced caused by the Marangoni effect is more important than that caused by the ring displacement and the temperature increase due to the thermo-mechanical effect exceeds the limit temperature.

Case 3 is also compared to case 1, the oil supply regime carries the difference out. When the lubricant film thickness decreases, the coefficient of friction increases, as well as the heat generated. A transition from the safe zone (green zone) to the risk zone (red zone) occurs between case 1 and case 3. Both effects might cause scuffing.

To study the effect of the heated zone width, case 4 is compared to case 2. For the same temperature increase, scuffing is delayed when the width of the heated zone increases. In case 4, scuffing is prevented and the contact operates in the safe zone. A transition from the safe zone of operating to the risk zone takes place between case 4 and case 5 when the lubricant supply regime becomes more severe.

4.5 Conclusion

The influence of the thermo-mechanical loop on scuffing initiation is presented in this chapter. The surface deformation due to a surface temperature difference generates an additional load that increases the contact pressure. The latter, combined with the coefficient of friction generates a local heat flux that leads again to a temperature variation. Results show that this thermo-mechanical loop can lead to scuffing if the temperature increases continuously and exceeds the limit temperature for the lubricant additive desorption. The scuffing initiation limit is presented in curves as a function of the ring tension and the temperature increase for different heated zone widths and lubricant supply regimes. The safe zone, where scuffing is prevented, is wider when the width of the heated zone increases or when the oil supply regime is less severe. Moreover, the contribution of the coupled effects (the Marangoni, the thermo-mechanical and the oil redistribution effects) to scuffing initiation is presented. Results show that when the thermo-mechanical loop acts like a snowball effect and the surface temperature exceeds the limit temperature, the surface moved due to the Marangoni effect is higher than the one moved because of the ring displacement and scuffing might initiate. The scuffing initiation limit depends on several parameters, such as the width of the heated zone, the lubricant supply regime, the temperature increase, the limit temperature of the lubricant additive desorption and the ring tension.

Chapter 5

Conclusion and future work

Contents

5.1 Conclusion	86
5.2 Future work	86

5.1 Conclusion

The piston-ring cylinder-liner (PRCL) contact contributes to an important amount of energy losses occurring in internal combustion engines (ICE). A thorough understanding of the phenomena acting in this contact is vital to enhance the overall performance of the ICE and meet the environmental standards.

Moreover, scuffing is a catastrophic surface damage that can initiate in the PRCL contact and lead to a complete engine failure. In this study, scuffing initiation risk is studied numerically as a function of the operating parameters through a thermal approach.

The thermal effects impacting scuffing initiation are the thermo-mechanical and the Marangoni effects. The first one leads to a surface deformation that causes the increase in the contact load. The second one causes an oil displacement from the warmer contact zones to the colder ones, which might provoke local oil starvation that accentuates the scuffing initiation risk.

Another effect, which delays the scuffing initiation is the oil redistribution effect. It is caused by the ring passage along the liner. The ring redistributes the lubricant in the contact and helps to avoid local starvation and thus prevents scuffing initiation.

The scuffing initiation limit is studied as a function of the effects mentioned above and it is presented in curves as a function of the problem parameters.

The scuffing initiation limit depends on the oil supply regime. When the oil quantity increases, the coefficient of friction decreases and the scuffing initiation is delayed. However, when the contact load increases, scuffing initiates more rapidly. Moreover, the width of the heated zone influences scuffing appearance. The safe zone becomes wider when the heated zone width increases. Another parameter affecting scuffing initiation is the limit temperature of the lubricant additive desorption. When the contact temperature reaches the temperature from which lubricant additive desorption initiates, the coefficient of friction increases suddenly and scuffing might initiate.

5.2 Future work

The study carried out in this thesis offers a model for scuffing initiation prediction in the PRCL contact of internal combustion engines. The model could be extended to include:

- an experimental validation of the numerical model,
- a further study of the heat exchange occurring between the liner, the ring and their surroundings,
- the liner surface texturing that appears to impact the PRCL contact performance,
- the impact of the lubricant additive and the material coating, since they have a major role to prevent scuffing initiation
- a less approximation prediction of the additional load caused by the thermo-mechanical effect.

Bibliography

- [1] R. N. Brady, “Internal combustion (gasoline and diesel) engines,” 2013.
- [2] J. Liu and H. Peng, “Modeling and control of a power-split hybrid vehicle,” IEEE transactions on control systems technology, vol. 16, no. 6, pp. 1242–1251, 2008.
- [3] “Engine cooling and lubrication engine cooling during combustion.” <https://slidetodoc.com/engine-cooling-and-lubrication-engine-cooling-during-combustion/>.
- [4] B. Tower, “First report on friction experiments,” Proceedings of the institution of mechanical engineers, vol. 34, no. 1, pp. 632–659, 1883.
- [5] C. Machado, M. Guessasma, V. Bourny, R. Bouzerar, J. Fortin, S. Baudon, and E. Bellenger, “Modélisation numérique discrete innovante pour le monitoring électrique des roulements,” in Congrès français de mécanique, AFM, Association Française de Mécanique, 2017.
- [6] S. Wang, R. Nates, T. Pasang, and M. Ramezani, “Modelling of gas tungsten arc welding pool under marangoni convection,” Universal journal of mechanical engineering, vol. 3, no. 5, pp. 185–201, 2015.
- [7] T. Marcombe, A. Lubrecht, and J. Cavoret, “Liner surface scuffing analysis.” Rapport de Projet Innovation Recherche et Developpement 2018.
- [8] “critical point chemistry.” <https://www.thoughtco.com/definition-of-critical-point-605853>.
- [9] S. C. Tung and M. L. McMillan, “Automotive tribology overview of current advances and challenges for the future,” Tribology International, vol. 37, no. 7, pp. 517–536, 2004.
- [10] Y. Jiang, J. Zhang, G. Hong, L. Wan, and X. Liu, “3d ehd lubrication and wear for piston ring-cylinder liner on diesel engines,” International Journal of Automotive Technology, vol. 16, no. 1, pp. 1–15, 2015.
- [11] M. Mian, “Design and analysis of engine lubrication systems,” tech. rep., SAE Technical Paper, 1997.

- [12] J. M. Perez, "Oxidative properties of lubricants using thermal analysis," Thermochemica acta, vol. 357, pp. 47–56, 2000.
- [13] D. Puhan, "Lubricant and lubricant additives," in Tribology, IntechOpen, 2020.
- [14] H. Y. Chu, W. C. Hsu, and J. F. Lin, "The anti-scuffing performance of diamond nano-particles as an oil additive," Wear, vol. 268, no. 7-8, pp. 960–967, 2010.
- [15] P. Rudenko and A. Bandyopadhyay, "Talc as friction reducing additive to lubricating oil," Applied surface science, vol. 276, pp. 383–389, 2013.
- [16] A. A. S. Omar, F. M. Salehi, U. Farooq, A. Morina, and A. Neville, "Chemical and physical assessment of engine oils degradation and additive depletion by soot," Tribology International, vol. 160, p. 107054, 2021.
- [17] "Machine lubrication." <https://www.machinerylubrication.com/Read/31107/oillubricantadditives>.
- [18] "Oil degradation causes." <https://www.machinerylubrication.com/Read/29169/oildegredationcause>.
- [19] G. Calderbank, E. H. Smith, and I. Sherrington, "Experimental measurement of the time-based development of oil film thickness, lubricating film extent and lubricant transport in crosshead engines," Lubricants, vol. 9, no. 1, p. 4, 2021.
- [20] J. Sun, J. Zhu, H. Wang, X. Zhao, Q. Teng, Y. Ren, G. Zhu, X. Zhang, and Y. Gao, "Research on the influence of the lubrication status at the inlet on the lubrication characteristics of engine piston ring," Lubrication Science, vol. 32, no. 7, pp. 321–332, 2020.
- [21] N. Bolander, B. Steenwyk, F. Sadeghi, and G. Gerber, "Lubrication regime transitions at the piston ring-cylinder liner interface," Proceedings of the Institution of Mechanical Engineers, Part J: Journal of Engineering Tribology, vol. 219, no. 1, pp. 19–31, 2005.
- [22] O. Reynolds, "Iv. on the theory of lubrication and its application to mr. beauchamp tower experiments, including an experimental determination of the viscosity of olive oil," Philosophical transactions of the Royal Society of London, no. 177, pp. 157–234, 1886.
- [23] D. Dowson and G. R. Higginson, Elasto-hydrodynamic lubrication: international series on materials science and technology. Elsevier, 2014.
- [24] P. M. Lugt and G. E. Morales-Espejel, "A review of elasto-hydrodynamic lubrication theory," Tribology Transactions, vol. 54, no. 3, pp. 470–496, 2011.
- [25] R. Stribeck, "Die wesentlichen eigenschaften der gleit-und rollenlager," Zeitschrift des Vereines Deutscher Ingenieure, vol. 46, pp. 1341–1348, 1902.

-
- [26] R. Stribeck and M. Schröter, Die wesentlichen Eigenschaften der Gleit- und Rollenlager: Untersuchung einer Tandem-Verbundmaschine von 1000 PS. Springer, 1903.
- [27] L. Gümbel, “Das problem der lagerreibung,” Mbl. Berlin. Bez. Ver. dtsh. Ing., vol. 5, pp. 87–104, 1914.
- [28] M. D. Hersey, “The laws of lubrication of horizontal journal bearings,” Journal of the Washington Academy of Sciences, vol. 4, no. 19, pp. 542–552, 1914.
- [29] D. Dowson, “The history of tribology in america,” 1981.
- [30] S. McKee, “The effect of running-in on journal bearing performance,” Mech. Eng., vol. 49, pp. 1335–1340, 1927.
- [31] G. Vogelpohl, “Die stribeck-kurve als kennzeichen des allgemeinen reibungsverhaltens geschmierter gleitflächen,” Z. VDI, vol. 96, no. 9, pp. 261–68, 1954.
- [32] Y. Hori, Hydrodynamic lubrication. Springer Science & Business Media, 2006.
- [33] Y. Choi, C. Lee, Y. Hwang, M. Park, J. Lee, C. Choi, and M. Jung, “Tribological behavior of copper nanoparticles as additives in oil,” Current Applied Physics, vol. 9, no. 2, pp. e124–e127, 2009.
- [34] R. Rahmani, H. Rahnejat, B. Fitzsimons, and D. Dowson, “The effect of cylinder liner operating temperature on frictional loss and engine emissions in piston ring conjunction,” Applied energy, vol. 191, pp. 568–581, 2017.
- [35] E. Price, A. Lees, and M. Friswell, “Detection of severe sliding and pitting fatigue wear regimes through the use of broadband acoustic emission,” Proceedings of the Institution of Mechanical Engineers, Part J: Journal of Engineering Tribology, vol. 219, no. 2, pp. 85–98, 2005.
- [36] K. C. Ludema, “A review of scuffing and running-in of lubricated surfaces, with asperities and oxides in perspective,” Wear, vol. 100, no. 1-3, pp. 315–331, 1984.
- [37] L. Ting and J. Mayer Jr, “Piston ring lubrication and cylinder bore wear analysis, part i nealetheory,” 1974.
- [38] A. Azam, A. Ghanbarzadeh, A. Neville, A. Morina, and M. C. Wilson, “Modelling tribochemistry in the mixed lubrication regime,” Tribology International, vol. 132, pp. 265–274, 2019.
- [39] L. Yang, A. Neville, A. Brown, P. Ransom, and A. Morina, “Friction reduction mechanisms in boundary lubricated w-doped dlc coatings,” Tribology International, vol. 70, pp. 26–33, 2014.
-

- [40] C. Espejo, C. Wang, B. Thiébaud, C. Charrin, A. Neville, and A. Morina, “The role of modtc tribochemistry in engine tribology performance. a raman microscopy investigation,” Tribology International, vol. 150, p. 106366, 2020.
- [41] Y. Chung, H. Schock, and L. Brombolich, “Fire ring wear analysis for a piston engine,” tech. rep., SAE Technical Paper, 1993.
- [42] N. P. Suh and N. Saka, “Fundamentals of tribology,” tech. rep., The MIT Press, Cambridge, Massachusetts, 1980.
- [43] P. Obert, T. Müller, H.-J. Füßer, and D. Bartel, “The influence of oil supply and cylinder liner temperature on friction, wear and scuffing behavior of piston ring cylinder liner contacts—a new model test,” Tribology International, vol. 94, pp. 306–314, 2016.
- [44] Z. Ma, N. A. Henein, and W. Bryzik, “A model for wear and friction in cylinder liners and piston rings,” Tribology transactions, vol. 49, no. 3, pp. 315–327, 2006.
- [45] N. Morris, R. Rahmani, H. Rahnejat, P. King, and B. Fitzsimons, “Tribology of piston compression ring conjunction under transient thermal mixed regime of lubrication,” Tribology International, vol. 59, pp. 248–258, 2013.
- [46] W. Van Dam, M. W. Cooper, K. Oxorn, and S. Richards, “Observations from cylinder liner wear studies in heavy duty diesel engines and the evolution towards lower viscosity heavy duty engine lubricants,” tech. rep., SAE Technical Paper, 2011.
- [47] B.-K. Chui and H. J. Schock, “Computational analysis of piston-ring wear and oil consumption for an internal combustion engine,” in Internal Combustion Engine Division Fall Technical Conference, vol. 46628, pp. 461–469, 2002.
- [48] F. Saeidi, S. Shevchik, and K. Wasmer, “Automatic detection of scuffing using acoustic emission,” Tribology International, vol. 94, pp. 112–117, 2016.
- [49] M. Neale, “Piston ring scuffing a broad survey of problems and practice,” Proceedings of the Institution of Mechanical Engineers, vol. 185, no. 1, pp. 21–32, 1970.
- [50] A. Green, “Friction between unlubricated metals: a theoretical analysis of the junction model,” Proceedings of the Royal Society of London. Series A. Mathematical and Physical Sciences, vol. 228, no. 1173, pp. 191–204, 1955.
- [51] E. C. Cutiongco and Y.-W. Chung, “Prediction of scuffing failure based on competitive kinetics of oxide formation and removal: application to lubricated sliding of aisi 52100 steel on steel,” Tribology transactions, vol. 37, no. 3, pp. 622–628, 1994.

- [52] H. Mishina and T. Sasada, "Observation of metallic structure of seized portion and mechanism of seizure," in Proceedings 24th Japan Congress on Materials Research, 1981.
- [53] J. Enthoven and H. Spikes, "Infrared and visual study of the mechanisms of scuffing," Tribology Transactions, vol. 39, no. 2, pp. 441–447, 1996.
- [54] M. Tas, A. Banerji, M. Lou, M. Lukitsch, and A. Alpas, "Roles of mirror-like surface finish and dlc coated piston rings on increasing scuffing resistance of cast iron cylinder liners," Wear, vol. 376, pp. 1558–1569, 2017.
- [55] A. Dyson, "The failure of elastohydrodynamic lubrication of circumferentially ground discs," Proceedings of the Institution of Mechanical Engineers, vol. 190, no. 1, pp. 699–711, 1976.
- [56] A. de Gee and G. Rowe, "Glossary of terms and definitions in the field of friction, wear and lubrication tribology," Organization for Economic Co-operation and Development, Paris, 1969.
- [57] M. Shuster, D. Combs, K. Karpip, and D. Burke, "Piston ring cylinder liner scuffing phenomenon studies using acoustic emission technique," SAE transactions, pp. 901–913, 2000.
- [58] M. Shen, H. Cheng, and P. Stair, "Scuffing failure in heavily loaded slow speed conformal sliding contacts," 1991.
- [59] B. Li, C. H. Wong, and Q. Chen, "Kinetics of lubricant desorption and decomposition under heat treatment: a molecular dynamics study," Soft Matter, vol. 9, no. 3, pp. 700–708, 2013.
- [60] J. Qu, J. J. Truhan, P. J. Blau, and H. M. Meyer III, "Scuffing transition diagrams for heavy duty diesel fuel injector materials in ultra low-sulfur fuel-lubricated environment," Wear, vol. 259, no. 7-12, pp. 1031–1040, 2005.
- [61] R. Johnson, T. Dow, and Y. Zhang, "Thermoelastic instability in elliptic contact between two sliding surfaces," 1988.
- [62] X. Ye, G. Chen, M. Luo, and Y. Jiang, "Three-dimensional analysis of tribological performance and heat transfer in piston and cylinder liner system," in Internal Combustion Engine Division Fall Technical Conference, vol. 41618, pp. 351–361, 2003.
- [63] Y. Xiaoming, C. Guohua, J. Yankun, and Z. Yunchuan, "Numerical investigation of the ehl performance and friction heat transfer in piston and cylinder liner system," tech. rep., SAE Technical Paper, 2004.

- [64] R. Barunovic, V. Haas, C. Langlade, and C. E. Krill III, "Sliding wear of 100cr6 in a diesel-lubricated flat-flat contact under realistic loads," Tribology international, vol. 53, pp. 1–11, 2012.
- [65] N. A. Henein, D. Taraza, N. Chalhoub, M.-C. Lai, and W. Bryzik, "Exploration of the contribution of the start/stop transients in hev operation and emissions," tech. rep., SAE Technical Paper, 2000.
- [66] L. Liu and T. Tian, "Implementation and improvements of a flow continuity algorithm in modeling ring/liner lubrication," SAE transactions, pp. 1165–1173, 2005.
- [67] S. Sanda, M. Murakami, T. Noda, and T. Konomi, "Analysis of lubrication of a piston ring package: Effect of oil starvation on oil film thickness," JSME International Journal Series B Fluids and Thermal Engineering, vol. 40, no. 3, pp. 478–486, 1997.
- [68] S. Bewsher, M. Mohammadpour, H. Rahnejat, G. Offner, and O. Knaus, "An investigation into the oil transport and starvation of piston ring pack," Proceedings of the Institution of Mechanical Engineers, Part J: Journal of Engineering Tribology, vol. 233, no. 1, pp. 112–124, 2019.
- [69] I. Sherrington, "Measurement techniques for piston-ring tribology," Tribology and Dynamics of Engine and Powertrain, pp. 387–425, 2010.
- [70] S. Furuhashi and S. Sasaki, "New device for the measurement of piston frictional forces in small engines," SAE transactions, pp. 781–792, 1983.
- [71] M. Gore, M. Theaker, S. Howell-Smith, H. Rahnejat, and P. D. King, "Direct measurement of piston friction of internal-combustion engines using the floating-liner principle," Proceedings of the Institution of Mechanical Engineers, Part D: Journal of Automobile Engineering, vol. 228, no. 3, pp. 344–354, 2014.
- [72] M. Ma, I. Sherrington, and E. Smith, "Analysis of lubrication and friction for a complete piston-ring pack with an improved oil availability model: Part 1: circumferentially uniform film," Proceedings of the Institution of Mechanical Engineers, Part J: Journal of Engineering Tribology, vol. 211, no. 1, pp. 1–15, 1997.
- [73] O. Akalin and G. M. Newaz, "Piston ring cylinder bore friction modeling in mixed lubrication regime: part i analytical results," J. Trib., vol. 123, no. 1, pp. 211–218, 2001.
- [74] P. Mishra, S. Balakrishnan, and H. Rahnejat, "Tribology of compression ring-to-cylinder contact at reversal," Proceedings of the Institution of Mechanical Engineers, Part J: Journal of Engineering Tribology, vol. 222, no. 7, pp. 815–826, 2008.

-
- [75] P. Mishra, H. Rahnejat, and P. King, “Tribology of the ring bore conjunction subject to a mixed regime of lubrication,” Proceedings of the Institution of Mechanical Engineers, Part C: Journal of Mechanical Engineering Science, vol. 223, no. 4, pp. 987–998, 2009.
- [76] O. Ajayi, C. Lorenzo-Martin, R. Erck, and G. Fenske, “Analytical predictive modeling of scuffing initiation in metallic materials in sliding contact,” Wear, vol. 301, no. 1-2, pp. 57–61, 2013.
- [77] W. Hirst and A. Hollander, “Surface finish and damage in sliding,” Proceedings of the Royal Society of London. A. Mathematical and Physical Sciences, vol. 337, no. 1610, pp. 379–394, 1974.
- [78] H. Yu and J. Medley, “Influence of lubricant additives on friction in a disc machine,” in Tribology Series, vol. 32, pp. 475–486, Elsevier, 1997.
- [79] S. Wan, D. Li, A. K. Tieu, B. Zhang, et al., “Comparison of the scuffing behaviour and wear resistance of candidate engineered coatings for automotive piston rings,” Tribology International, vol. 106, pp. 10–22, 2017.
- [80] M. Kennedy, S. Hoppe, and J. Esser, “Lower friction losses with new piston ring coating,” MTZ worldwide, vol. 75, no. 4, pp. 24–29, 2014.
- [81] I. Etsion, G. Halperin, and E. Becker, “The effect of various surface treatments on piston pin scuffing resistance,” Wear, vol. 261, no. 7-8, pp. 785–791, 2006.
- [82] G. Timmermans and L. Froyen, “Fretting wear behaviour of hypereutectic p/m al-si in oil environment,” Wear, vol. 230, no. 2, pp. 105–117, 1999.
- [83] A. Riahi, T. Perry, and A. Alpas, “Scuffing resistances of al-si alloys: effects of etching condition, surface roughness and particle morphology,” Materials Science and Engineering: A, vol. 343, no. 1-2, pp. 76–81, 2003.
- [84] Z. Ye, C. Zhang, Y. Wang, H. Cheng, S. Tung, Q. J. Wang, and X. He, “An experimental investigation of piston skirt scuffing: a piston scuffing apparatus, experiments, and scuffing mechanism analyses,” Wear, vol. 257, no. 1-2, pp. 8–31, 2004.
- [85] Y. Wang, C. Yao, G. Barber, B. Zhou, and Q. Zou, “Scuffing resistance of coated piston skirts run against cylinder bores,” Wear, vol. 259, no. 7-12, pp. 1041–1047, 2005.
- [86] Y. Wang, K. Brogan, and S. C. Tung, “Wear and scuffing characteristics of composite polymer and nickel/ceramic composite coated piston skirts against aluminum and cast iron cylinder bores,” Wear, vol. 250, no. 1-12, pp. 706–717, 2001.
- [87] P. M. Doran, Bioprocess engineering principles. Elsevier, 1995.
-

- [88] H. Blok, "The flash temperature concept," Wear, vol. 6, no. 6, pp. 483–494, 1963.
- [89] D. Baugh, "The miracle of fire by friction," David Wescott. Primitive Technology: A Book of Earth Skills, vol. 10, pp. 32–33, 1999.
- [90] B. Çavdar, "Effect of temperature, substrate type, additive and humidity on the boundary lubrication in a linear perfluoropolyalkylether fluid," Wear, vol. 206, no. 1-2, pp. 15–23, 1997.
- [91] J. Thomson, "Xlii. on certain curious motions observable at the surfaces of wine and other alcoholic liquors," The London, Edinburgh, and Dublin Philosophical Magazine and Journal of Science, vol. 10, no. 67, pp. 330–333, 1855.
- [92] C. Marangoni, "On the expansion of a drop of liquid floating on the surface of another liquid," Tipographia dei fratelli Fusi, Pavia, 1865.
- [93] L. Scriven and C. Sternling, "The marangoni effects," Nature, vol. 187, no. 4733, pp. 186–188, 1960.
- [94] P. A. Lyford, H. Pratt, D. C. Shallcross, and F. Grieser, "The marangoni effect and enhanced oil recovery part 1. porous media studies," The Canadian Journal of Chemical Engineering, vol. 76, no. 2, pp. 167–174, 1998.
- [95] M. G. Velarde, "Drops, liquid layers and the marangoni effect," Philosophical Transactions of the Royal Society of London. Series A: Mathematical, Physical and Engineering Sciences, vol. 356, no. 1739, pp. 829–844, 1998.
- [96] X. Fanton and A. Cazabat, "Spreading and instabilities induced by a solutal marangoni effect," Langmuir, vol. 14, no. 9, pp. 2554–2561, 1998.
- [97] R. Monti, R. Savino, and S. Tempesta, "Wetting prevention by thermal marangoni effect. experimental and numerical simulation," European Journal of Mechanics-B/Fluids, vol. 17, no. 1, pp. 51–77, 1998.
- [98] M. Gugliotti, M. S. Baptista, and M. J. Politi, "Surface tension gradients induced by temperature: The thermal marangoni effect," Journal of chemical education, vol. 81, no. 6, p. 824, 2004.
- [99] C. Yuan, Z. Peng, X. Zhou, and X. Yan, "Effects of temperature on sliding wear process under contaminated lubricant test conditions," Wear, vol. 257, no. 7-8, pp. 812–822, 2004.
- [100] V. L. Popov and A. Fischersworing-Bunk, "Thermo-mechanical instabilities in friction contact,"
- [101] X. Liu, Y. Wang, and W. Liu, "Finite element analysis of thermo-mechanical conditions inside the piston of a diesel engine," Applied Thermal Engineering, vol. 119, pp. 312–318, 2017.

-
- [102] A. Usman, T. Ahmad Cheema, and C. Woo Park, “Tribological performance evaluation and sensitivity analysis of piston ring lubricating film with deformed cylinder liner,” Proceedings of the Institution of Mechanical Engineers, Part J: Journal of Engineering Tribology, vol. 229, no. 12, pp. 1455–1468, 2015.
- [103] Q. Zhaoju, L. Yingsong, Y. Zhenzhong, D. Junfa, and W. Lijun, “Diesel engine piston thermo-mechanical coupling simulation and multidisciplinary design optimization,” Case Studies in Thermal Engineering, vol. 15, p. 100527, 2019.
- [104] I. Etsion, “State of the art in laser surface texturing,” J. Trib., vol. 127, no. 1, pp. 248–253, 2005.
- [105] Y. Hu, X. Meng, Y. Xie, and J. Fan, “Mutual influence of plateau roughness and groove texture of honed surface on frictional performance of piston ring–liner system,” Proceedings of the Institution of Mechanical Engineers, Part J: Journal of Engineering Tribology, vol. 231, no. 7, pp. 838–859, 2017.
- [106] M. Organisciak, G. Cavallaro, and A. Lubrecht, “Variable lubricant supply of a starved hydrodynamic linear contact: lubricant lateral flow for smooth and laser textured surfaces,” Proceedings of the Institution of Mechanical Engineers, Part J: Journal of Engineering Tribology, vol. 221, no. 3, pp. 247–258, 2007.
- [107] I. Sherrington, “Oil film thickness measurement: a contribution to the understanding and control of lubrication in the piston-ring packs of ic engines,” Proceedings of the Institution of Mechanical Engineers, Part J: Journal of Engineering Tribology, vol. 225, no. 7, pp. 595–601, 2011.
- [108] G. G.-A. Fatjo, E. H. Smith, and I. Sherrington, “Mapping lubricating film thickness, film extent and ring twist for the compression-ring in a firing internal combustion engine,” Tribology International, vol. 70, pp. 112–118, 2014.
- [109] N. Biboulet and A. Lubrecht, “Efficient solver implementation for reynolds equation with mass-conserving cavitation,” Tribology International, vol. 118, pp. 295–300, 2018.
- [110] “Plane-stress and plane-strain analysis.” <https://sites.engineering.ucsb.edu/hpsci-com/projects/stress/introge.pdf>.
- [111] H. Moes, “Lubrication and beyond,” Utwente lecture notes code, vol. 115531, p. 366, 2000.
- [112] N. Biboulet, F. Colin, and A. Lubrecht, “Friction in starved hydrodynamically lubricated line contacts,” Tribology International, vol. 58, pp. 1–6, 2013.
- [113] A. Neville, A. Morina, T. Haque, and M. Voong, “Compatibility between tribological surfaces and lubricant additives—how friction and wear reduction can be controlled by surface/lube synergies,” Tribology international, vol. 40, no. 10-12, pp. 1680–1695, 2007.
-

- [114] N. Dolatabadi, S. Theodossiades, and S. Rothberg, “On the identification of piston slap events in internal combustion engines using tribodynamic analysis,” Mechanical Systems and Signal Processing, vol. 58, pp. 308–324, 2015.
- [115] Z. Geng and J. Chen, “Investigation into piston-slap-induced vibration for engine condition simulation and monitoring,” Journal of sound and vibration, vol. 282, no. 3-5, pp. 735–751, 2005.
- [116] V. Dagostino, D. Guida, A. Ruggiero, and C. Russo, “Optimized ehl piston dynamics computer code,” in AITC-AIT, International Conference on Tribology, pp. 20–22, 2006.
- [117] “Engine oil additives.” <https://www.firestonecompleteautocare.com/blog/oil-change/what-is-engine-oil-additive>.
- [118] L. Joly-Pottuz, B. Vacher, N. Ohmae, J. Martin, and T. Epicier, “Anti-wear and friction reducing mechanisms of carbon nano-onions as lubricant additives,” Tribology Letters, vol. 30, no. 1, pp. 69–80, 2008.
- [119] A. Abdelkhalik, H. Elsayed, M. Hassan, M. Nour, A. Shehata, and M. Helmy, “Using thermal analysis techniques for identifying the flash point temperatures of some lubricant and base oils,” Egyptian Journal of Petroleum, vol. 27, no. 1, pp. 131–136, 2018.
- [120] E. Brandes, W. Möller, and B. P.-T. Bundesanstalt, Safety characteristic data. Wirtschaftsverl. NW, Verlag f. Neue Wiss., 2008.
- [121] “oil data base.” <https://lubs.products.database.total.com/total/quartz/5w30/FR.pdf>.
- [122] “oil data base.” <https://lubs.products.database.total.com/total/quartz/5w30/FR.pdf>.
- [123] “oil data base.” <https://totalenergies.mg/sites/wompnd2091/files/quartz/ineo.pdf>.
- [124] “oil data base.” <https://totalenergies.nc/sites/wompnd1391/files/quartz/ineo.pdf>.
- [125] “Comsol multiphysics.” <https://doc.comsol.com/5.5/doc/com.comsol.help.comsol/>.
- [126] B. K. Dutta, Heat transfer: principles and applications. PHI Learning Pvt. Ltd., 2000.
- [127] A. Bertram and R. Glüge, Solid mechanics. Springer, 2015.
- [128] P. Ungerer and C. Batut, “Prédiction des propriétés volumétriques des hydrocarbures par une translation de volume améliorée,” Revue de l’institut français du pétrole, vol. 52, no. 6, pp. 609–623, 1997.

Appendices

Appendix A

Thermo-mechanical analysis using COMSOL Multiphysics

COMSOL Multiphysics [125] is a simulation software based on the finite element analysis (FEA). It is a solver for various physical problems, especially coupled ones.

A thermo-mechanical problem couples two physics:

- solid heat transfer,
- solid mechanics.

The solid heat transfer physic predicts the energy transfer that may take place between material bodies as a result of temperature variation. Dutta et al. [126] detailed the heat transfer principles and applications. Solid mechanics is the study of the deformation and motion when an external load or temperature change is applied on a solid. For more details about the solid mechanics theory, see Bertram et al. [127].

The detailed modeling procedure using COMSOL is:

- the geometry of the model is defined,
- the type of the material is chosen to define the thermal and mechanical properties,
- the boundary conditions for both physics are defined (temperature, heat flux, strain...),
- the mesh size is chosen for the finite element analysis

As a result, the temperature, stress and deformation distributions are obtained and graphically represented.

Appendix B

Thermo-mechanical ring model

This appendix details the ring model used for the thermo-mechanical analysis. This analysis studies the deformation generated when the ring surface is exposed to a temperature gradient. It also studies the necessary force to bend the ring into its original position.

The ring geometry parameters are:

- the outer diameter is $\phi_{outer}=0.0754$ m,
- the inner diameter is $\phi_{inner}=0.0708$ m,
- the axial thickness is $t_{axial}=1.5e^{-3}$ m.

B.1 3D model analysis

Figure B.1 is an example of the temperature distribution of a ring. It is exposed to a temperature difference of 20 K over a circumferential width of 5 mm along the face in contact with the liner. The imposed temperature of the surface is $T_0=363$ K (except the section where a temperature difference takes place). Note that the upper and lower faces of the ring are exposed to a heat exchange, however, the exchange is considered to be circumstantially uniform.

The ring deformation (shown as a displacement) occurring as a result of the temperature variation shown in figure B.1 is presented in figure B.2. The deformation (Δy) is maximal where the temperature is the highest (at the hot-spot). Note that the ring displacement is null at the imposed fixed ends ($\Delta y = 0$ on the figure).

The force (F) needed to return the hot-spot to its nominal position, as shown in figure B.3 is obtained.

B.2 2D model analysis

Figure B.4 is an example of the temperature distribution of a 2D ring model. It is exposed to a temperature difference of 20 K over a circumferential width of 5 mm along the face

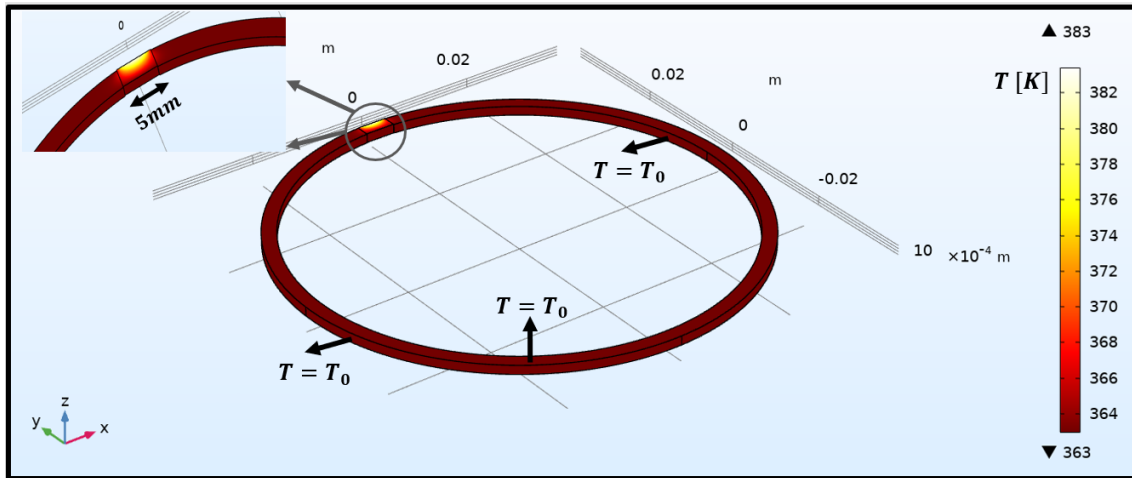


Figure B.1: Temperature distribution of a ring (3D model analysis)

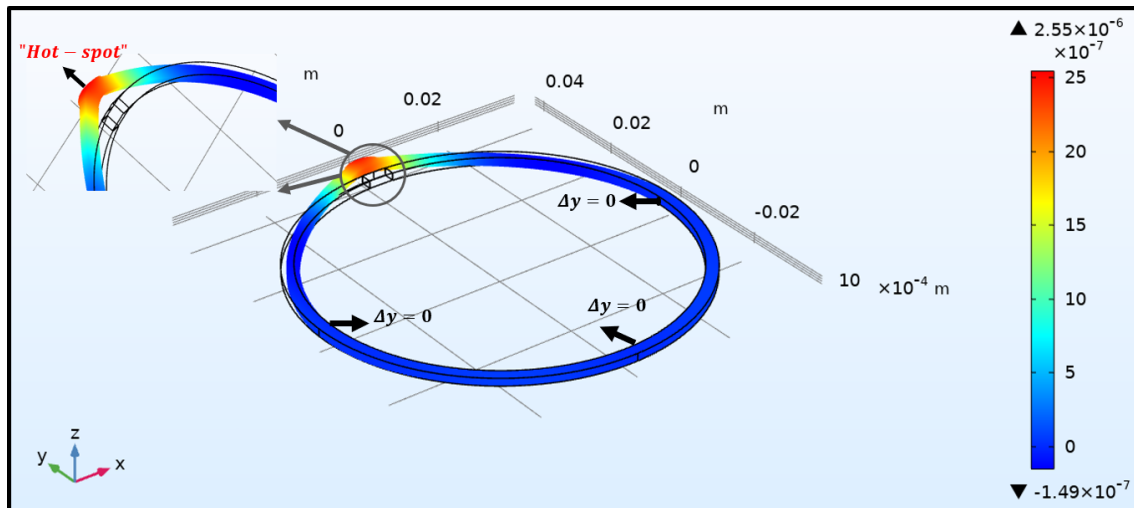


Figure B.2: Ring surface deformation as a result to the temperature variation (see figure B.1) (3D model analysis)

in contact with the liner. The temperature of the inner and outer circumferential faces (except the width where a temperature difference takes place) is imposed and equal to $T_0=363$ K.

The ring deformation (shown as a displacement) occurring as a result of the temperature variation of figure B.4 is presented in figure B.5. The deformation (Δy) is maximal where the temperature is the highest (at the hot-spot). The ends where the displacement is null ($\Delta y = 0$) on the figure, refers to the fixed ends imposed for the displacement calculation. Note that as the axial thickness of the ring is about a few millimeters ($t_{axial} = 1.5$ mm), the analysis is carried out using plane-stress assumptions.

The force (F) needed to return the hot-spot to its nominal position, as shown in figure B.6 is obtained.

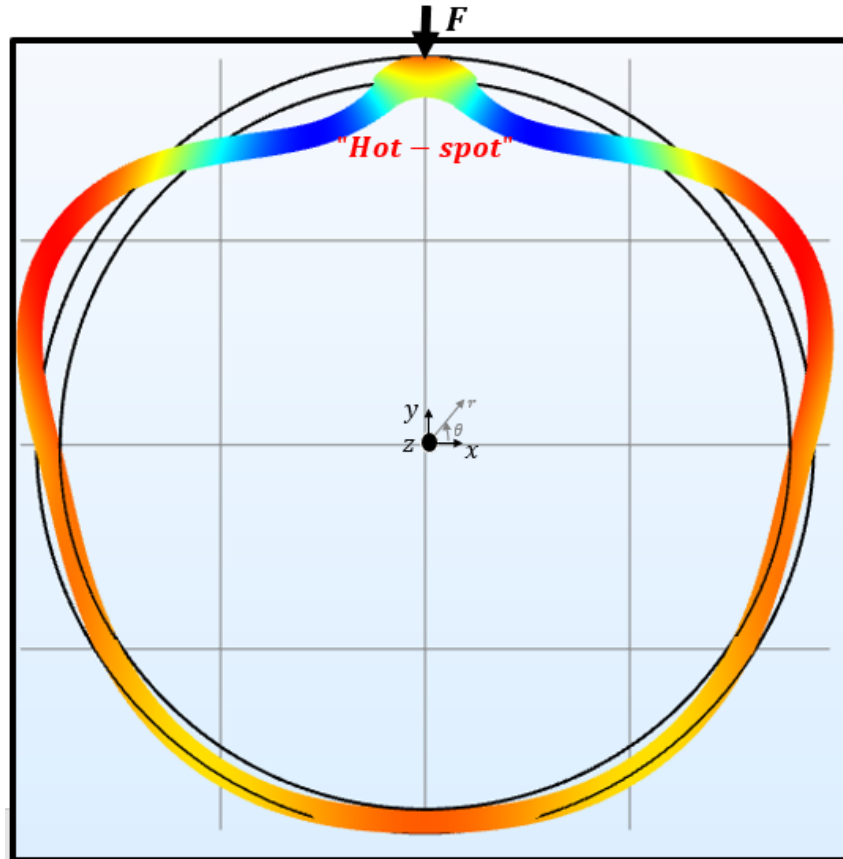


Figure B.3: Ring surface deformation when it is exposed to a load (F) at the hot-spot (3D model analysis)

The temperature increase, the deformation and the force at the hot-spot for both analyses are given in table B.1.

Model	ΔT [K]	Δy [m]	F [N]
3D	20	$2.5e^{-6}$	-1
2D	20	$2.4e^{-6}$	-1.2

Table B.1: Parameters at hot-spot for the 2D and 3D analyses

When comparing the deformation and the load obtained by both analyses, one can conclude that they are similar. Thus, the 2D model analysis for the ring deformation is validated.

The mesh of the ring surface needed for calculation is shown in figure B.7. A mesh refinement study is carried out to validate the accuracy of the solution. From case 1 to case 4, the mesh becomes finer and finer (figures B.7-B.10). The obtained ring deformation (displacement) and required force needed to be applied at the hot-spot for different mesh

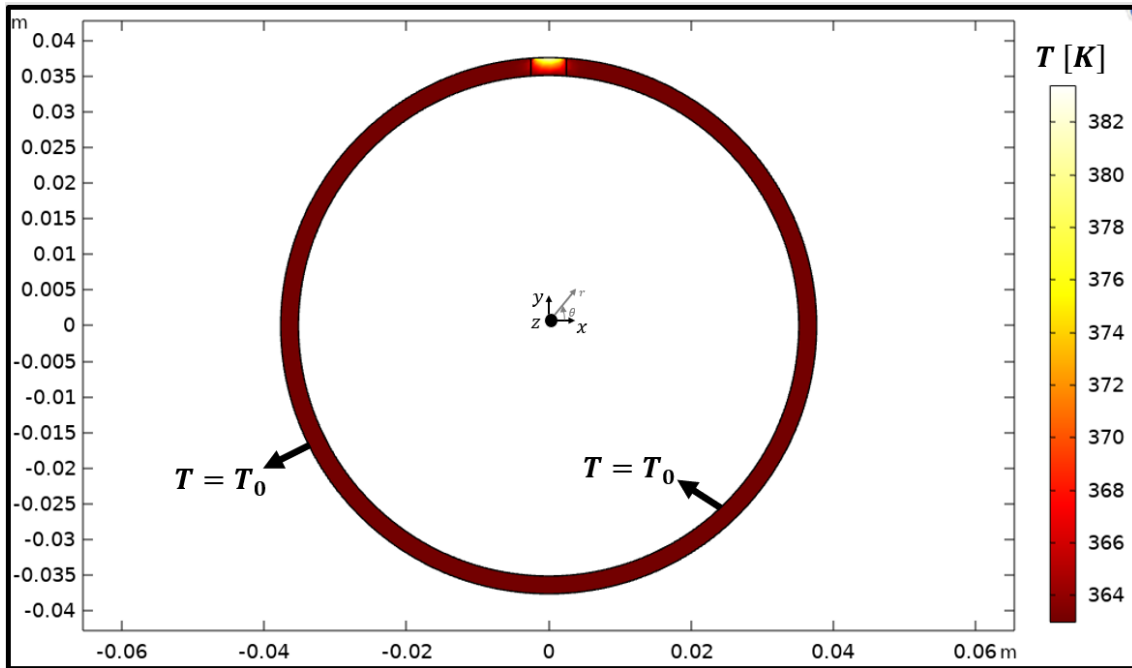


Figure B.4: Temperature distribution of a ring (2D model analysis)

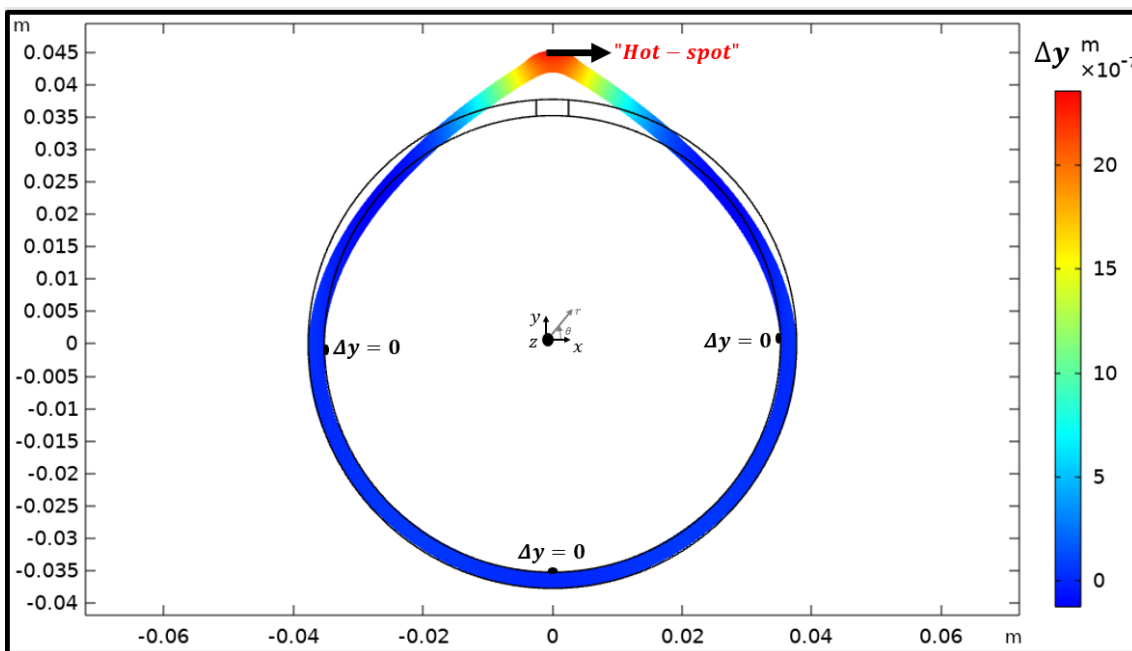


Figure B.5: Ring surface deformation as a result of the temperature variation (see figure B.4) (2D model analysis)

size cases are shown in table B.2. From the table, one can conclude that the parameters obtained at the hot-spot are similar. Hence, the solution obtained using the mesh of case

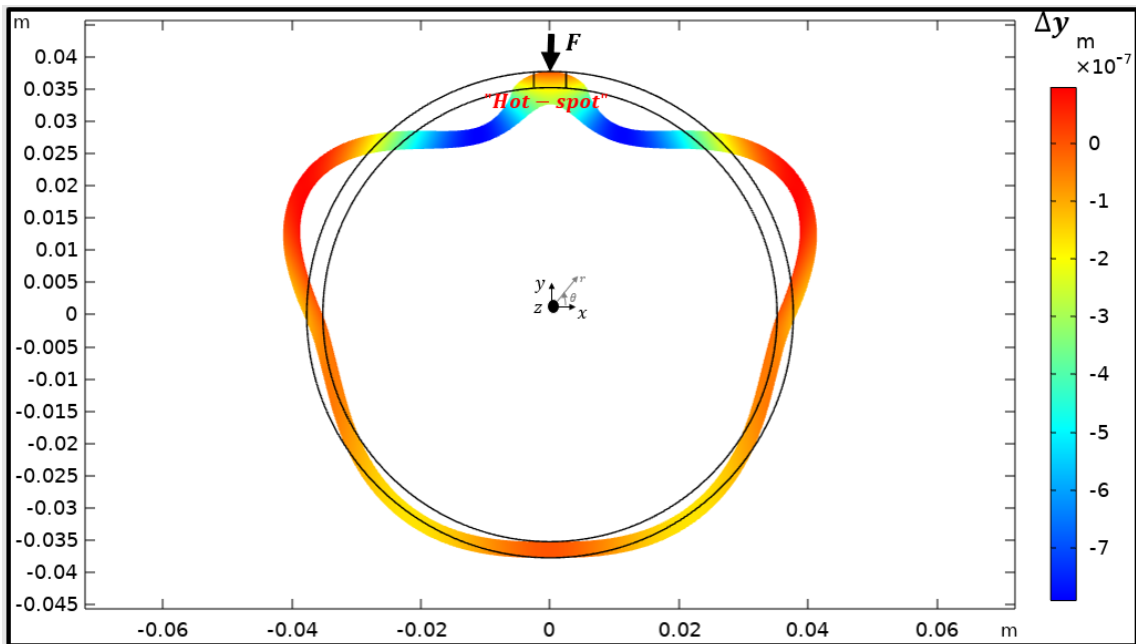


Figure B.6: Ring surface deformation when it exposed to a load (F) at the hot-spot (2D model analysis)

1 is validated.

Case	Δy [m]	F [N]
Case 1	$2.4e^{-6}$	-1.2
Case 2	$2.42e^{-6}$	-1.22
Case 3	$2.44e^{-6}$	-1.23
Case 4	$2.46e^{-6}$	-1.25

Table B.2: Parameters at hot-spot for different mesh size cases

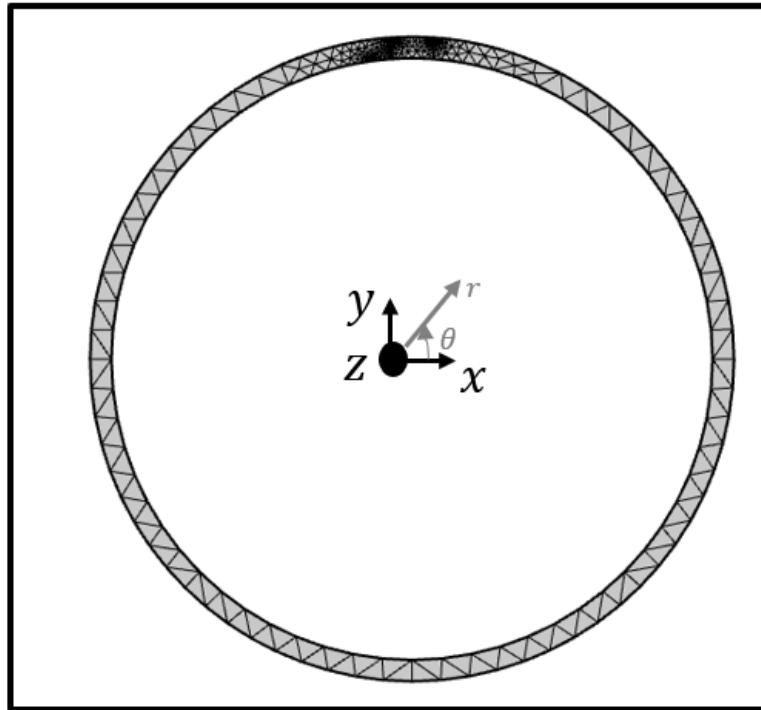


Figure B.7: Case 1: mesh grid of the ring surface

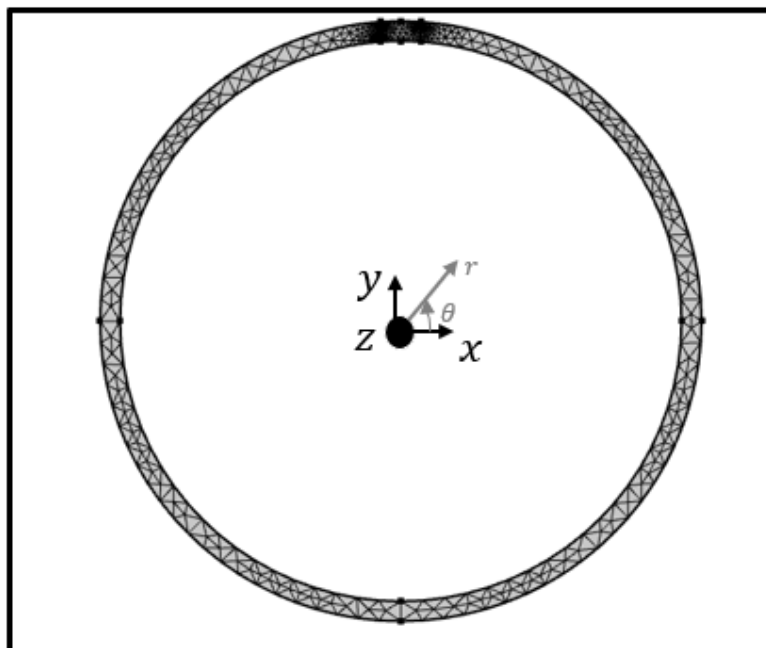


Figure B.8: Case 2: mesh grid of the ring surface

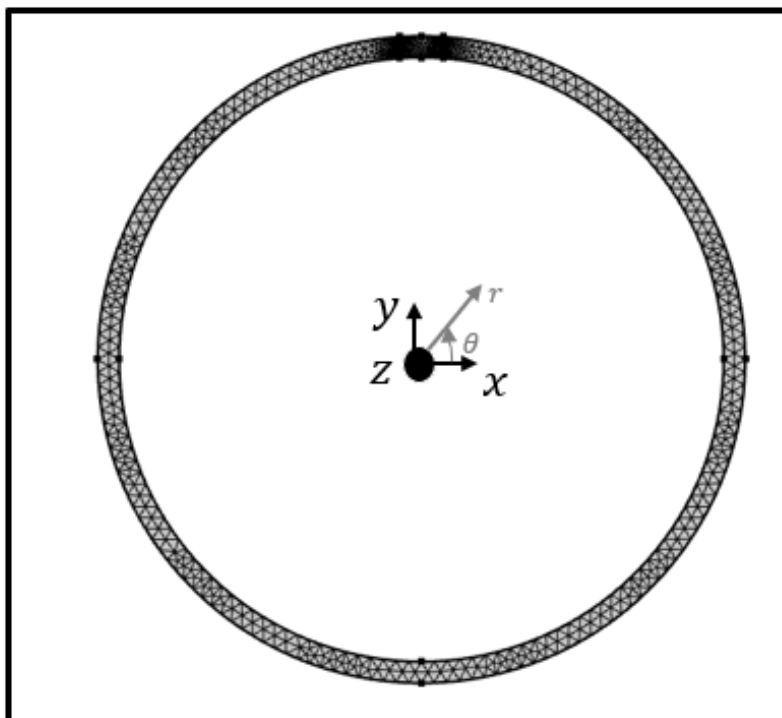


Figure B.9: Case 3: mesh grid of the ring surface

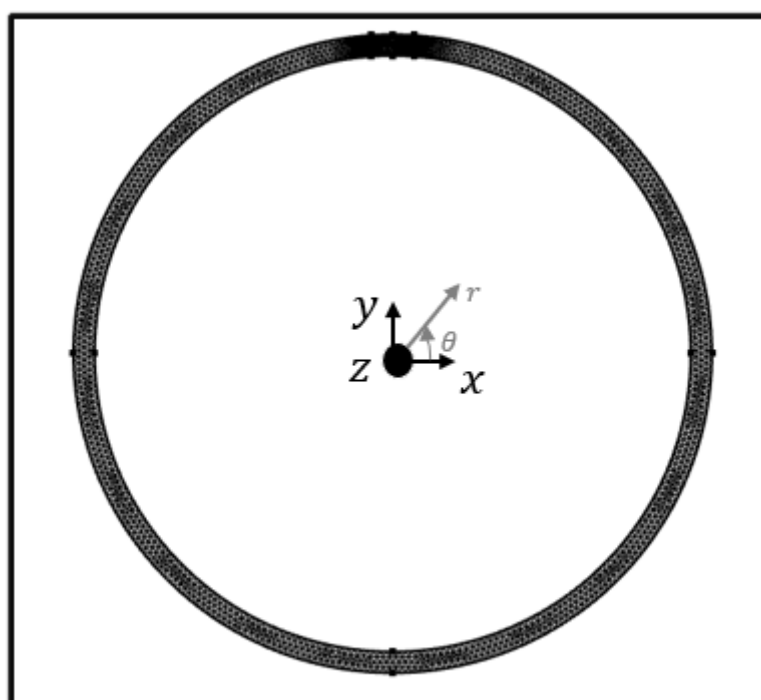


Figure B.10: Case 4: mesh grid of the ring surface

Appendix C

Thermal liner model

A heat flux is generated as a result of friction due to the contact pressure and the ring sliding velocity ($q = \mu p_{contact} u_m$). The ring is moving along the liner in the x -direction as shown in figure C.1. Thus, a transient 3D model is required to calculate the liner temperature distribution.

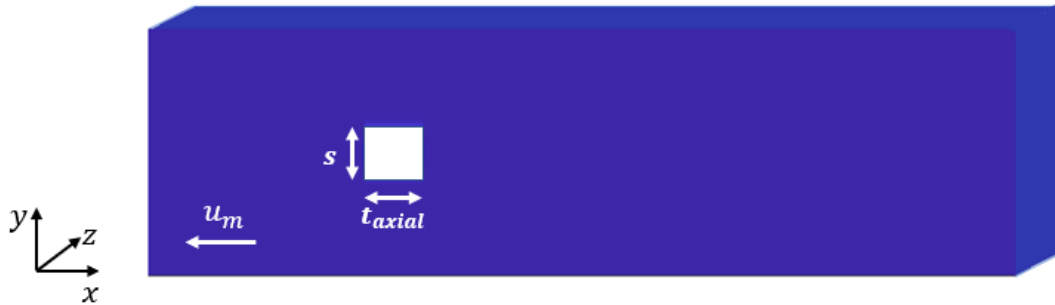


Figure C.1: Liner surface with a moving heat flux

The heat equation considering a moving heat flux is:

$$\frac{\partial^2 \bar{T}}{\partial X^2} + \frac{\partial^2 \bar{T}}{\partial Y^2} + \frac{\partial^2 \bar{T}}{\partial Z^2} = P_e \frac{\partial \bar{T}}{\partial X} \quad (C.1)$$

where P_e is the Peclet number. $P_e = u_m s / D$, (u_m is the velocity, s is the width of the source and D is the diffusivity of the material). An example of the temperature distribution calculation on the liner surface when considering a moving heat flux in the X -direction is shown in figures C.2 and C.3. The Peclet number is $P_e = 100$ and the domain size is $15 * 2.5 * 1 \text{ cm}^3$ respectively in x, y, z directions. The width of the source is $s = 5 \text{ mm}$ and $q = 0.1 * 10^6 * 10 = 10^6 \text{ W/m}^2$.

From figure C.3, it can be concluded that the temperature increases when the source moves and then the temperature decreases and is re-stabilizes.



Figure C.2: (X, Y) plane of the liner surface with a moving heat flux

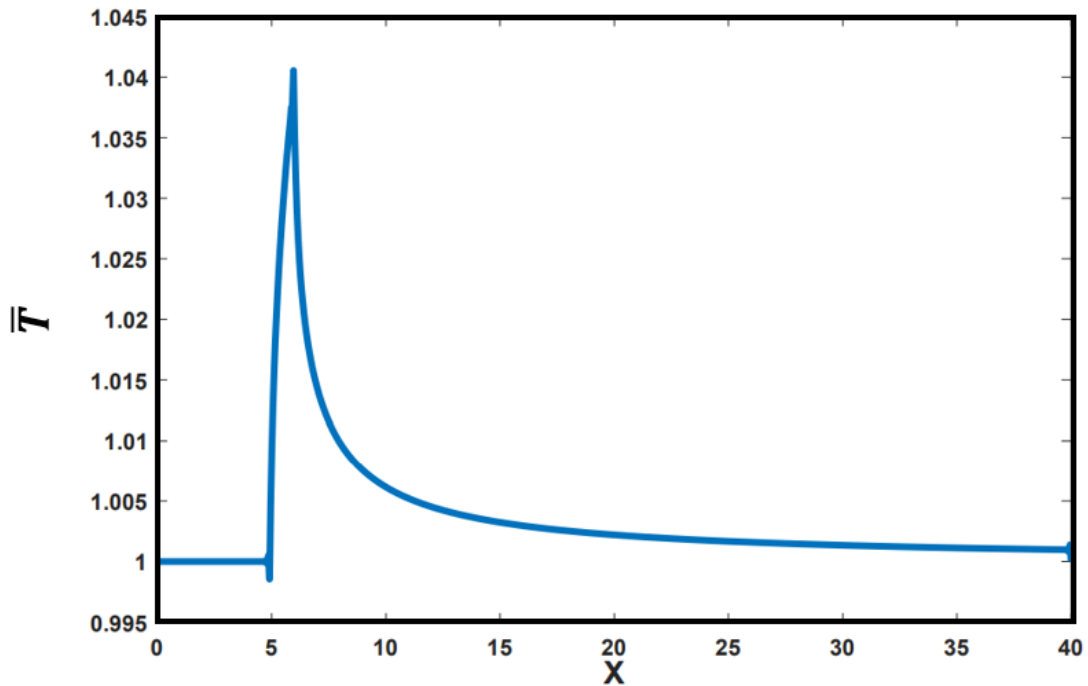


Figure C.3: Dimensionless temperature distribution on the liner surface caused by a moving heat flux

To simplify the model, the heat flux generated is averaged over the time of a ring passage along the liner. The average time of a ring passage is $\Delta t_{passage} = 1/(2f)$, where f is the frequency in Hz . The required time for the heat flux to change position is $\Delta t = t_{axial}/u_m$. The mean heat flux is then obtained as shown below:

$$q_{mean} = \mu p_{contact} u_m \frac{\Delta t}{\Delta t_{passage}} = 2\mu p_{contact} t_{axial} f \quad (C.2)$$

The liner surface exposed to the mean heat flux ($q_{mean} = 2 * 0.1 * 10^6 * 1.5e^{-3} * 60 = 18 * 10^3 W/m^2$) is presented in figure C.4. As the heat flux and the temperature increase are constant along the liner, and the surface is considered infinitely long in the x -direction,

the transient 3D model is simplified to a stationary 2D model.

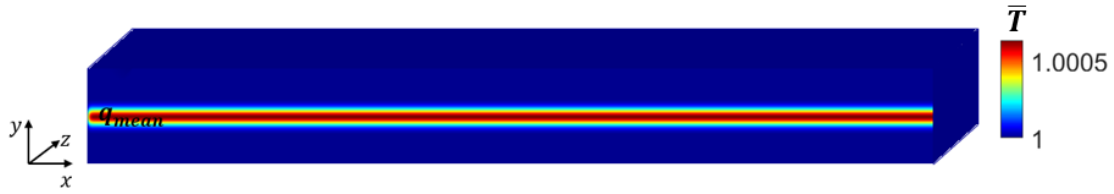


Figure C.4: Liner surface with mean heat flux

The calculational domain presented in the (Y,Z) plane is meshed from 0 to n_i for the Y -direction and from 0 to n_j for the Z -direction. The number of points is $(n_i+1)*(n_j+1)$. The size of the mesh is $dY*dZ$ where $dY = dZ$. Figure C.5 shows the discretized domain where the number of points is $(525*52)$.

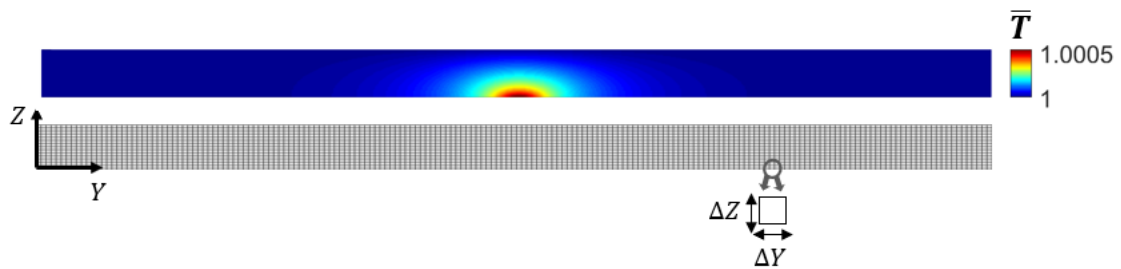


Figure C.5: Mesh grid of the liner surface

Appendix D

Ring tension and pressure distribution

The measurement of the contact pressure (p_c) which pushes the ring against the cylinder wall is difficult. In practice, it is calculated from the tangential force (F_t) which is the needed load to apply to the ends of the ring in order to compress it to the specific closed gap. Figure D.1 shows the pressure distribution, which is constant.

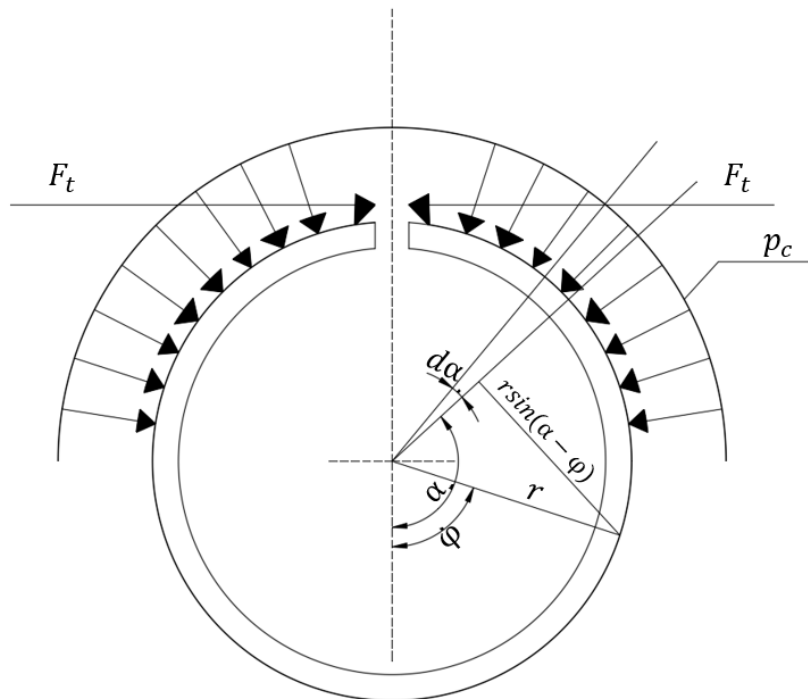


Figure D.1: Constant contact pressure distribution

The elementary bending moment is given in the equation below:

$$dM = p_c t_{axial} r^2 \sin(\alpha - \phi) d\alpha \quad (D.1)$$

where t_{axial} is the axial thickness of the ring. From this equation, the bending moment as a function of the contact pressure is:

$$M = p_c t_{axial} r^2 (1 + \cos(\phi)) \quad (D.2)$$

The bending moment can also be given as a function of the tangential force:

$$M = F_t t_{axial} r (1 + \cos(\phi)) \quad (D.3)$$

From the equations D.2 and D.3 the equation between the ring tension and the contact pressure is obtained:

$$p_c = \frac{F_t}{r t_{axial}} \quad (D.4)$$

Appendix E

Numerical model input variables

This appendix presents the input parameters used for the numerical study. Table E.1 and table E.2 give respectively the chosen geometric and operating parameters.

Variable	Symbol	Unit	Value
Outer ring diameter	ϕ_{outer}	<i>mm</i>	75.4
Inner ring diameter	ϕ_{inner}	<i>mm</i>	72.9
Axial ring thickness	t_{axial}	<i>mm</i>	1.5
Radial ring thickness	t_{radial}	<i>mm</i>	2.5
Ring radius of curvature	R_x	<i>mm</i>	10
Heated zone width	s	<i>mm</i>	[1;6.25]
Calculational domain width	s_d	<i>mm</i>	50
Calculational domain thickness	e_d	<i>mm</i>	2.5
Surface roughness	σ	μm	0.2

Table E.1: Geometric parameters

The lubricant properties (viscosity and density) are given as curves, as a function of the temperature as shown in figure E.1 and figure E.2.

The phase diagram of a fluid is given in figure E.3. As shown in the figure, the critical point is the endpoint of a phase equilibrium curve. It is the point at which the liquid and its vapor can coexist. The critical temperature of hydrocarbons ranges around $T_c = 570K$ [128].

Variable	Symbol	Unit	Value
Stroke length	C	cm	10
Engine speed	N	rpm	[1000;4000]
Initial temperature	T_0	$^{\circ}C$	90
Ring tension	$F_{tension}$	N	[5;25]

Table E.2: Operating parameters

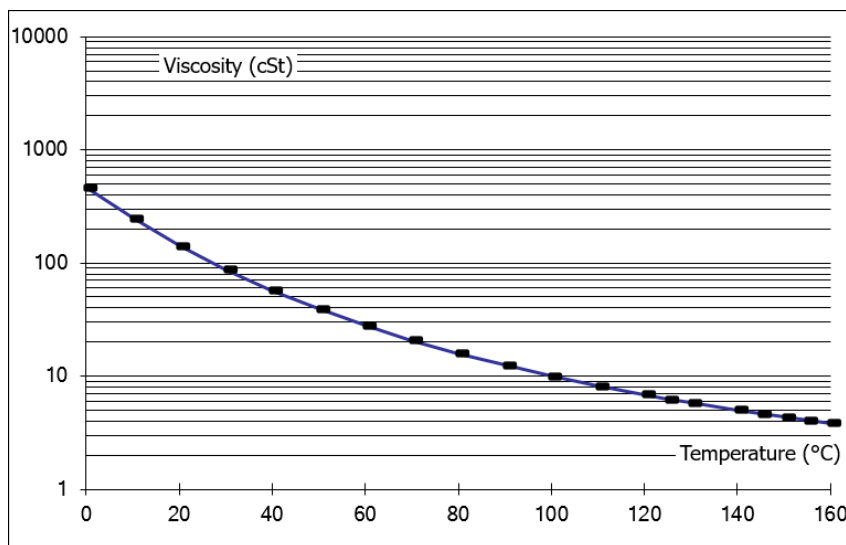


Figure E.1: Lubricant kinematic viscosity as a function of the temperature

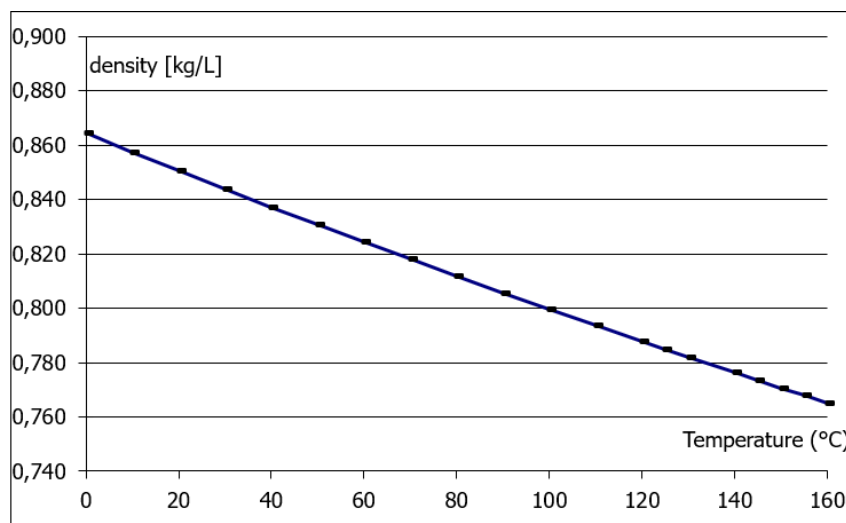


Figure E.2: Lubricant density as a function of the temperature

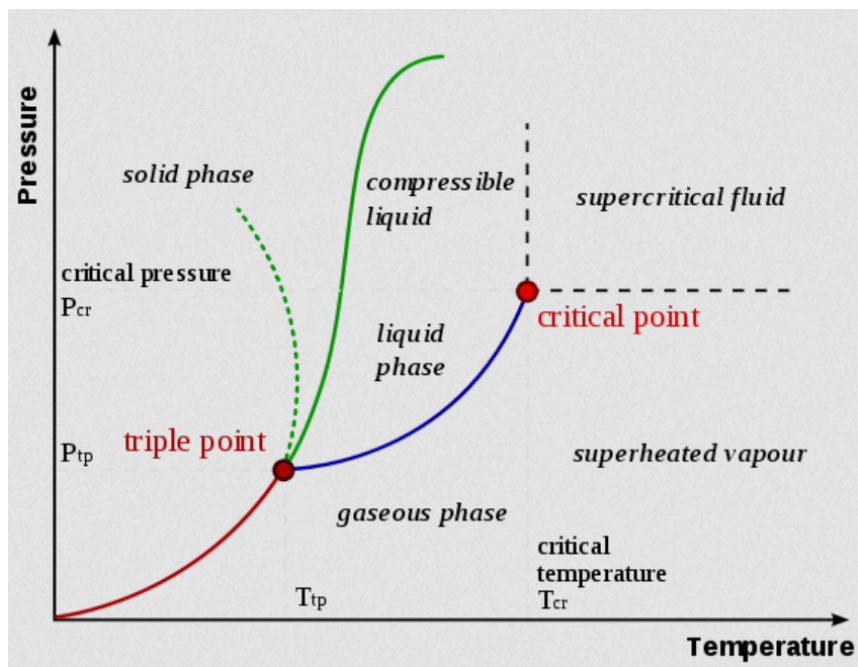


Figure E.3: Phase diagram [8]

Résumé étendu en français

1 Introduction

Un moteur à combustion interne (MCI) est un moteur thermique dans lequel la combustion du carburant est le processus de base de libération d'énergie. Cette énergie libérée est ensuite convertie en travail. Le moteur est composé des cylindres fixes et pistons mobiles. L'expansion des gaz pousse le piston vers le bas, qui à son tour fait tourner le vilebrequin. Ce mouvement entraîne les roues du véhicule à travers un système d'engrenages et un groupe motopropulseur.

Le MCI peut être un moteur à essence (allumage commandé) ou un moteur diesel (allumage par compression). Dans la plupart des cas et pour les deux types, le moteur fonctionne sur le cycle à quatre temps qui comprend: phase d'admission, phase de compression, phase de combustion et phase d'échappement.

Ces dernières années, l'objectif de l'amélioration des performances des véhicules tout en optimisant l'économie de carburant et en respectant les normes d'émissions polluantes poussent les chercheurs et les constructeurs automobiles à rechercher des technologies vertes.

Une solution à court terme est le véhicule électrique hybride. Dans ce dernier, une machine électrique est ajoutée au groupe motopropulseur conventionnel, ce qui est bénéfique pour la conservation d'énergie et les pertes en puissance.

Le mode arrêt-démarrage est appliqué pour cette technologie. Lorsque le véhicule est à l'arrêt, le moteur s'arrête, l'énergie est donc conservée. Lorsque le conducteur appuie de nouveau sur le pédale, le moteur redémarre automatiquement. la répétition de ce processus impacte le système de lubrification du moteur. A l'arrêt, les pièces mécaniques ne reçoivent plus de lubrifiant alors que la température du moteur est élevée. Au redémarrage, cette condition critique peut entraîner l'usure et le grippage.

Le grippage est un mode de défaillance soudaine caractérisé par une grave dégradation des surfaces en contact, pouvant entraîner une casse moteur. De plus, le contact segment/chemise provoque la moitié des pertes moteur. Une étude approfondie de ce contact et de son système de lubrification est donc nécessaire pour améliorer les performances globales du moteur.

Même si l'apparition du grippage dans les MCI est rare, des études expérimentales sont menées sur des prototypes pour prédire et empêcher son initiation. La modélisation et la simulation sont des approches qui facilitent l'études de l'initiation du grippage.

L'objectif de la présente étude est de développer un modèle numérique combinant les paramètres et les phénomènes provoquant le grippage dans le contact segment/chemise afin d'éviter son initiation.

2 Résumé

Le processus de lubrification consiste à injecter un fluide appelé lubrifiant entre les pièces mobiles pour les séparer et éviter un contact solide-solide. Un lubrifiant est composé d'huile de base et d'additifs. Les additifs sont des produits chimiques qui améliorent ou ajoutent des propriétés à l'huile de base. Certains additifs principaux sont: modificateurs de viscosité, antioxydants, anti-usures, modificateurs de frottement, inhibiteurs de corrosion et extrême pression.

Les segments sont des anneaux élastiques qui se trouvent dans les rainures du piston. Le contact segment/chemise comprend couremment trois segments: le segment coupe feu, le segment racleur et le segment de contrôle d'huile. La chemise est la paroi intérieure d'un cylindre de moteur, où le piston et les segments se déplacent. Elle est exposée à des températures et pressions élevées. Les principales fonctions des segments sont: la fonction d'étanchéité et la fonction de lubrification. Les fonctions secondaires sont: le transfert de chaleur et le support du piston.

Le grippage est la défaillance tribologique la moins connue en raison du grand nombre de variables impliquées dans son initiation. Il se produit principalement dans un contact lubrifié en présence d'une vitesse. Il s'accompagne généralement d'une augmentation soudaine du frottement, de la température et des vibrations. Un facteur majeur qui contribue à l'initiation du grippage est la quantité du lubrifiant présente dans le contact.

Le grippage est étudié d'une approche thermique. Les phénomènes thermiques sont: l'effet thermomécanique et l'effet de Marangoni. Dans le contact segment/chemise, la génération de chaleur et l'augmentation de la température sont causées par la présence de frottement. De plus, la température est l'un des facteurs clés influant les propriétés du lubrifiant et par suite les performances du contact. L'augmentation de température, réduit la viscosité de l'huile, de sorte qu'un film de lubrifiant plus petit se forme, provoquant le fonctionnement du contact en régime limite.

La discipline thermomécanique semble d'avoir une influence importante sur les systèmes tribologiques. Dans un contact glissant, le frottement généré et la dilatation thermique locale peuvent entraîner une instabilité. Zones avec température plus élevée, une dilatation thermique plus élevée et donc des contraintes plus élevée.

Dans cette étude, cet effet est introduite par une boucle. Considérant qu'en raison d'une manque d'huile locale de lubrifiant dans le contact, le frottement augmente ainsi que la température. L'augmentation de température conduit à une déformation de la surface, ce qui entraîne une charge supplémentaire au contact. Le film d'huile est ainsi calculé dépendant du régime de lubrifiant choisis. Ensuite, le coefficient de frottement est obtenu par la courbe de Stribeck. Plus la hauteur d'huile est faible, plus le coefficient de frottement est élevé. Un flux de chaleur est ainsi généré causant une nouvelle augmentation de température. La boucle est arrêtée lorsque la température diminue et tend vers la température nominale, ou lorsque la température augmente et atteint la température limite de désorption du système d'additif du lubrifiant. Dans ce cas, le coefficient de frottement augmente soudainement ce qui risque de causer le grippage. C'est l'effet de boule de neige.

D'autre part, la convection du fluide due au gradient de tension superficielle est connue sous le nom d'effet Marangoni. En raison de la convection du fluide, une rupture du film peut se produire. Lorsque le gradient de tension superficielle est causé par un gradient de température, l'effet de convection est appelé convection thermo-capillaire ou convection thermique de Marangoni.

Un effet additionnel qui s'ajoute aux deux précédents est l'effet de redistribution d'huile. En fait, le passage du segment tout au long de la chemise redistribue le lubrifiant sur la surface. Cette redistribution évite la sous-alimentation locale d'huile et ralentit l'initiation du grippage, ce qui est bénéfique pour le contact.

L'écartement d'huile due à l'effet de Marangoni et la redistribution d'huile due à l'effet du passage du segment tout au long de la chemise sont quantifiés en fonction des paramètres du problème. La comparaison de ces deux effets est effectuée pour prédire le comportement du contact. Lorsque l'écartement est plus important que la redistribution, un risque d'apparition du grippage existe. Par contre, lorsque l'écartement est balancé avec la redistribution d'huile, la sous-alimentation d'huile est évitée ainsi que le risque d'apparition du grippage.

3 Conclusion

La limite de l'apparition du grippage est donnée sous forme des courbes en fonction des paramètres du problème et des effets étudiés. Au dessous de cette courbe, le grippage est évité et le contact fonctionne dans les conditions nominales. En dessus de cette courbe, un risque d'initiation du grippage existe et le contact ne fonctionne plus sous conditions nominales.

Figure 1 présente la limite d'initiation du grippage à cause de l'effet thermomécanique en fonction de l'augmentation de température et de la tare du segment pour différentes largeurs de la zone sous-alimentée. Comme la figure montre, pour la même largeur de la zone chauffée (s) et la même tare du segment, le grippage apparaît plus rapidement lorsque l'augmentation de température est plus importante. Lorsque la tare augmente pour la même largeur de la zone chauffée, l'augmentation de température qui cause l'initiation du grippage diminue. Pour la même tare, lorsque s augmente, le gradient de température diminue. Par conséquent, l'initiation du grippage est retardée.

La limite d'apparition du grippage à cause de l'effet de Marangoni est présentée dans la figure 2. La figure montre que pour la même tare et augmentation de température, la limite d'initiation se déplace en augmentant la largeur de la zone chauffée. De plus, pour la même largeur de la zone chauffée et en augmentant la tare du segment, l'augmentation de la température requise provoquant le grippage diminue. Ceci est dû à l'augmentation de la charge de contact.

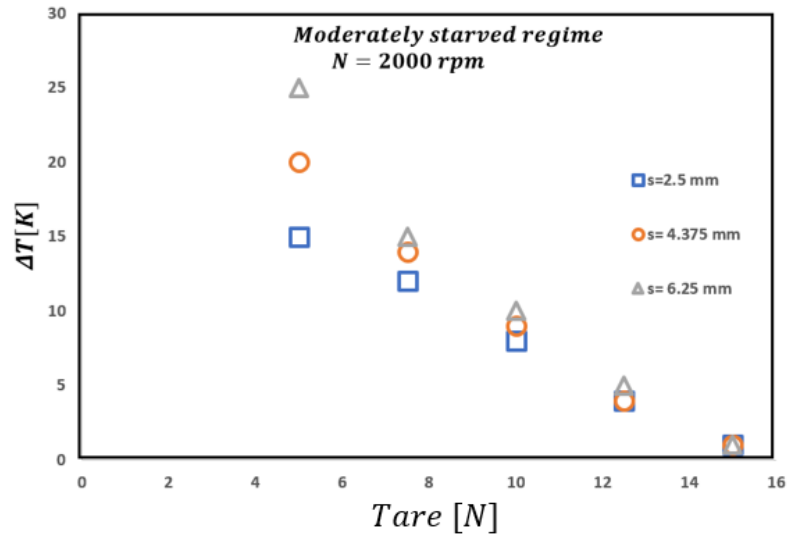


Figure 1: Limite d'initiation du grippage à cause de l'effet thermomécanique

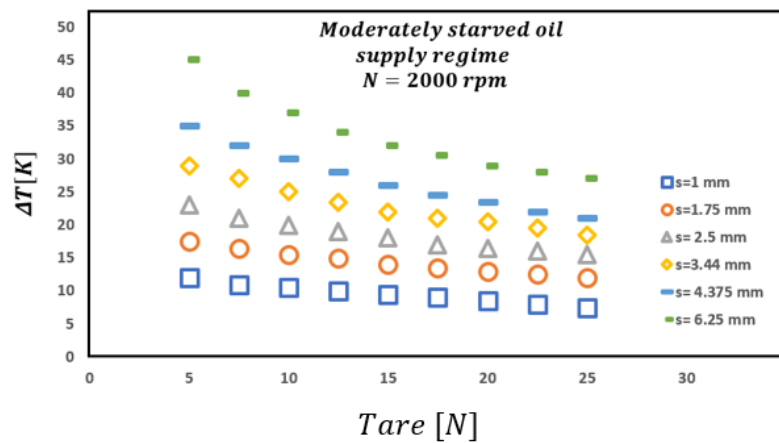


Figure 2: Limite d'initiation du grippage à cause de l'effet Marangoni



FOLIO ADMINISTRATIF

THESE DE L'UNIVERSITE DE LYON OPEREE AU SEIN DE L'INSA LYON

NOM : DAHDAH

DATE de SOUTENANCE : 25 février 2022

Prénoms : Simona

TITRE : Scuffing Initiation Prediction in a Lubricated Piston Ring Cylinder Liner Contact

NATURE : Doctorat

Numéro d'ordre : 2022LYSEI011

Ecole doctorale : Mécanique, Energétique, Génie civil, Acoustique (MEGA)

Spécialité : Génie mécanique

RESUME :

Le contact segment-chemise a une importante influence sur les pertes par frottement du moteur à combustion interne (MCI). D'où la nécessité d'étudier les phénomènes présents dans ce contact ainsi que son processus de lubrification. De plus, le contact segment-chemise peut être exposé au grippage. Le grippage est un mode de défaillance qui peut apparaître dans un contact lubrifié en présence d'une vitesse. Il s'accompagne d'une augmentation de température, de frottement et de vibration. Son apparition dans le MCI est rare mais une fois il apparaît l'endommagement est catastrophique et permanent, d'où l'intérêt de prédire son initiation.

Le grippage est étudié d'une approche thermique pour créer un modèle de prédiction de son initiation dans le contact segment-chemise. Les effets thermiques introduits dans le modèle sont : l'effet thermomécanique et l'effet de Marangoni. Le premier effet cause une déformation de la surface due à l'augmentation de la température prenant lieu dans le contact. Cette déformation engendre une charge additionnelle dans le contact. Le second effet cause la convection et l'écartement d'huile, se qui crée une sous-alimentation locale en lubrifiant dans le contact. Un troisième effet qui s'ajoute aux deux précédents est le déplacement du segment sur la chemise. Ce dernier redistribue l'huile et aide à éviter la sous-alimentation locale en lubrifiant. L'influence des paramètres du problème sur ces effets est étudiée pour obtenir des graphes présentant la limite d'initiation du grippage dans le contact segment-chemise.

MOTS-CLÉS : Contact segment-chemise, Grippage, Lubrification, Simulation numérique

Laboratoire (s) de recherche : Laboratoire de Mécanique des Contacts et des Structures
UMR CNRS 5259-INSA de Lyon
Bâtiment Sophie Germain
Avenue Jean Capelle
69621 Villeurbanne Cedex FRANCE

Directeur de thèse : LUBRECHT Antonius. A

Président de jury : Prof. SHERRINGTON Ian

Composition du jury : MORINA Ardian, SHERRINGTON Ian, QUILLIEN Muriel, LUBRECHT Antonius. A, BIBOULET Nans, CHARLES Pierre

